



Universität Potsdam

Mathematisch-Naturwissenschaftliche Fakultät
Institut für Physik und Astronomie

Single particle spectroscopy using a scattering scanning near field optical microscope

Diplomarbeit

von

Felix Stete

Dezember 2014

Erster Gutachter: Prof. Dr. Matias Bargheer
Zweiter Gutachter: Prof. Dr. Dieter Neher

Betreuer: Prof. Dr. Matias Bargheer
Dr. Wouter Koopman

Zusammenfassung

Die vorliegende Arbeit beschreibt den Aufbau eines streuungsbasierten optischen Rasternahfeldmikroskops (s-SNOM) und die damit durchgeführte Spektroskopie eines Goldnanoteilchens, das mit dem Farbstoff TDBC ummantelt wurde.

Die Auflösung klassischer Mikroskope ist durch das Abbe-Limit auf Größenordnungen des sichtbaren Lichts begrenzt. Im Gegensatz zu klassischer Mikroskopie nutzt ein s-SNOM auch evaneszente Anteile des Lichtfeldes und kann dieses Limit damit umgehen. Dadurch kann es Auflösungen im Nanometerbereich erzielen. Durch die hohe Auflösung können auch Spektren von einzelnen Teilchen aufgenommen werden.

Ein s-SNOM entsteht durch die Kombination eines AFMs, dessen Nadel als Streuzentrum fungiert, und eines Konfokalmikroskops als Lichtquelle und Detektor. Bei Beleuchtung mit einem Laser entsteht in der Region zwischen Nadel und Probe ein elektrisches Nahfeld, das durch die Nadel wiederum in den Detektor gestreut wird. Die Region, in der das Nahfeld entsteht, ist durch den Durchmesser der Nadelspitze räumlich stark begrenzt, wodurch optische Informationen eines sehr kleinen Bereichs erhalten werden können. Durch das Rastern über eine Fläche lassen sich so optische Bilder aufnehmen mit einer höheren Auflösung als es klassische Mikroskopie erlaubt.

Wie diese Arbeit zeigt, sind mit dem s-SNOM Bilder mit einer Auflösung weit unter 100 nm möglich. Auch lassen sich teilweise Strukturen, die in einem AFM nicht erkennbar sind, auflösen, da ein s-SNOM die optischen Eigenschaften einer Probe untersucht. Auch diese Eigenschaft wird in dieser Arbeit vorgeführt.

Im zweiten Teil der Arbeit wird die Möglichkeit, mit dem s-SNOM Fluoreszenzspektren einzelner Teilchen aufzunehmen, diskutiert und demonstriert. Die untersuchte Probe besteht aus Goldnanoteilchen, die mit dem fluoreszierenden Farbstoff TDBC ummantelt wurden. TDBC bildet sogenannte J-Aggregate aus, die einen scharfen Absorptions- bzw. Emissionspeak verursachen. Die Anregungen dieser J-Aggregate koppeln stark an die Anregungen der Goldteilchen, was zu einem neuen Anregungszustand, einem sogenannten *Plexciton*, führt.

Die Existenz dieser Plexcitonen wird durch ein lokales Minimum im Absorptionsspektrum von TDBC-Gold-Präparaten bestätigt. Mit dem s-SNOM wird dann ein Fluoreszenzspektrum eines einzelnen Goldteilchens aufgenommen. Dieses Spektrum zeigt, dass das Auftreten der Plexcitonen die ursprüngliche Fluoreszenz der J-Aggregate fast komplett auslöscht und die Anregungen nur noch nichtstrahlend relaxieren.

Zukünftig könnte durch die Kombination des s-SNOMs mit gepulsten Lasern mit Pulslängen unter 10 fs die hohe Ortsauflösung mit hoher Zeitauflösung kombiniert werden und z.B. die Rabioszillationen im oben genannten Gold-TDBC-System beobachtet werden.

Contents

1	Introduction	1
2	Principle of an s-SNOM	5
2.1	Diffraction limit	5
2.2	Generation of a near field	10
2.3	Near field at an AFM tip	11
2.4	s-SNOM	17
2.5	Elimination of noise from the signal	18
2.6	Resolution limit of an s-SNOM	19
3	Set-up	21
3.1	AFM	21
3.2	Classical microscope	23
3.2.1	Construction	23
3.2.2	Test measurements	25
3.3	Confocal microscope	26
3.3.1	Construction	26
3.3.2	Test measurements	29
3.4	SNOM	31
3.4.1	Construction	31
3.4.2	Test measurements	32
4	Gold nanoparticles and J-aggregates	35
4.1	Dielectric function	35
4.2	Localised plasmons	41
4.3	J-aggregates	48
4.4	Strong coupling	51
5	Experiments	54
5.1	Preparation of samples	54
5.2	Spectra of uncoupled gold nanoparticles and TDBC	58
5.2.1	Absorption of gold nanoparticles	58
5.2.2	Formation of J-aggregates of TDBC	61
5.3	Spectra of TDBC coated nanoparticles	62
5.3.1	Absorption	62
5.3.2	Emission	63
5.4	Comparison between single and many particle spectroscopy	68
6	Conclusion and outlook	70
	Bibliography	73
	Selbständigkeitserklärung	79
	Danksagung	81

1 Introduction

Optical microscopy has always been an important tool to investigate the properties of nature on a small scale. In the 19th century Rayleigh [1] and Abbe [2] showed that the resolution of classical microscopy is restricted to the magnitude of the light's wavelength applied for investigation. Since light in the visible range is usually applied for microscopy this meant that structures with a size below approximately $0.5\mu\text{m}$ could not be resolved.

However a lot of structures of scientific interest have sizes in the nanometre range. This can be biological specimen, chemical clusters or nanotechnological devices. Therefore a microscope that can optically resolve structures down to a few nanometres would be highly beneficial.

The first person who published the idea of applying the evanescent field of a light wave was Synge in 1928 [3]. He postulated a big improvement in resolution if a sample is illuminated through an aperture with a diameter of approximately 100nm . This aperture should be placed in a distance of less than 100nm and scanned over the sample pixel by pixel.

Technically it was impossible to implement this idea back in that time and the first to experimentally do so at least for microwaves were Ash and Nicholls in 1972 [4]. Using waves with a wavelength of $\lambda = 3\text{cm}$ they demonstrated a resolution of $\lambda/60$.

The invention of scanning probe technology eventually enabled an implementation of Synge's original idea. With a scanning tunnelling microscope (STM), developed by Binnig and Rohrer in 1982 [5] or an atomic force microscope, developed by Binnig et al. in 1986 [6] a precise control over the distance between sample and probe was possible.

These techniques were the basis for the first instruments that could take pictures in the visible spectrum with resolutions far below the applied wavelength. In 1984 Pohl et al. presented a technique based on an aperture on a sharp tip to image a sample at a resolution $\lambda/20$ [7]. Independently in 1983 Lewis et al. developed a microscope with a resolution of 50nm where the aperture was etched into a silicon disc [8]. Using the aperture as a near field source for optical microscopy, these devices are nowadays called aperture scanning near field optical microscopes (a-SNOM).

Microscopy in general needs a sufficient amount of light illuminating the sample. However for very small apertures, the transmitted light intensity decreases strongly with the diameter [9]. This reduces the minimum aperture size to around 50nm [10]. Since the aperture size defines the minimum resolution of a device, this means, that with the method suggested by Synge the resolution cannot be much better than 50nm .

In 1986 Wessel proposed the idea that instead of irradiating an aperture a small scatterer could be brought close to the surface that could then be radiated with a laser [11]. A locally

enhanced field would be created that could serve as a light source. In analogy to an a-SNOM the resulting device is today called scattering SNOM or s-SNOM.

Wessel's idea was first implemented by Fischer and Pohl in 1989 [12] and improved over the years. Today resolutions down to 3 nm were obtained [13] for visible light.

Another great feature of near field microscopy is the fact that the resolution does not depend on the wavelength of the applied light. Therefore also infrared microscopy can have resolutions down to a few nanometres. Thus also in the infrared regime resolutions of down to $\lambda/500$ could be obtained [10].

In the last century also other methods were successfully developed to resolve structures smaller than the limit predicted by Abbe and Rayleigh, e.g. the already mentioned AFM and STM or the transmission electron microscope by Knoll and Ruska [14]. These instruments however react on different properties of the sample like topography or electron density. A SNOM in contrast is sensitive to the optical properties of a material. Another idea to enable optical microscopy with a resolution on a nanometre scale (stimulated emission depletion (STED) microscopy) was established by Hell and Wichmann in 1994 [15] and experimentally realised by Klar and Hell in 1999 [16].

The first part of this work documents the successful construction of the first s-SNOM built in the group for ultrafast dynamics in condensed matter at the university of Potsdam under the direction of Matias Bargheer. The microscope was not only installed to enable pictures of nano sized structures but also to investigate plasmonic systems using the SNOM's ability to probe strongly localized electric fields as for example discussed by Zayats and Smolyaninov [17] or Kawata [18].

The group for ultrafast dynamics in condensed matter is specialised on pump-probe experiments applying ultrashort laser pulses to execute time resolved measurements on a femtosecond time scale. This expertise could in future be used to couple the SNOM with a 6 fs phase stabilized pulse laser to obtain an experimental set-up that can measure on a femtosecond and nanometre scale simultaneously. A similar system was for example constructed by Furube et al. [19].

Chapter 2 of this thesis introduces the theoretical background of an s-SNOM, starting with the motivation and the explanation of the classical resolution limit and the idea that applying the near field of an electromagnetic wave can overcome this restriction. Afterwards the generation of such a near field is discussed followed by the calculation of the electric near field between an AFM tip and an arbitrary surface. This leads to an explanation of the actual functionality of an s-SNOM. Later in the chapter, noise reduction techniques and the resolution limit of the device will be discussed.

Chapter 3 presents the actual set-up of the device, starting with an AFM as a basis and the installation of a classical optical microscope. Thereafter the construction of a confocal microscope is shown and the combination of the different parts to obtain a scattering near field optical microscope. Besides the set-up, exemplary measurements, that shall illustrate the applicability of the single parts, will be presented in the chapter.

Another possibility of using this SNOM is to do single particle spectroscopy. It is superior to far field spectroscopy in the sense that only a small region of a sample is illuminated. This means also that only this region contributes to the spectrum. Assuming a sufficient size of the particles or a sufficiently low density on the sample, spectra of single particles can be recorded. This diminishes effects caused by inhomogeneities of a sample. Such inhomogeneities can be caused by size and shape differences of the optically active particles as well as differences in their chemical environment and smear out the peaks in the spectrum.

To demonstrate the applicability of the constructed SNOM as a single particle spectrometer, the second part of this work presents the results of single particle fluorescence spectroscopy of gold nanoparticles that were coated with the fluorescent dye 5,5',6,6'-tetrachloro-1-1'-diethyl-3,3'-di(4-sulfobutyl)-benzimidazolocarbo-cyanine (TDBC).

Due to plasmonic resonance gold nanoparticles absorb and scatter light in the visible range. Their exact scattering and absorption characteristics depend on their size and shape and are thus easily tunable. This property makes them interesting for applications for example in material science, nanotechnology or medical engineering.

Gold nanoparticles were already used (though not yet understood) in the fourth century by Romans to stain glass [20]. Later in the 19th century a method of photography using gold nanoparticles was developed by Herschel [21].

The understanding of the properties of those nanoparticles started with Faraday in the 1850s [22] and was fully developed by Mie in 1908 [23].

Today gold nanoparticles are for example used as labels in electron microscopy [24] or for local enhancement of electric fields for surface enhanced Raman spectroscopy (SERS) [25]. They can also be used in components of nano sized plasmonic waveguides [26]. Nanoparticles coated with organic complexes can be found in promising applications like nanoscale pH meters [27] or light harvesters [28].

In this case gold nanoparticles were coated with TDBC. TDBC is an organic dye forming J-aggregates [29]. Such J-aggregates are self-organised supramolecular assemblies of molecules caused by attractive van-der-Waals-like forces [30]. Electric excitations of the dye are delocalised over the whole aggregate and cause a shift of the absorption energy compared to that of the monomers.

J-aggregates have been discovered independently by Jelley [31] and Scheibe [32] in the 1930s. They both discovered a shift of the absorption peak of pseudoiso-cyanine chloride for higher dye concentrations. Scheibe also found the right qualitative explanation for the shift as an effect of polymerisation of the dye.

Today J-aggregates are used as optical sensitiser [33], laser active media [30] or fluorescent tags [34]. In future also applications as light sources or in laptop displays might be possible [30].

The excitations in J-aggregates (excitons) and the excitations in gold nanoparticles (plasmons) are strongly coupled when the gold is coated with TDBC. This means plasmons and excitons can no more be treated independently but must be seen as a new combined system, the plasmon-exciton or plexciton.

These new excitations show new properties like new absorption energies and fluorescence characteristics. An energy splitting in the gold absorption occurs. The original properties of both gold nanoparticles and J-aggregates are mutually modified, resulting in new nanoparticle-based complexes with unique characteristics distinct from either the nanoparticle or molecular adsorbate properties alone [35].

The theoretical foundations of gold nanoparticle-TDBC compounds will be presented in chapter 4. To understand their properties, the dielectric function of gold will be discussed, leading to an explication of localised surface plasmons in gold nanoparticles. The occurrence and properties of J-aggregates will be explained and the situation of strong coupling will be discussed.

After these theoretical foundations are clarified, the experiments will be presented in chapter 5. The actual measurement was a single particle fluorescence spectrum measurement of TDBC coated gold nanoparticles conducted with the s-SNOM. This will be presented and discussed at the end of the chapter. Before, the preparation of samples and preliminary experiments will be shown. The absorption spectrum of gold and the transmission and fluorescence spectra of TDBC will be discussed. This is necessary for the interpretation of the spectra of the gold particle-TDBC compounds. To prove that the particles coated with TDBC indeed give rise to strong coupling between plasmons and excitons, absorption and fluorescence spectra of TDBC coated gold nanoparticles will be shown. The chapter ends with a comparison between single particle and many particle spectroscopy which shows that single particle spectra show smaller linewidths of the peaks since they are not inhomogeneously broadened.

The conclusion and an outlook in chapter 6 sums up the work that was done and discusses potential future investigations using the constructed s-SNOM .

2 Principle of an s-SNOM

Conventional microscopy is an important and well-established tool for investigating nature on a small scale. However, as shown by Abbe and Rayleigh this method's resolution is limited to micrometre range. Many biological structures, devices in nanotechnology as well as other structures of scientific interest have sizes on a nanometre scale.

A scattering scanning near field optical microscope (s-SNOM) can overcome the limitations of classical microscopy. Its spatial resolution reaches down to a few nanometres yielding a huge improvement compared to the conventional optical techniques.

This high resolution can be used to take spectra of single particles or small structures. Its main advantage is a much higher precision since studying ensembles of particles always induces a broadening of spectral peaks caused by structural and environmental inhomogeneities (i.e. different sizes and shapes of particles lying in different regions of the sample). This inhomogeneous broadening leads to a loss of spectral information. This single particle spectroscopy will be discussed in the chapters 4 and 5 of this work where fluorescence spectra of TDBC coated around gold nanoparticles will be presented.

This chapter discusses the limitation of conventional microscopy and motivates the usefulness of evanescent waves for high resolution images (section 2.1), their generation (section 2.2) and their properties close to an AFM tip (section 2.3). Afterwards the actual functionality of an s-SNOM will be presented (section 2.4) followed by a discussion about possibilities to filter out the relevant information from a detected signal in section 2.5. Eventually, section 2.6 discusses possible restrictions in the resolution of an s-SNOM.

2.1 Diffraction limit

This section discusses the limitations of conventional microscopy presenting the Abbe limit and another equivalent criterion defining the resolution limit. This second limit, called *uncertainty criterion*, shows that the main reason for these limits is the fact that spacial information is lost when only light far away from the specimen is recorded. This insight is the main motivation for the development of a near field microscope.

The Abbe limit is the generally accepted restriction for the resolution of structures in optical microscopy. It specifies the minimum separation between two light sources that may be resolved into distinct objects [36]. In classical optical microscopy an objective is used to collect the light emitted from an area of interest which is then projected on an observation plane.

The limit says that two objects whose distance d_{Abbe} is smaller than

$$d_{Abbe} = 0.61 \frac{\lambda_0}{NA} \quad (2.1)$$

(where NA describes the objective's numerical aperture) cannot be distinguished using light with the vacuum wavelength λ_0 or bigger.

This limit is not a natural law. It is rather a reasonable definition. It implies that the light intensity distribution of a point source in an optical instrument due to interference looks the same as the scattering pattern of a circular aperture. It is of the form $I \sim (J_1(r)/r)^2$ where $J_1(r)$ describes the Bessel function of the first order [36] and r the space vector in the plane orthogonal to the direction of propagation. The shape of this function is shown in figure 2.1(a). It is not a sharp line but broadened and has side lobe peaks.

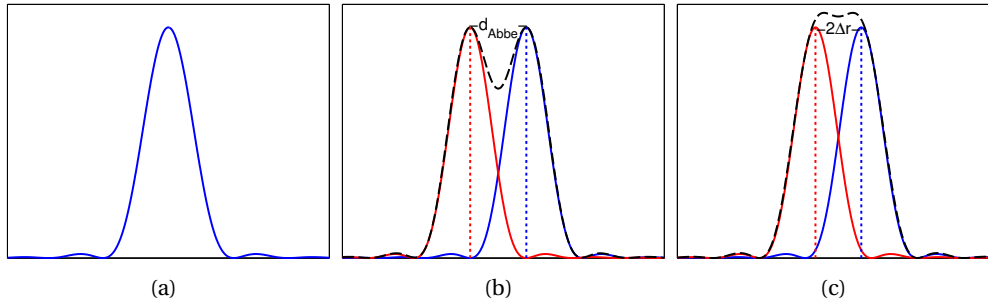


Figure 2.1: Light intensity distribution for one (a) or two (b), (c) point sources. The dashed black lines represent the sum of the two functions. In (b) they are separated by the Abbe limit the maxima lie above the other's minimum. In (c) their distance is given by twice the distribution's deviation, this means they are closer to each other. Therefore in (c) the intensity pit between the maxima is less deep than that for the Abbe limit in (b).

The Abbe criterion now states that two points can no more be distinguished when they are at least so close that the one's intensity maximum coincides with the other's first minimum as shown in figure 2.1(b). The light intensity seen from the two point sources is given by the sum of the single sources. When those two point sources come so close to each other that the dip in the combined intensity is too small they cannot be distinguished. Theoretically this dip could always be resolved, but in practice noise leads to a minimum contrast between dip and maximum to be distinguishable [20].

The limit can be understood by looking at figure 2.2, where two sources move so close to each other that they cannot be seen separately anymore.

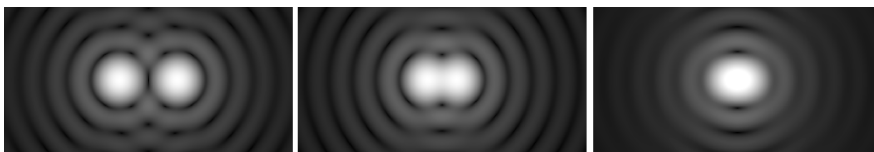


Figure 2.2: The spatial light distribution of two point sources. When they get too close to each other, they cannot be distinguished anymore. Modified from [37].

The exact derivation of Abbe's formula i.e. of the intensity distribution of a point source is not part of this work but can be found in the standard text books about optics (e.g. in [20]).

We can, however, understand its existence and its magnitude by looking at the k -space of electromagnetic fields.

From Fourier analysis of an electrical field one obtains that for a photon [20]

$$\Delta r \Delta k \geq 1. \quad (2.2)$$

This equation implies that the values for the position and its Fourier transform, the k -vector, of a photon are given by probability distributions. Δr describes the standard deviation of the spatial component and Δk the standard deviation of the k -vector. It can be seen as the equivalent to Heisenberg's uncertainty principle.

This uncertainty of space and momentum (i.e. the k -vector) enables another criterion for a resolution limit in microscopy: Similarly to the Abbe limit, two points are considered undistinguishable if their spatial distributions are so close that the areas within their standard deviations overlap, i.e. if their distance $d_{ucer} < 2\Delta r$ [20]. This criterion is more general than Abbe's since it does not imply a certain distribution in r - or k -space. A comparison of the two criteria shows that this *uncertainty criterion*, as will be called hereafter, is reasonable:

For this comparison the same spatial distribution as for the Abbe limit is assumed (see figure 2.1(c)). This means $I \sim (J_1(r)/r)^2$ where the intensity I is proportional to the probability that a photon originates from a point r .

For such a distribution twice the standard deviation is $2\Delta r \approx \pi$, whereas the Abbe limit is given by $d_{Abbe} = 1.22\pi$. That means the uncertainty criterion is of the same magnitude as the Abbe limit, but a little more optimistic. Graphically this means that between two point sources, separated by $2\Delta r$, the minimum of the combined intensity is less deep than for two points separated by the Abbe limit (figure 2.1(c)).

Actually, an integral over $(J_1(r)/r)^2$ does not converge for infinite boundaries. This means it is strictly spoken not possible to calculate a deviation for this distribution. However the small side lobes can be neglected and new integration boundaries be defined. For this case, besides the maximum, three side lobes on each side were included in the integration. The value for the deviation depends on those boundaries, which means, the value for the minimum distance in the uncertainty criterion for such a distribution is more an approximate value to motivate the reasonableness of this criterion.

As mentioned, this uncertainty criterion is also valid for other distributions and it is possible to find a physical lower bound for it. This fact is discussed in the following part, which consequently will show that too few available k -vectors give rise to the restricted resolution in conventional microscopy.

The uncertainty principle (equation 2.2) holds also in two dimensions, i.e. a plane [20]. That means for a photon with a certain energy emitted from a point source located in the xy -plane it holds:

$$\Delta r_{xy} \Delta k_{xy} \geq 1 \quad (2.3)$$

where r_{xy} describes the place in the plane and k_{xy} the k -vector component parallel to the plane.

The corresponding electrical field \mathbf{E} can, without loss of generality, be described by a plane wave with an amplitude E_0

$$\mathbf{E} = \mathbf{E}_0 e^{i\mathbf{k}\mathbf{r}}. \quad (2.4)$$

From the energy (respectively the wavelength) we can determine its k -vector:

$$k = \frac{2\pi n}{\lambda_0}. \quad (2.5)$$

Here λ_0 describes the vacuum wavelength of the photon and n the refractive index of the medium in which the photon propagates.

Via

$$k_{xy}^2 + k_z^2 = k^2 \quad (2.6)$$

which can easily be derived from figure 2.3, one can obtain information about the k -vector's component in the xy -plane.

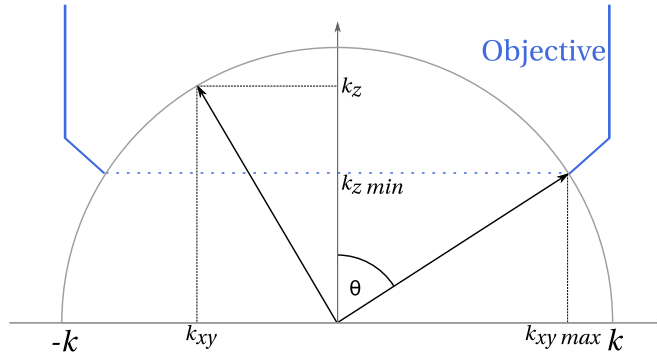


Figure 2.3: Sketch of the accessible vectors in the xy -plane. The maximum value is given by the maximum angle at which light can still be collected.

Classical microscopy enables us only to look at fields far away from a sample, this is distances much bigger than the wavelength of the applied light. For imaginary k_z the electrical field far away from the sample is zero, since in equation 2.4 $e^{ik_z z} \rightarrow 0$ for imaginary k_z and long distances to the origin z . This means we can only detect real k_z which means $k_z^2 \geq 0$.

In practice, the objective is not able to collect all photons but only those which are emitted within an angle θ around the z -axis. This means (as can be seen in figure 2.3 as well) that

$$k_z \geq k \cos(\theta). \quad (2.7)$$

This inequation holds only because k_z is real since otherwise the two values would not be comparable at all. This feature (equation 2.7) can be used in equation 2.6:

$$k_{xy}^2 = k^2 - k_z^2 \leq k^2 - k^2 \cos^2(\theta) = k^2 \sin^2(\theta). \quad (2.8)$$

This restriction for k_{xy} ($k_{xy} \in [-k \sin(\theta), k \sin(\theta)]$) leads to an upper bound for its deviation since the latter cannot be bigger than the maximum range of available k_{xy} -vectors, independent of the k -vector distribution:

$$\Delta k_{xy} \leq 2k \sin(\theta) = 2n \sin(\theta) \frac{2\pi}{\lambda_0}. \quad (2.9)$$

The factor $n \sin(\theta)$ defines the numerical aperture NA of the objective. Using this and inserting equation 2.9 into equation 2.3 leads to

$$\Delta r_{xy} \geq \frac{\lambda_0}{4\pi \text{NA}}. \quad (2.10)$$

This is a physical lower bound for the standard deviation in r in conventional microscopy. So regardless of the actual distribution of k -vectors, equation 2.10 means that, following the uncertainty criterion, two point sources cannot be distinguished if their distance d_{ucer} is smaller than

$$d_{ucer} = \frac{\lambda_0}{2\pi \text{NA}}. \quad (2.11)$$

This factor is 1.2π times smaller than the minimum distance given by Abbe. The reason for this is the differently assumed distribution of k -vectors. As mentioned, for the Abbe limit a spatial distribution of $I \sim (J_1(r)/r)^2$ was assumed. For this distribution also the uncertainty criterion gives a value that is around π times bigger than the lowest limit given by equation 2.11.

To get to this extreme value the maximum deviation $\Delta k = 2k \sin(\theta)$ was assumed. This can only be achieved by a distribution where the k -vectors have the extreme values $k = \pm k \sin(\theta)$ and no k -vectors in between. For the distribution assumed for Abbe the k -vectors are more evenly distributed and by that the standard deviation in k -space gets smaller. From equation 2.3 follows that the uncertainty in r -space then becomes bigger. This explains the difference between the lower resolution bound and the Abbe limit.

Taking this into account the magnitude of the Abbe limit becomes clear. In particular this criterion shows that the reason why classical microscopy is not able to resolve smaller objects is the fact that only fields with real k_z -vectors can be detected (which results in a decreased Δk). This means parts of the k -vector information are lost. This loss of image information directly translates to a lower resolution.

This section showed that being capable of also using the part of the electromagnetic field with imaginary components (i.e. evanescent fields) one should be able to receive more information and by that have a better resolution. Due to their fast decay and small expansion

these evanescent components are called a *near field*. The next section discusses the question where those near fields occur or how they can be created.

2.2 Generation of a near field

As mentioned earlier, we would like to use also the evanescent components of the electromagnetic field to exceed the Abbe limit. But where do near fields occur?

Following the original idea by Synge [3] one could use a laser for illuminating a sub-wavelength aperture brought close to a surface. The field behind such an aperture contains a strong near field component as shown by Bethe [38] and Bouwkamp [39]. Bringing a small aperture close to the sample as near field source is a well established idea [40] and devices using an apertured fibre are commercially available.

Yet, the drawback of this method is that here the resolution is restricted to a few tens of nanometres since the light intensity transmitted through the aperture decreases strongly for small aperture diameters [9]. This means, for too small apertures the light signal is too weak to be used. However the resolution cannot be better than the aperture's diameter [20].

Another possibility for creating a near field can be derived from Babinet's principle [41]. This states that the scattering pattern of an aperture, away from the incident direction, is the same as that of an opaque disc of the same size. Consequently a near field can also be created by radiating a small tip.

This idea can also be understood by another approach: Every dipole that is radiated by light scatters this light. The scattered field contains also a near field component, which is dominant in the region where the distance to the dipole is much smaller than the wavelength [41].

Since the electrical behaviour of every atom irradiated by light can be approximated by that of a dipole, basically every material irradiated by light causes a near field. In addition, the *lightning-rod-effect* states that fields are particularly strong at sharp edges [42]. Thus a strong electric near field exists in close proximity to a small tip that is radiated by a light source [20]. This mechanism was employed to build a microscope with a spatial resolution exceeding the classical diffraction limit.

In practice the scattering tip has to be brought very close to the region of interest. This can be achieved by using a scanning tunnelling microscope (STM) or an atomic force microscope (AFM) where the tip's position above the sample can be controlled precisely via the tunnelling current or the atomic force feedback, respectively. In both cases, the distance between tip and sample is in the order of a few tens of nanometres.

2.3 Near field at an AFM tip

For this work an AFM was used as the basis of an s-SNOM. It has a very small tip that is kept oscillating at a constant mean distance of a few tens of nanometres above the region of interest.

This section shows the derivation of the electric field between the tip and the sample when the system is irradiated with a laser. The tip is placed at $x = y = 0, z = d$, whereas the sample lies in the xy -plane at $z = 0$. To calculate the electric field, the section basically follows the concept of a review by Atkin et al. [9], where the authors show electrical field enhancement of the irradiating light between tip and sample.

To calculate the field we assume that the tip's apex diameter a and the distance between tip and sample d are much smaller than the light's wavelength used for irradiation. Doing so, the electric field can be considered to be constant over the whole region. In that case it is sufficient to find a solution for the electrostatic case and later include the factor of harmonic time dependence $e^{i\omega t}$ [41].

The tip's apex is approximated as a polarisable sphere above a planar substrate [9]. The incoming light represented by the electrical field \mathbf{E}_{inc} induces a polarization

$$\mathbf{p}_{sph} = \alpha_{sph} \mathbf{E}_{inc} \quad (2.12)$$

where the polarizability α_{sph} is given by the Clausius-Mossotti relation [42]

$$\alpha_{sph} = 4\pi\epsilon_0 a^3 \frac{\epsilon_{tip} - 1}{\epsilon_{tip} + 2}. \quad (2.13)$$

Here ϵ_{tip} describes the dielectric function of the tip's material. This polarised sphere can be treated as a dipole with the dipole moment \mathbf{p}_{sph} .

The dipole scatters the light and the respective near field is given by [41]

$$\mathbf{E} = \frac{1}{4\pi\epsilon_0} [3\mathbf{n}(\mathbf{n} \cdot \mathbf{p}) - \mathbf{p}] \frac{1}{r^3}. \quad (2.14)$$

Here \mathbf{n} describes the normal vector from the dipole to the point of interest and r their mutual distance.

To calculate the field between sphere and plane we use the method of image charges. That is, the surface charge induced by the dipole gives rise to an electric field. This field can be described like that of another dipole placed beneath the surface at $z = -d$ (see figure 2.4) which will be referred to as image dipole.

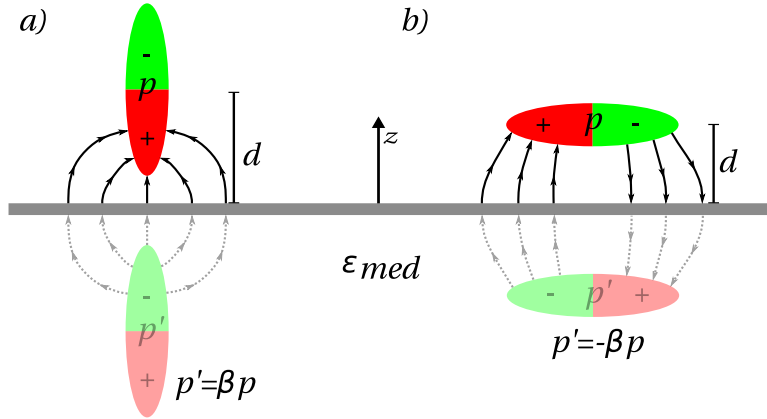


Figure 2.4: Field lines of a dipole located in air at a distance d above a medium with dielectric function ϵ_{med} . The surface lies in the xy -plane. In (a) the dipole's axis is perpendicular to the surface in (b) it is oriented parallel to the surface. The relative strength of the image dipoles is given by β (a) or $-\beta$ (b).

The image dipole's dipole moment \mathbf{p}' is not the same as \mathbf{p} but given by

$$\mathbf{p}' = c\mathbf{p}. \quad (2.15)$$

The following part discusses this factor c that results from applying continuity boundary conditions to the electric field on both sides of the surface [20]. These conditions state that the tangential component of the electric field has to be continuous as well as the orthogonal component of the displacement field, that means

$$E_{xy,air}(\mathbf{r})|_{z=0} = E_{xy,med}(\mathbf{r})|_{z=0} \quad (2.16)$$

and

$$D_{z,air}(\mathbf{r}) = D_{z,med}(\mathbf{r}) \quad \Rightarrow \quad E_{z,air}(\mathbf{r})|_{z=0} = \epsilon_{med}E_{z,med}(\mathbf{r})|_{z=0}. \quad (2.17)$$

The subscripts air and med refer to the region above and below the surface, respectively. E_{xy} and E_z describe the electric field component parallel and perpendicular to the surface, D_z the displacement field's component perpendicular to the surface and ϵ_{med} the dielectric function of the medium.

The factor c in equation 2.15 depends on the dipole's orientation in regard to the surface. That is why it is necessary to distinguish two different cases: First, a dipole whose orientation is perpendicular to the surface, afterwards, one parallel to the surface. From those two cases all possible orientations can be described via the superposition principle.

In the first case the dipole moment is parallel to the normal vector of the surface. That means $\mathbf{p} = p\mathbf{e}_z$. Above the surface the field of the induced surface charge is described by the field of an image dipole with the dipole moment \mathbf{p}' placed at $z = -d$. The fields of the two

dipoles, given by equation 2.14, sum up to the total electric field in air:

$$\begin{aligned} \mathbf{E}_{air} = & \frac{p}{4\pi\epsilon_0} \left(\frac{x(z-d)}{r_1^5} \mathbf{e}_x + \frac{y(z-d)}{r_1^5} \mathbf{e}_y + \left[\frac{(z-d)^2}{r_1^5} - \frac{1}{r_1^3} \right] \mathbf{e}_z \right) \\ & + \frac{p'}{4\pi\epsilon_0} \left(\frac{x(z+d)}{r_2^5} \mathbf{e}_x + \frac{y(z+d)}{r_2^5} \mathbf{e}_y + \left[\frac{(z+d)^2}{r_2^5} - \frac{1}{r_2^3} \right] \mathbf{e}_z \right) \end{aligned} \quad (2.18)$$

where $r_1 = \sqrt{x^2 + y^2 + (z-d)^2}$ describes the distance to the dipole and $r_2 = \sqrt{x^2 + y^2 + (z+d)^2}$ the distance to its image.

Below the surface the field can be derived by filling the whole space with the medium. To take this into account, the original dipole has to be replaced by a fictional dipole p'' at the same place $z = d$. In that case the electric field below the surface is

$$\mathbf{E}_{med} = \frac{p''}{4\pi\epsilon_0\epsilon_{med}} \left(\frac{x(z-d)}{r_1^5} \mathbf{e}_x + \frac{y(z-d)}{r_1^5} \mathbf{e}_y + \left[\frac{(z-d)^2}{r_1^5} - \frac{1}{r_1^3} \right] \mathbf{e}_z \right). \quad (2.19)$$

Applying the boundary conditions, equation 2.16 leads to $p'' = (p - p')\epsilon_{med}$ and equation 2.17 to $p'' = p + p'$. Thus the image dipole moment is given by

$$\mathbf{p}' = \frac{\epsilon_{med} - 1}{\epsilon_{med} + 1} \mathbf{p} = \beta \mathbf{p}. \quad (2.20)$$

This describes the relative strength of the image dipole in case of perpendicular polarisation as $c_z = \beta$.

The analysis of a dipole parallel to the surface is similar. With equation 2.14 the electric field is described by

$$\begin{aligned} \mathbf{E}_{air} = & \frac{p}{4\pi\epsilon_0} \left(\left[\frac{x^2}{r_1^5} - \frac{1}{r_1^3} \right] \mathbf{e}_x + \frac{xy}{r_1^5} \mathbf{e}_y + \frac{(z-d)x}{r_1^5} \mathbf{e}_z \right) \\ & + \frac{p'}{4\pi\epsilon_0} \left(\left[\frac{x^2}{r_1^5} - \frac{1}{r_1^3} \right] \mathbf{e}_x + \frac{xy}{r_1^5} \mathbf{e}_y + \frac{(z+d)x}{r_1^5} \mathbf{e}_z \right) \end{aligned} \quad (2.21)$$

above the medium and below the surface it is expressed by

$$\mathbf{E}_{med} = \frac{p}{4\pi\epsilon_0\epsilon_{med}} \left(\left[\frac{x^2}{r_1^5} - \frac{1}{r_1^3} \right] \mathbf{e}_x + \frac{xy}{r_1^5} \mathbf{e}_y + \frac{(z-d)x}{r_1^5} \mathbf{e}_z \right). \quad (2.22)$$

This time the boundary conditions give $p'' = (p + p')\epsilon_{med}$ and $p'' = p - p'$, which results in

$$\mathbf{p}' = -\frac{\epsilon_{med} - 1}{\epsilon_{med} + 1} \mathbf{p} = -\beta \mathbf{p}. \quad (2.23)$$

That means for a dipole parallel to the surface the relative strength of its image is given by $c_{xy} = -\beta$.

Now we discuss the case when the dipole and its image are oriented antiparallel. This can intuitively be understood by considering the slope of the field lines (figure 2.4). The electric field lines can only be drawn continuously if the dipole and its image are oriented parallel (in the perpendicular case) or antiparallel (in the planar case).

In an s-SNOM a laser irradiates the tip-sample region and the outgoing light intensity is recorded (figure 2.5). To approximate the field in that region the fields of the two dipoles and the incident field need to be added up. These fields shall be derived in the following part.

The electric field of the incoming light induces a dipole parallel to its polarisation. Thus the dipole's orientation depends on the incident angle of the (transversally polarised) light. Here an objective with numerical aperture of $NA = 0.82$ was used to focus the incoming light. This means that light in an angle of up to $\arcsin(0.82) = 55^\circ$ reached the tip-sample region. So the incoming light had components that were polarised parallel and components that were perpendicular to the surface. Due to this, both cases of dipole orientation need to be considered.

The following part therefore first discusses the electric field between tip and sample caused by an incident field with only components parallel to the surface. Afterwards the case will be discussed where the whole incident field is perpendicular to the surface. Superposition of the fields resulting from these two cases yields the solution for an electric field with arbitrary polarization.

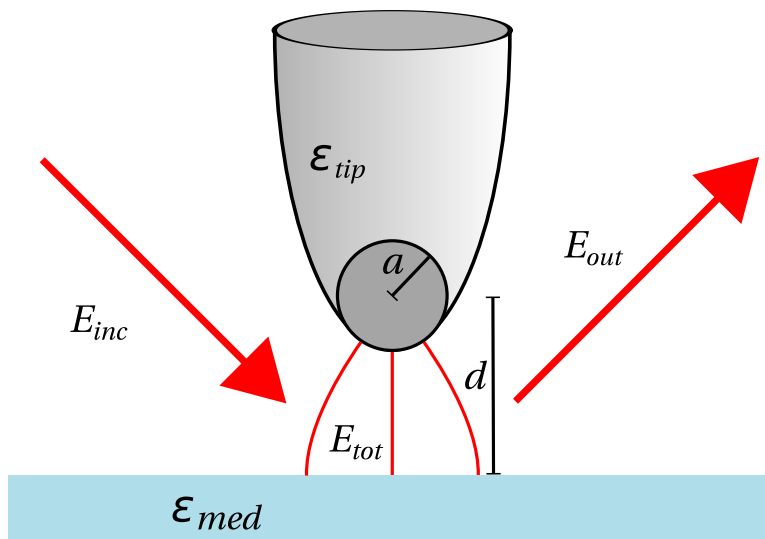


Figure 2.5: The tip is brought close to the sample and irradiated with a laser. The outgoing light is then measured.

First, an incident field only consisting of components in the xy -plane is discussed. It induces a dipole in the tip, whose dipole moment p_{xy} lies parallel to the surface. The tip's near field is given by equation 2.14 and directly beneath the tip it is

$$E_{xy,tip}(r) = -\frac{1}{4\pi\epsilon_0} \frac{p_{xy}}{r^3}. \quad (2.24)$$

The dipole moment is not permanent but caused by an electric field. That means both the incoming light and the field caused by the image dipole have to be included when calculating the dipole moment. The image dipole depends on the tip's dipole moment via equation 2.23. This correlation can be taken into account by defining an effective polarizability $\alpha_{eff,xy}$ via

$$p_{xy} = \alpha_{eff,xy} E_{inc,xy}. \quad (2.25)$$

On the other hand the dipole moment is given by equation 2.12, but now also the electric field of the image dipole E_{image} has to be considered:

$$p_{xy} = \alpha_{sph}(E_{inc,xy} + E_{image,xy}). \quad (2.26)$$

Using the expression for the electric field of a dipole to express $E_{image,xy}$ (equation 2.24) through the image dipole moment $p'_{xy} = -\beta\alpha_{eff,xy}E_{inc,xy}$, one obtains

$$p_{xy} = \alpha_{sph} \left(1 + \frac{\alpha_{eff,xy}\beta}{4\pi\epsilon_0(2d)^3} \right) E_{inc,xy} \quad (2.27)$$

from which the value for the effective polarizability reads as

$$\alpha_{eff,xy} = \alpha_{sph} \left(1 - \frac{\alpha_{sph}\beta}{32\pi\epsilon_0 \cdot d^3} \right)^{-1} \quad (2.28)$$

The electric field for any point between tip and surface (i.e. $0 < z < d$) results from adding up the contributions of the incoming field, the sphere and its image:

$$E_{tot,xy}(z) = \left(1 - \frac{\alpha_{eff,xy}}{4\pi\epsilon_0(d-z)^3} + \frac{\alpha_{eff,xy}\beta}{4\pi\epsilon_0(d+z)^3} \right) E_{inc,xy}. \quad (2.29)$$

Of course there are also other parts of the resulting electric field, e.g. the direct interaction between the incoming light and the surface, that were not considered in the calculation for E_{tot} . However these components do not carry relevant information and will be filtered out anyway (see section 2.5).

Now, let us look at an incident field perpendicular to the surface that means only with a z -component is discussed. In this case the field beneath the dipole results from equation 2.14 as

$$E_z(r) = \frac{1}{2\pi\epsilon_0} \frac{p_z}{r^3}. \quad (2.30)$$

Analogous to the parallel case an effective polarizability needs to be defined:

$$p_z = \alpha_{eff,z} E_{inc,z}. \quad (2.31)$$

Again, the dipole moment can also be expressed by

$$p_z = \alpha_{sph}(E_{inc,z} + E_{image,z}). \quad (2.32)$$

Now the image dipole moment shall be parallel to the sphere dipole, this is $p'_z = \beta \alpha_{eff,z} E_{inc,z}$. Inserting this into the expression for a dipole field in z -direction (equation 2.30) leads to an expression for $E_{image,z}$. This result can then be inserted into equation 2.32 and one obtains:

$$p_z = \alpha_{sph} \left(1 + \frac{\alpha_{eff,z} \beta}{2\pi\epsilon_0 (2d)^3} \right) E_{inc,z}. \quad (2.33)$$

The comparison between this and equation 2.31 leads to an expression for the polarizability in z -direction:

$$\alpha_{eff,z} = \alpha_{sph} \left(1 - \frac{\alpha_{sph} \beta}{16\pi\epsilon_0 d^3} \right)^{-1}. \quad (2.34)$$

The corresponding field in the region between tip and sample is again given by adding up the fields of the incoming light, the sphere and its image:

$$E_{tot,z}(z) = \left(1 + \frac{\alpha_{eff,z}}{2\pi\epsilon_0 (d-z)^3} + \frac{\alpha_{eff,z} \beta}{2\pi\epsilon_0 (d+z)^3} \right) E_{inc,z}. \quad (2.35)$$

The two expressions (equation 2.35 and equation 2.29) show that the electric field can be strongly enhanced in the tip-sample region, i.e. the local field is much stronger than the incident field. This can be caused by resonance in α_{eff} or β or by a very small distance between tip and sample d .

This enhancement is weaker for incident fields parallel to the surface since in that case, the sphere dipole and its image are antiparallel. By that their respective fields add up destructively and cause a differing sign in the second and third term of equation 2.29. For an incident field perpendicular to the surface the two dipole components add up constructively which causes an even stronger enhancement.

Atkin et al., in their review [9], come to different expressions for the electric field between tip and sample. Their enhancement is 8 times smaller than the result presented here.

Their deviation is identical and even the values for α_{eff} coincide with those from equations 2.28 and 2.34. Assuming that the step from the effective polarizability to the total field beneath the tip is correct, I do not see a reason why the values presented here might be wrong.

The enhancement is important for filtering out the signal carrying the relevant information from a very strong background (see section 2.5).

2.4 s-SNOM

Here the actual working principle of an s-SNOM is presented, showing that with such a device high-resolution pictures can be taken, that only depend on the optical properties of a specimen.

In an s-SNOM the tip scatters the very confined and enhanced field from equations 2.29 and 2.35 back through the objective [9]. The strength of the scattered field is proportional to the enhancement, i.e. the last two terms in the expressions for the field between tip and sample [10]. This back scattered signal can then be recorded as part of the outgoing light from the illuminated region.

The only variable in those equations is the dielectric function of the medium in the factor β . The other parameters like incoming light intensity and distance between tip and sample can be kept constant during any kind of measurement.

The difference in the near field between two points is therefore only given by the different dielectric functions of the areas beneath the tip. That means, one can scan over a certain area by defining a grid on the latter and measure the near field point by point (i.e. pixel by pixel). The near field's area is always restricted to the region of the tip's apex. Therefore a scan results in a picture with a resolution beyond the limit of conventional microscopy. This leads to the name *scattering scanning near field optical microscopy*.

In addition one can use an s-SNOM to take spectra of the small region beneath the tip. Inhomogeneities in size and shape cause slight differences in the response on incident light for different scatterers or sources of fluorescence. This leads to a *smearing out* of a spectrum if many particles contribute to it. Having only one or a few particles in the region beneath means only one or a few particles contribute to a spectrum recorded with SNOM. Therefore those spectra are more precise and effects that would be smeared out in many particle spectra can be resolved.

Scattering spectra can be obtained by illuminating the tip with a broad band of wavelengths and measuring the outgoing light depending on the wavelength. However scattering spectra should be interpreted carefully since not only the sample's response depends on the incident wavelength but also the response of the tip dipole as can be seen in the expression for α_{sph} in equation 2.13. This common response as shown in equations 2.29 and 2.35 makes drawing conclusions about the sample's properties complicated.

Fluorescence spectra are easier to interpret. There the tip is used to enhance the excitation field on a very confined area. The spectrum of the outgoing light shows the fluorescence spectrum of the particles placed beneath the tip. Since the exciting field is kept constant during one measurement the dependence of the enhancement factor of the wavelength does not disturb the fluorescence signal.

Now the working principle of an s-SNOM is clear. That means the occurrence of the signal and its detection. However besides the signal a lot of noise is recorded, too, and only in a few cases a system the way presented until now would be functional. To ensure general practicability, methods for discriminating the signal of interest from the noise need to be established.

2.5 Elimination of noise from the signal

As mentioned before, the signal is the outgoing light (back scattered or fluorescence) that is measured with a detector. However the laser spot of the irradiating light has a diameter of around 800 nm (as shown later in section 3.3) whereas the diameter of the tip, which defines the size of the tip-sample region, only has a diameter of down to 20 nm (manufacturer's data). But only the part of the light that originates from the tip-sample region carries relevant information. The rest of the signal has to be treated as noise.

Field enhancement as derived in the previous section helps a lot in improving the signal-to-noise ratio. However even to be at least as strong as the noise, the field between tip and sample has to be enhanced by a factor of 1600 since the area of the tip is of less than 0.1% of the laser's focus area. However even a signal-to-noise ratio of 1:1 is not optimal. For further improvement different methods were developed that can be used depending on what spectral region of the signal is desired.

For taking a reflection image, all the outgoing light is recorded. This means also, all wavelengths (or only that of the excitation light) are detected. In that case, obviously, all the disturbing part of the signal is recorded as well. To discriminate the part that carries the relevant information, one can make use of the fact that the tip is actually not kept constant at a certain distance to the sample but oscillating above the latter. Only the mean distance stays constant. Equations 2.29 and 2.35 show that the field enhancement strongly depends on the distance between tip and sample. This means the near field beneath the tip is modulated with the tip's oscillation frequency whereas the noise is hardly modulated and can be filtered out electronically. For this extraction a lock-in amplifier can be used, a device that can discriminate a signal with a given reference frequency and in addition amplify it.

A lock-in amplifier needs an analog signal to be able to discriminate unmodulated parts. If the photon flux is very small, which can occur for example in Raman scattering or fluorescence measurements, this is not the case anymore. Fortunately, for those examples the signal is detected at wavelengths that are not identical with the excitation wavelength, which means the latter can be eliminated with a colour filter.

2.6 Resolution limit of an s-SNOM

Theoretically the resolution of an s-SNOM is not limited [20]. For this the range of k -vectors in plane needs to be infinite and the AFM tip infinitely sharp. In reality mainly the tip's sharpness and the AFM's resolution define the resolution of an s-SNOM.

As shown earlier in section 2.3, the field is enhanced below the tip's apex. But this enhancement occurs at every place beneath the tip. Thus the region of the near field has a diameter of at least the tip's apex diameter. By that particles whose distance is smaller than the apex diameter can no more be distinguished as shown in figure 2.6(a).

This can be seen as a consequence of the fact, that particles in a SNOM picture seem to have at least the size of the apex (see figure 2.6(b)). This again means also particles which are smaller than the apex are no more mapped with their actual contours.

Not only the tip's diameter but also the actual resolution of the AFM define the resolution of an s-SNOM. It also depends on the sharpness of the tapering leading to the tip, and also on the sample. This can nicely be seen in figure 2.6(c). A SNOM picture needs to have the same mean distance to the sample at all times. However if a pit's edge is too steep and the AFM tip cannot reach the bottom of the pit the distance is no more the same. This disturbs the near field signal as well as it causes a wrong topography signal in the AFM: First the edge width in the picture is influenced by the tip's tapering sharpness, second, small particles lying next to such edges cannot be detected. This holds for both an AFM and an s-SNOM. By that the resolution of the SNOM cannot exceed that of the AFM.

Another factor that can have an influence on the resolution is the tip's height above the sample [20]. Since this is bigger than zero, not all evanescent waves can overcome this distance. This again decreases the amount of accessible k -vectors and by that the resolution as shown in section 2.1.

Thus in practice several parameters can influence the resolution of an s-SNOM. Yet pictures with a resolution down to 3 nm were already recorded [13].

The resolution does not depend on the wavelength of the illuminating light. This is a big difference to conventional optical microscopy. Thus in the infrared regime resolutions of down to $\lambda/500$ could be obtained [10].

Summary: This chapter has shown the general working principle of a scattering near field optical microscope. Starting with the motivation of why the application of near fields can improve the resolution, the creation of near fields and their quantitative strength were shown. With these the functionality of an s-SNOM was explained and how the signal can be improved. Eventually the resolution of such a device was shortly discussed. Hence an overview over the theory of an s-SNOM was established.

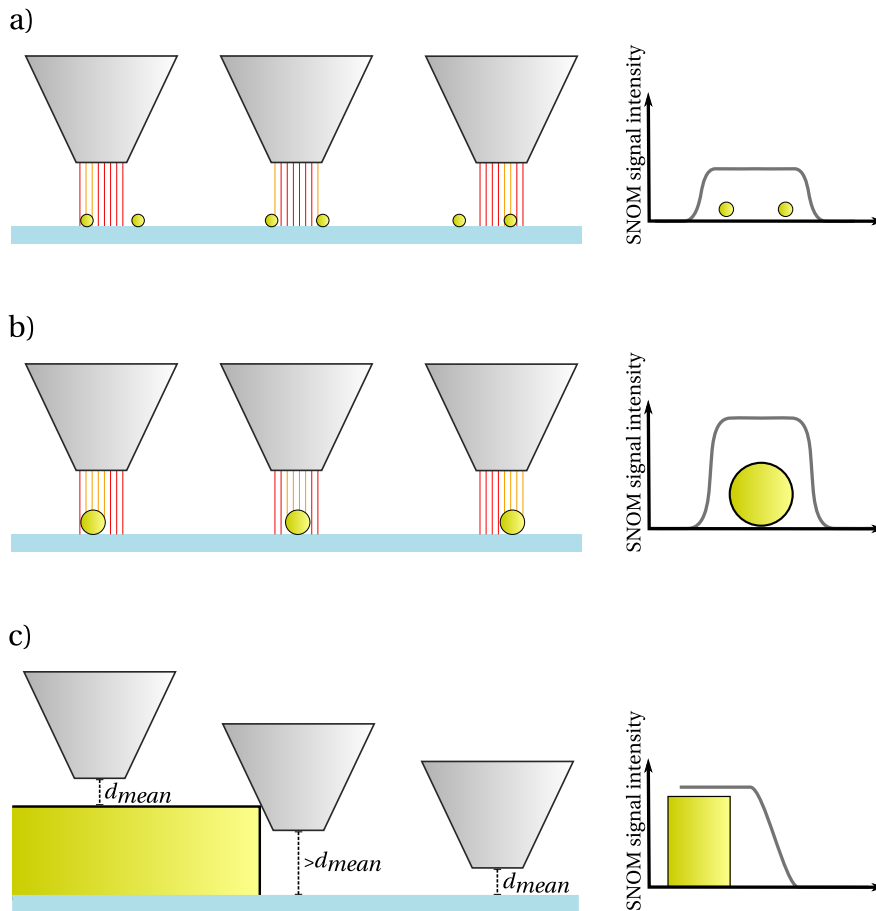


Figure 2.6: (a) shows an s-SNOM scanning over small particles who are separated by a distance of the size of the tip's apex. In all three situations the near field below tip causes approximately the same signal. Thus the particles can no more be resolved since the near field signal they cause is the same over the whole gap between them. A model of that situation is shown on the left, a sketch of the intensity pattern that would be recorded is shown on the right side of the figure. (b) displays the s-SNOM scanning over a structure smaller than the tip's apex. In all three situations the near field between tip and sample causes approximately the same signal. The object's contour can no more be resolved. Here, too, a sketch of the situation is shown on the left, the approximate intensity signal can be seen on the right side. (c) shows the influence of too sharp edges on the picture. Those cause a bigger distance between tip and ground due to the fact that the tip's shaft prevents the tip of coming close to the surface. The near field signal is disturbed and the edge cannot be resolved. Again the left side shows the situation whereas on the right side a potential intensity profile is displayed.

3 Set-up

After the introduction to the working principles of an s-SNOM in the last section, this section describes the successful process of building such a device. An atomic force microscope (AFM) served as basis (section 3.1). In it an optical objective was already included, which was then used to install a classical optical microscope (section 3.2) and a confocal microscope (section 3.3). By aligning the confocal part and the AFM's tip a s-SNOM was obtained (section 3.4). To show the functionality of the single components, in every section test measurements are presented.

3.1 AFM

The basis of the s-SNOM implemented in this work is a tapping mode AFM by Attocube. Tapping mode means a very sharp tip (ideally with only a few nm tip width) oscillates very close to a surface of interest. Tapping mode implies that the tip is brought so close that it taps the sample while oscillating.

If the height of the sample changes, the oscillation amplitude changes since its oscillation is blocked earlier or later. The amplitude is kept at a constant value. This means if the sample height changes, a feed back loop causes an adjustment in the tip's height. This height change can be recorded.

By scanning over a certain area the sample's height profile can be measured by recording how far the tip had to be moved in z -direction (i.e. out-of-plane direction) pixel by pixel. The resolution depends on the tip's apex size and its sharpness as discussed earlier in section 2.6.

The tip is an *Akiyama probe* (by NANOSENSORS) which is the tapered end of a silicon cantilever. This cantilever is glued to the prongs of a quartz tuning fork mounted on a titanium cube.

A sketch of this set-up is shown in figure 3.1. The system works as follows: A small dither piezo stack is glued in proximity of the tuning fork. It is excited to oscillate by a lock-in amplifier at a frequency between 40 and 50kHz. This oscillation causes the prongs of the tuning fork to oscillate, too. They move in plane and have opposite phases.

Since the cantilever is glued to the end of the prongs those ends are mechanically connected. This causes a twisting motion in the prongs when oscillating in antiphase. This twisting generates a vibration of the cantilever in z -direction (this is the axis of the tip), so its tapered end, i.e. the tip, oscillates in z -direction, too. The frequency is the same as that of the original dither piezo oscillation.

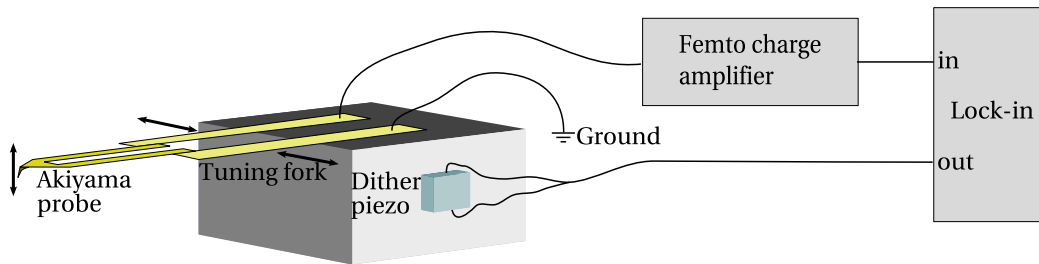


Figure 3.1: Working scheme of the AFM tip. The probe and its cantilever are glued to the end of a tuning fork. This is mounted on a cube that can be brought to oscillation by a dither piezo driven by a lock-in. The signal from the tuning fork is amplified by a femto charge amplifier and its amplitude measured by the lock-in.

The oscillatory response of the tuning fork is converted into a small amplitude dependent charge accumulation. This happens due to the piezo electricity of the quartz tuning fork. The accumulated charge is picked up at the electrodes mounted at the ends of the prongs. This charge signal is converted into a voltage and amplified by a charge amplifier by FEMTO. The output signal of the amplifier is then monitored by the lock-in amplifier. From that the oscillation amplitude, or at least a value proportional to the amplitude, can be recorded.

The excitation frequency is chosen to be on resonance with the tip. This can be obtained by measuring the tip response over a frequency range between 40 and 50 kHz and choosing the value with the highest amplitude.

This oscillation amplitude provides the signal for the feedback control. While approaching the tip to the sample surface the oscillation amplitude reduces (since it taps the surface earlier and earlier) and is kept constant at a certain set point by a feedback loop acting on the z -position of the tuning fork. This z -position is then recorded by the AFM software.

The sample (as well as the tip) can be moved in all three dimensions to be able to scan over a certain area. Figure 3.2 shows exemplary pictures to demonstrate the AFM's suitability. In figure 3.2(a) a test sample is shown. It consists of holes in a silicon oxide layer, which are approximately 800 nm wide and 20 nm deep with a respective distance of 2 μm (UMG 01 by Anfatec). These structures can be resolved nicely by the AFM.

Another example is given in figure 3.2(b) which shows gold nanoparticles. Those particles are of the size of only 80 nm but can still be resolved well.

For optical measurements the manufacturer had already installed an objective in the AFM (LT-ASWDO/0.82 by nanoSCOPY). It is, like the tip, located above the sample holder, thus the tip is located in the optical path between sample and objective. This objective has a numerical aperture of $NA = 0.82$ a focal length of $f = 3.96\text{mm}$ and a working distance of $d = 0.35\text{mm}$ for a spectral range of 350 nm-1600 nm. It is infinity corrected, which means a collimated light beam is focused on exactly one spot in the focal plane and the light of a point source in this plane is collimated by the objective. Unfortunately it is not chromatically corrected, so the focal plane is a bit different for every wavelength. This causes slight uncertainties when working with white light, but is of no consequence when only using one

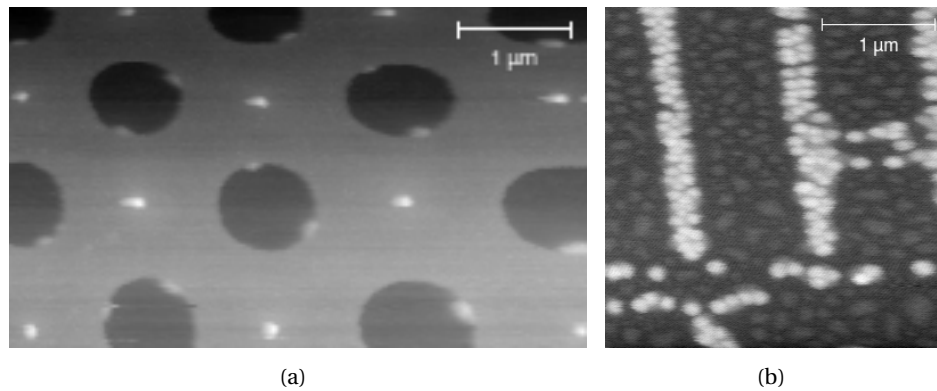


Figure 3.2: Test pictures by the AFM. a) shows a test sample consisting of ca. 800 nm wide and ca. 20 nm deep holes in a silicon oxide layer. The white spots represent tips from the production process. b) shows chains of gold nanoparticles.

wavelength. This objective was used as basis for further optical components that were installed in order to use the device as a scattering SNOM.

3.2 Classical microscope

To be able to take pictures (that means to be able to measure the light intensity on the whole sample at the same time) and to have a rough optical real time control over the area which the tip is scanning, a classical optical microscopy unit was installed. This means in essence, in addition to the already present objective the sample area had to be illuminated and a camera needed to be added.

3.2.1 Construction

The illumination path follows the Köhler illumination method [43], which provides uniform and bright illumination over the field of view, even for light sources that are not uniform. Figure 3.3 sketches the functional principle of Köhler illumination.

The main idea is to focus the lamp's filament image onto the objective's back focal plane in order to obtain an evenly illuminated area on the sample. In this case a quartz tungsten-halogen lamp was used. The light was collected by a lens with a focal length of $f = 5$ cm and subsequently collimated by a lens with $f = 20$ cm. After passing several apertures, each with a width of 1 inch, the light was focused to the focal back plane of the objective by a lens with $f = 20$ cm. The last aperture formed the field diaphragm, this is it defined the size of the lighted region on the sample and lay in the sample's focal plane. Then the objective collimated the light and created a smoothly illuminated area.

In practice the focus of this unit was to illuminate the area sufficiently to have a satisfactory optical control over the tip and the area it was moving on. The goal was not a perfect Köhler

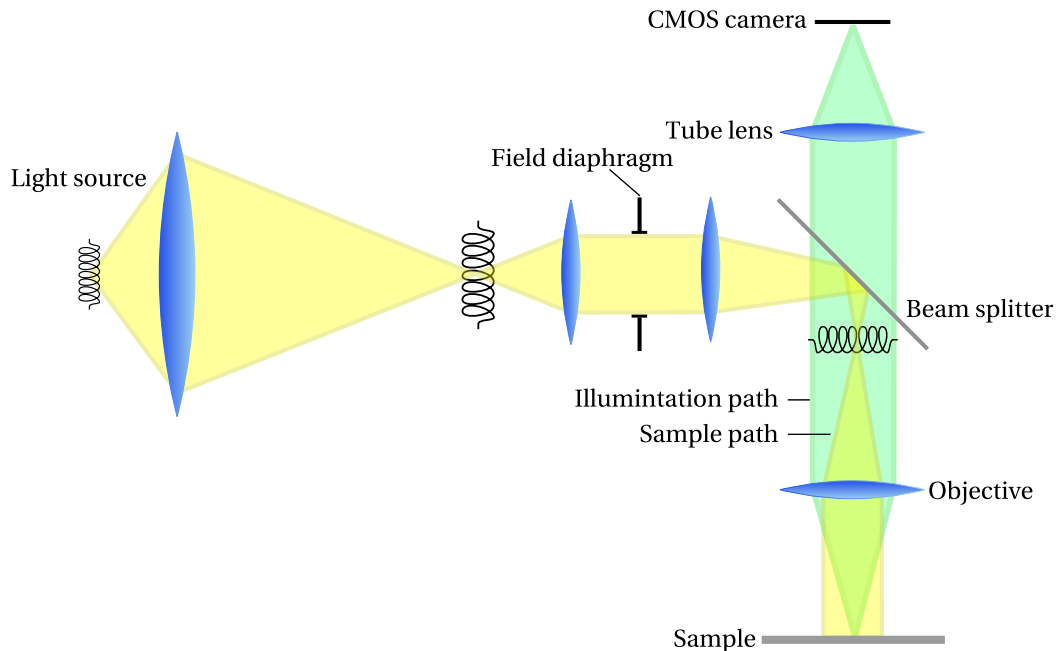


Figure 3.3: Scheme of a classical optical microscope using Köhler illumination for the light path and a CMOS camera as detector.

illumination. Therefore parts were used that were already at hand which did not necessarily fit perfectly but sufficiently. Due to this fact the distances between the single lenses were not always optimal. This caused in particular the light to be not perfectly collimated after the second lens but be a bit divergent. That's why a slight shade of the aperture could always be seen on the sample. Due to this the aperture (a necessary part of a mirror mount) was placed further away from the objective. Yet a slight shade is still visible in the top left corner of the pictures (see figure 3.4(a)). But as mentioned, the unit fulfils the tasks it is built for sufficiently.

To eventually visualize the area of interest the reflected light was detected by a CMOS chip (Thorlabs DCC1545M) with 1280 x 1024 Pixels. For that, the light coming from any spot on the sample was collimated by the objective and, after passing a beam splitter, focused on the chip by a tube lens with $f = 15$ cm. For normal optimal imaging, the camera should be in the focus plane of the tube lens.

However, to improve the optical control over the tip, the distance between lens and chip could be tuned with the help of an adjustable tube between the two. A bigger distance causes the focal plane to be closer to the objective, a smaller distance means the focal plane is further away. This means, with an adjustable distance, different planes could be in focus. By that it was possible to focus on the sample or on the tip's cantilever which lay in different planes by simply adjusting the distance between tube lens and CMOS chip.

After the installation of the described unit, it was possible to take pictures of small objects of the size of a few micrometres.

3.2.2 Test measurements

To obtain information about distances and sizes in those pictures, a picture of a known scale was taken (figure 3.4(a)). The distance between two bars is $10\mu\text{m}$. This means that the picture has a width of around $185\mu\text{m}$.

Due to the fact that the size of the monitored area also depends on the distance between tube lens and camera (i.e. the distance between sample and objective), the area seen by the camera can be of different sizes. To obtain the precise distance in a picture, the set up needs to be calibrated every time the distance between camera and tube lens are changed. For the present thesis this was not necessary since sizes and distances were not of actual interest, but the classical microscope was only used as a control device.

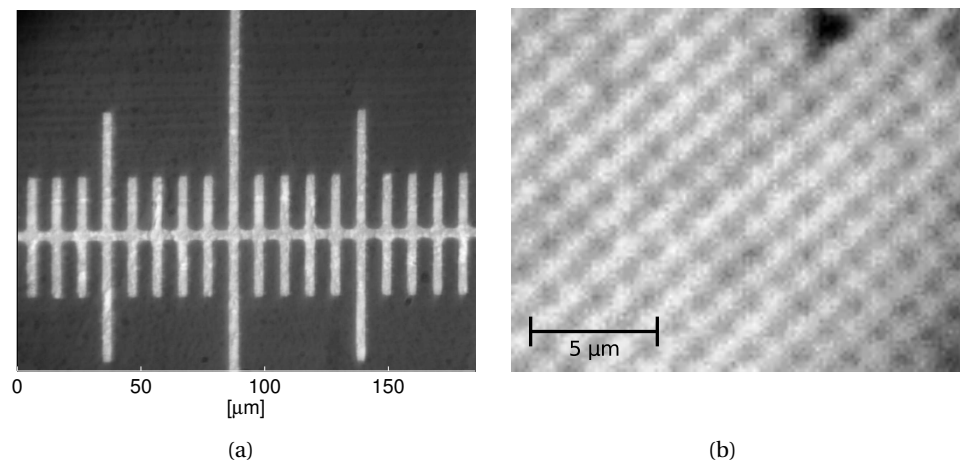


Figure 3.4: Picture of a known scale to be able to estimate distances on the sample (a). The distance between two bars is $10\mu\text{m}$ and the whole width of the picture is $185\mu\text{m}$. (b) shows the picture of a chess pattern whose holes are around 800nm wide. The distance between two holes is $2\mu\text{m}$. This pattern can still be resolved by the optical microscope.

It would also be convenient to have an approximate feeling for the resolution of this unit. To get this, a picture of a chess pattern was taken (UMG 02 by Anfattec). This was very similar to the one, used as example picture for the AFM (figure 3.2(a)). The hole diameters (800nm) and distances ($2\mu\text{m}$) were the same, only the holes were a bit deeper (58nm instead of 20nm).

The pattern could still be resolved by the microscope as can be seen in figure 3.4(b), which shows an excerpt of the chess pattern picture. This means that the resolution is at least as good as $2\mu\text{m}$. However the contrast between holes and plateaus is already rather low. If the holes were even closer, the noise would most likely cause the same signal intensity for holes and plateaus. This implies that the resolution is best $2\mu\text{m}$.

A better resolution would be surprising since the Abbe limit can only be obtained with an optimal instrument. Two reasons why this device does not fulfil these requirements shall be mentioned here: The first is the fact that the objective is not chromatically corrected. This causes a blur that reduces the resolution when illuminating with white light. Second, as

mentioned, the illumination is not ideal. This causes edges on the sample to cast shadows since the light is not perfectly collimated. This, too, causes a slight blur and reduces the resolution.

As mentioned earlier the classical microscope was only used for an optical control over tip and sample. For this a resolution of at least $2\mu\text{m}$ is completely sufficient. With this the area on the sample which shall be investigated by the AFM tip or by the laser spot of a confocal microscope can be selected easily. The confocal microscope is presented in the next section.

3.3 Confocal microscope

A confocal microscope is a part of every scattering SNOM. Its laser is used for illumination of the sample-tip area (see section 2.3) and its detection optics are used to measure the outgoing light. Additionally, a confocal microscope is a good instrument to take optical pictures with resolution at the Abbe limit and even three dimensional pictures. Its main idea is to only illuminate a small spot and eliminate all out-of-focus light.

This section discusses first the unit's construction (section 3.3.1) and afterwards its practicability (section 3.3.2).

3.3.1 Construction

In a confocal microscope a laser is focused on a spot and the reflection measured by a detector. To eliminate light from out-of-focus layers a pinhole is placed exactly in the image plane in front of the detector (see figure 3.5). This causes all light to be blocked that does not come from a point lying within the projected image of the pinhole in the sample plane. Hence this light does not disturb the signal. A sketch of its basic functionality can be seen in figure 3.5. If the sample is now movable, one can scan over a whole area and record the reflected light pixel by pixel. In the best case, this results in a diffraction limited image of the region.

The fact that out-of-focal-plane light is eliminated results in two other advantages of confocal microscopy: First, also thick samples can be examined, since it is possible to have a sharp focus also within a specimen. Second, an additional scan in the direction of the optical axis enables a three dimensional scan of an object.

It is also possible to eliminate the excitation wavelength in the outgoing light before detection. By this, fluorescence signals can be measured and fluorescence pictures at resolution limit can be recorded. In a non-scanning mode the spectrum of a very small area can be recorded and by that the fluorescence of a few or only a single particle can be measured.

To have a bigger variety in possibilities both for confocal and for scanning microscopy several lasers and two different detectors were used in this set up. The lasers that could be coupled into the objective (after being collimated) reached from 408 nm to 633 nm in the continuous wave regime.

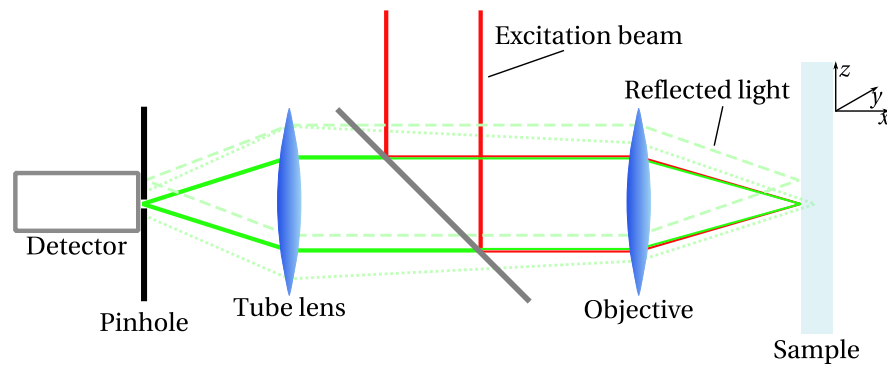


Figure 3.5: Sketch of the functionality of a confocal microscope. Points that reflect or emit light from a point away from the pinhole's image on in the sample plane are not detected. The sample can be moved in all three dimensions to focus and scan over a certain area.

To be able to separate incoming from outgoing light the excitation light passed a beam splitter before reaching the objective. This beam splitter was either a 50:50 broad band beam splitter, used for reflection images, or a long pass dichroic beam splitter, used for sensitive fluorescence images. The latter was reflective for wavelengths below approx. 530 nm and showed nearly 100% transmission for wavelengths above this threshold. This ensured, that long wavelength light like that from fluorescence could be guided to the detectors with only low losses, whereas the disturbing excitation light was almost completely filtered out.

The outgoing light could be guided on two ways: In the first possibility, a Si-detector (Thorlabs DET36A/M) was used to measure the scattered light. For this the light was focused on a pinhole by a tube lens with a focal length of $f = 10$ cm. The detector was placed directly behind the pinhole. The latter's size was chosen to be $50\mu\text{m}$. Its size will be explained in section 3.3.2.

The other possibility was used to measure spectrally resolved signals. For this the light was guided through a monochromator (Cornerstone 260m 1/4m by Oriel instruments). This was achieved by focussing the light with a tube lens ($f = 5$ cm) on the focal plane of a two lens system which collected the light and focused it into the monochromator. The two lens system consisted of a lens collimating the light originating from its focal plane with a focus length of $f = 7.5$ cm and a second lens with a focal lens with $f = 20$ cm focusing the light into the entrance slit of the monochromator.

A pinhole could optionally be placed in the focal plane of the two lens system to obtain a classical confocal microscope. However for very weak fluorescence signals, it was necessary to remove the pinhole. As presented earlier in section 2.5 the light carrying the information originates from the area beneath the tip. This is much smaller than the area cut out by the pinhole. Since the information was discriminated with a lock-in amplifier a missing pinhole would not worsen the resolution in an s-SNOM.

Behind the monochromator the light was detected by a photo multiplying tube (PMT). With this, also very weak signals could be recorded. This was handy since the fluorescence spectra presented in chapter 5 were indeed very weak and could not be recorded with the Si-detector. The whole set up can be seen in figure 3.6.

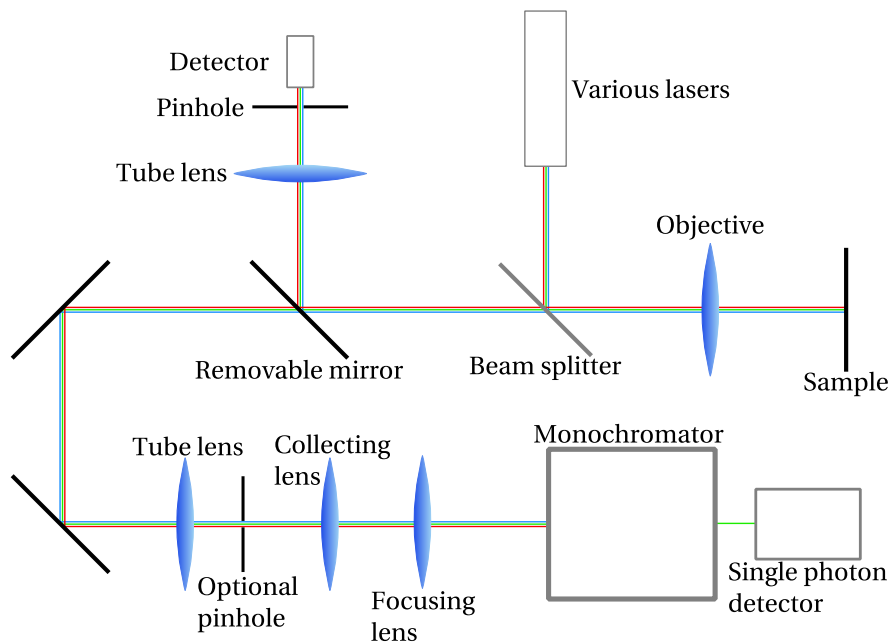


Figure 3.6: Light path in the confocal set up. With a folding mirror the light can either directly be focused on a detector or be lead through a monochromator and then on a single photon detector. The beam splitter could be switched (between 50:50 and long pass) depending on the needs of the current measurement.

The two microscope parts (the classical microscope and the confocal microscope) were connected by another beam splitter which reflected 90% of the light originating from the sample into the confocal part. This was done since fluorescence signals were very weak. These signals were not supposed to be recorded by the CMOS camera which only took reflection pictures. Thus it was sufficient if 10% of the light originating from the sample reached the camera. A sketch of the organisation of the two components is shown in figure 3.7.

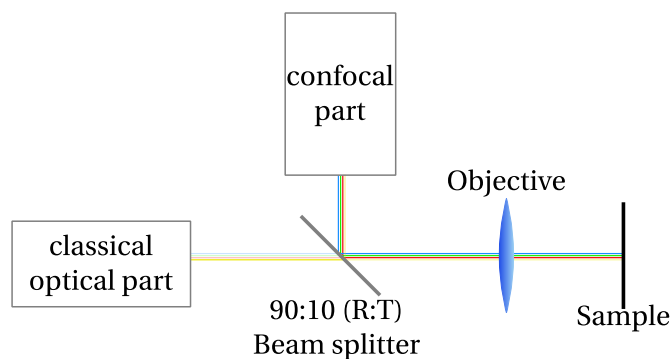


Figure 3.7: Light path in the confocal set up. With a folding mirror the light can either directly be focused on a detector or be lead through a monochromator and then on a single photon detector. The beam splitter could be switched depending on the needs of the current measurement.

3.3.2 Test measurements

The pinhole size has to be chosen as a compromise between signal strength and resolution. A smaller pinhole improves the resolution but also decreases the light intensity. To figure out which is the best solution for this set-up, a few test measurements were made with different pinhole sizes. The results can be seen in figure 3.8.

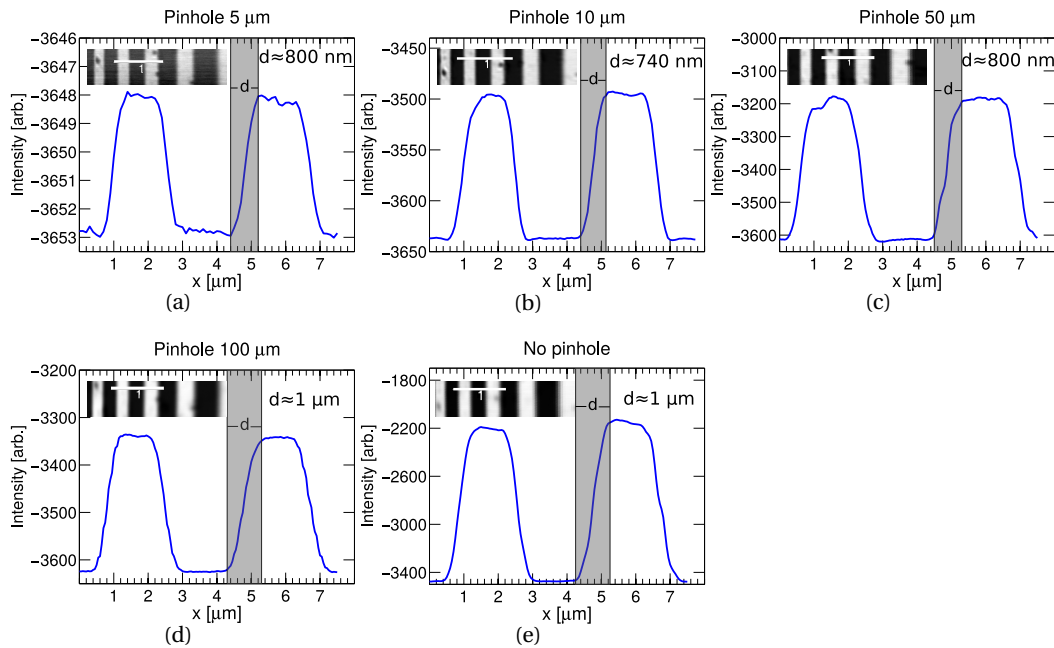


Figure 3.8: Test measurements of a reflective grid with the confocal microscope with different pinhole sizes of $5\mu\text{m}$ (a), $10\mu\text{m}$ (b), $50\mu\text{m}$ (c), $100\mu\text{m}$ (d) and without pinhole (e). The light was produced by a 543 nm cw-Laser and detected by the Si-detector. The graphs show the profile along the lines marked in the insets. The insets are taken from the original pictures and have a width of $20\mu\text{m}$ and a height of $5\mu\text{m}$.

In these measurements confocal pictures of a grid that consisted of reflective and non-reflective stripes with a width of $2\mu\text{m}$ were taken. A cw-laser was used with an emission wavelength of 543 nm and the reflected light was recorded by the Si-detector.

Apparently the pictures in the insets are distorted. This happened because the piezo scanning elements did not react linearly to the applied voltage but reacted hystereticly. Actually this distortion appeared already in the pictures of figure 3.2 but there the covered areas were much smaller, which is why the distortion is not as obvious. The distortions could in principle be corrected by a post processing algorithm that is not implemented yet, since up to now this has not been necessary. That is why the distances measured are not completely correct, but should be sufficiently precise as they were taken, from the center of the pictures where the distortion should be smallest.

To compare the different resolutions obtained with different pinhole sizes, intensity profiles were taken along certain lines in the pictures. The resolutions were obtained with the knife edge method as done for example by Lime et al. [44]:

The spot size of the whole system, the *total spot* size, is determined by the spot size of the laser and the projection of the pinhole on the sample. It can be approximated by the product of the intensity distributions of the laser spot and of the pinhole [20] (the intensity distribution of the pinhole projection means the intensity distribution in the focal plane if the pinhole was evenly illuminated from its back).

If this total spot scans over a sharp edge, the width of the edge in the signal gives the width of the spot. A mathematical argument for this is that the detected signal is given by the convolution of the system spot size and the profile of the sample [45]. For a sharp edge this profile is given by the θ -function. Its convolution with the system's total spot profile describes a broadened edge as seen in the profiles of figure 3.8. The width of the edge is as big as the spot size. Of course this depends how spot size is defined. In this case it is defined to the region where the intensity is noticeably different from zero.

This spot size defines the resolution analogous the argument used in section 2.6. Two particles separated by a distance smaller than the spot size cannot be distinguished. This means the profile of an actually sharp edge can be used to determine the resolution.

As expected, a confocal microscope without pinhole has the worst resolution (around $1\mu\text{m}$, figure 3.8(e)). Figure 3.8(d) shows that also a pinhole with a diameter of $100\mu\text{m}$ does not filter out enough out-of-focus light to cause a better resolution. A pinhole of $50\mu\text{m}$ already improves the resolution by around 20% and 800nm can be resolved as can be seen in figure 3.8(c).

In the three measurements discussed before the exposure time was 1 ms per pixel. For a pinhole with a diameter of $10\mu\text{m}$ this time had to be increased to 10 ms per pixel. Only by that enough light could be detected to receive a sufficient signal (figure 3.8(b)). On the other hand the best resolution was obtained in this measurement. It is around 740nm which is already comparable to the light's wavelength. For a $5\mu\text{m}$ pinhole the exposure time had to be increased further to 100 ms (figure 3.8(a)). This is also the most likely explanation why the resolution was worse compared to the $10\mu\text{m}$ pinhole. The difference between minimum and maximum of the signal is 50 times smaller than for the $10\mu\text{m}$ measurement and with that the bad signal to noise ratio reduces the resolution.

The best resolution is obviously obtained with a $10\mu\text{m}$ pinhole. However, the price is a much longer exposure time which might cause problems in more complex measurements. In addition in a SNOM measurement also other filter methods are applied (see section 2.5). So it is in general sufficient to use the pinhole with a diameter of $50\mu\text{m}$ which was done for the rest of this work. For the second detector the fibre input works as pinhole which also has a diameter of $50\mu\text{m}$.

The resolution of the confocal device is with $750\text{nm} - 800\text{nm}$ worse than predicted by the Abbe limit (equation (2.1) for a laser with a wavelength of 543nm). This is mainly caused by two reasons: First, the laser profile was far away from being evenly round but more half moon shaped. This caused the laser spot to be not perfectly focused on the smallest possible spot. Second, the criterion for the confocal resolution is different from the definition for the Abbe limit. This is due to the fact, that the intensity was assumed to be constant over the

whole spot size as was done in the discussion about the SNOM resolution. However the actual intensity distribution over the spot can be approximated by a Gauss curve [44]. Thus structures whose distance is a bit smaller than the measured spot size could still be resolved.

Hence the resolution of the presented confocal microscope is quite decent and was, in combination with the AFM, sufficient for the successful construction of a scattering SNOM as can be seen in the next section.

3.4 SNOM

According to the theory in chapter 2, an s-SNOM is obtained by aligning the AFM tip with the laser of the confocal part. In addition, a method to discriminate the noise from the desired information needs to be established. Thus, a lock-in amplifier was installed.

3.4.1 Construction

The lock-in was integrated by simply leading the detector signal to the input of the lock-in. As reference signal the driving voltage of the dither piezo of the AFM head was used. The reference signal defines the frequency on which the lock-in discriminates the signal. That means, only signals that are modulated with that frequency pass the lock-in while the rest is filtered out.

The alignment of the laser and the AFM tip happened in two steps: First, the tip was brought in the focal plane of the objective, then it was adjusted in plane to receive the maximum near field signal. For this a silver mirror was used as sample.

For a reflective sample the detected light intensity in a confocal microscope is strongest when the sample is placed in the focal plane of the objective. This feature was used to place the tip in the focus spot of the laser.

The tip was first roughly brought to the focal plane by bringing it in focus of the classical microscope so it could be seen sharply in the CMOS camera (section 3.2). For this the distance between camera and tube lens was chosen to be maximal so eventually the tip was slightly closer to the objective than the focal plane.

Afterwards, the silver mirror was inserted into the AFM and slowly brought closer to the tip until they were in contact. This contact could be recorded by recording the amplitude change of the tip's oscillation. Eventually when in contact with the tip, also the sample was slightly too close to the objective. So tip and sample were slowly moved back until the confocal signal was maximal and by that the tip sample region in the focal plane of the objective.

Afterwards the tip was moved to the laser spot. This could be controlled by the camera that before was moved closer to the tube lens so the laser spot was in focus. Fine adjustment was made by slightly moving the laser in plane until the signal detected through the lock-in was maximized.

Using a test sample and not only the tip alone was necessary since, as seen in section 2.3, the near field enhancement originates from the tip-sample interaction. However, once the tip was adjusted the sample could be removed and any other sample be inserted.

3.4.2 Test measurements

To see that field enhancement occurs and that the signal recorded by the lock-in originates from the tip-sample region, a tip scan was executed. That means, while the mirror sample was held fixed in the focal plane and the laser kept permanently on one spot the tip was scanned over the area around the laser spot. Both direct signal and that of the lock-in were recorded and are shown in figure 3.9.

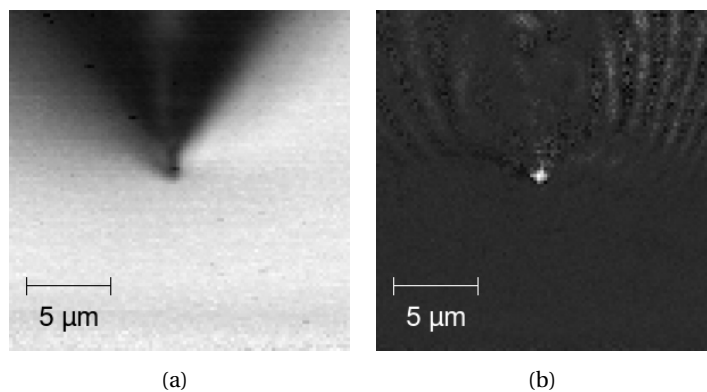


Figure 3.9: Tip scan over a reflective sample in the focal plane of the objective, illuminated by a laser spot. (a) shows the direct signal, (b) shows the signal discriminated by the lock-in on the tip's oscillation frequency. In the direct picture the shape of the tip can be seen nicely as a shadow, the SNOM signal shows a strong enhancement when tip and laser coincide.

In the confocal picture (figure 3.9(a)) the tip and the cantilever can be seen since if the laser hits them instead of the mirror the reflection is weaker. As the cantilever is higher than the tip it is not focused.

The picture obtained by leading the signal through the lock-in (figure 3.9(b)) shows one bright spot in its centre. A comparison with the confocal picture yields that this is where the tip crosses the focused laser. This means that in this situation a strong electric signal occurs that is modulated with the tip frequency. Thus this set-up indeed measured the scattered enhanced field derived in section 2.3.

The wave like artefacts that occur in figure 3.9(b) are caused by reflection of the laser from the cantilever since this also oscillates with the same frequency as the tip.

Now exemplary pictures are presented in figure 3.10. These pictures show that with the SNOM a comparable resolution as with the AFM can be obtained. For those measurements the gold particle chain sample was used that was already shown in figure 3.2(b) where it served as test sample for the AFM.

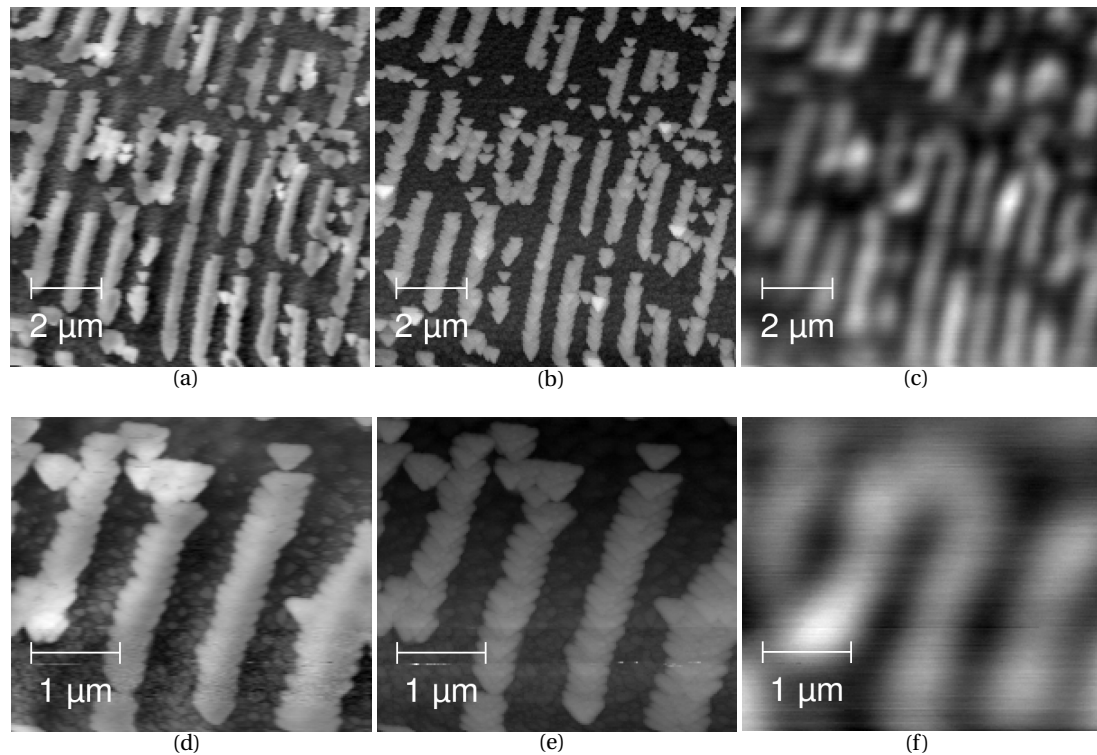


Figure 3.10: Test pictures of gold nanoparticle chains. The upper row shows a section of $10\mu\text{m} \times 10\mu\text{m}$, the lower one a section of $4\mu\text{m} \times 3.5\mu\text{m}$. The left column shows SNOM pictures, the central column AFM pictures and the right column confocal pictures of the same area respectively. The SNOM resolution is nearly as good as the AFM's and far better than the confocal resolution.

For a good comparison between the different techniques confocal, AFM and SNOM picture were recorded simultaneously. This means an AFM scan was executed, with the tip in focus of a 543 nm laser. The outgoing light was detected by the Si-detector. The detector signal was directly recorded by the AFM software to receive a confocal picture. Parallely the signal was connected to the input of the lock-in amplifier. The magnitude of the signal discriminated by the lock-in was then recorded by the same software. This resulted in the s-SNOM picture.

The SNOM pictures are shown in figures 3.10 (a) and (d), the AFM pictures in figures 3.10 (b) and (e) and the confocal pictures can be seen in figures 3.10 (c) and (f).

The pictures show the huge improvement in resolution from a confocal microscope to an s-SNOM. The SNOM pictures have a comparable resolution as the AFM pictures but, in contradiction to the latter, contain optical information about the sample instead of topographical information.

The lower row (figure 3.10 (d) and (e)) shows that the single gold particles can still be distinguished. However a comparison with figure 3.2(b) shows that the quality of the tip used for this measurement apparently was worse. There might have been some dust on the tip or a deformed apex. Therefore the particles show a triangular shape in the picture, which implies that the tip apex had a triangular shape itself. This caused a worse resolution in the

AFM and by that also limited the resolution of the s-SNOM. However these pictures confirm that it is possible to take SNOM pictures with the resolution of an AFM.

Another test measurement shows the advantages of sensing optical properties on a nano scale. In that measurement a picture was taken of a dried up film of TDBC with both SNOM and AFM. Both pictures are shown in figure 3.11.

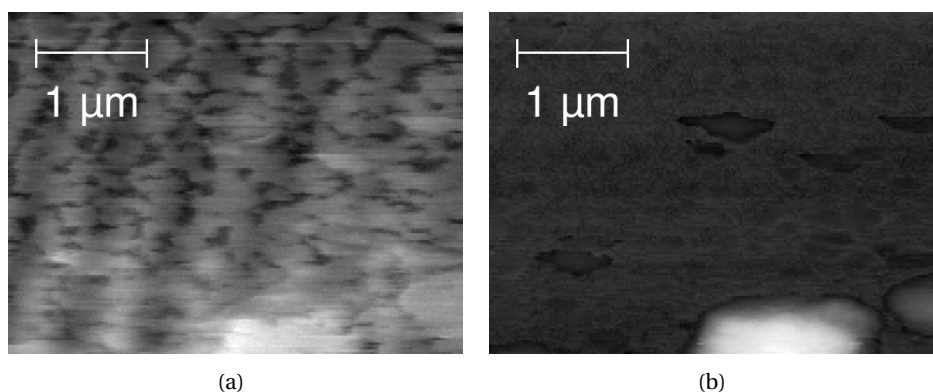


Figure 3.11: Image of a dried up TDBC film recorded with the SNOM (a) and the AFM (b). In addition to the structures that can be seen in both pictures (apparently dirt), the SNOM picture shows defects in the TDBC film, which cannot be seen in the AFM picture, since the height differences are too small.

The SNOM picture shows that the TDBC film is not uniform but has a lot of inhomogeneities. Since these inhomogeneities are not that deep, the AFM cannot resolve them topographically. The pattern can rudimentarily be seen but also changing the contrast cannot carve it out properly. In contrast, the inhomogeneities can be seen well in the SNOM picture due to the different optical properties of the different regions. These pictures show nicely the benefit of having an optical microscope with a resolution on the nanometre scale.

Summary: The last pictures in figures 3.11 and 3.10 show the great properties of this scattering SNOM. The resolution is comparable to that of the used AFM and sometimes even superior since optical properties instead of topological properties are investigated.

The AFM was presented in the beginning of the chapter as the foundation of the SNOM. To have optical control over the tip and the investigated region, a classical optical microscope was installed and presented in this chapter. The illumination and detection facilities were provided by a confocal microscope which was constructed with a variety of options in both illumination and detection. The combination of the compounds led to the nice high-resolution pictures at the end of this chapter.

4 Gold nanoparticles and J-aggregates

This work discusses the fluorescence spectrum of gold nanoparticles coated with TDBC. To obtain higher precision a single particle spectrum was recorded with the components of the s-SNOM introduced in the two previous chapters.

Due to their optical properties caused by plasmonic resonance in the visible light region gold nanoparticles were already used in the 4th century in stained glass [20]. The theoretical background was provided by Mie in 1908 [23]. Today gold nanoparticles find application for example as waveguides in plasmonic chains [26], in surface enhanced Raman spectroscopy [25] or as labels in electron microscopy [24].

To be able to interpret these spectra, understanding the theoretical interaction of gold nanoparticles with the incident light field is essential. For this, section 4.1 discusses the dielectric function of gold. The gold nanoparticles used for this work were considerably smaller than the wavelength of visible light. This allowed the formation of localised plasmons. These plasmons are resonant oscillations of the free electron gas in the particles. They strongly influence the electric behaviour of the gold nanoparticles and will therefore be discussed in section 4.2.

The coating material for the gold particles, TDBC, is a fluorescent dye forming J-aggregates. These are supramolecular assemblies of monomers caused by attractive van-der-Waals-like forces [30]. They were discovered in the beginning of the 1930s by Jelley [31] and Scheibe [32]. J-aggregates show strong red-shifted fluorescence compared to their monomers caused by dipole-dipole interaction of the transition dipole moments.

Today J-aggregates find application as optical sensitizers [33], laser active media [30] or fluorescent tags [34]. In future also applications as light sources or in laptop displays could be possible [30]. Section 4.3 discusses their optical properties.

The excitations in J-aggregates (delocalised excitons) are strongly coupled with the plasmons in gold nanoparticles yielding new optical properties like frequency splitting of the gold absorption peak or annihilation of the J-aggregate fluorescence as will be shown in the next chapter where the measurements will be discussed. The theory of strong coupling will be discussed in section 4.4.

4.1 Dielectric function

The dielectric function $\epsilon(\omega)$ describes the reaction of a metal to an external electric field. It determines the absorption and transmission behaviour of the metal. This section motivates

the form of the dielectric function of gold by modelling it with understandable physical effects. Thus an understanding of the form of the function in the visible range is obtained. In addition an acceptably precise quantitative description for wavelengths down to 500 nm is derived.

A metal reacts on an external electric field with a displacement of the charge carriers. Assuming that in a metal only conduction electrons get displaced, the displacement induces a dipole moment $\mathbf{p} = e\mathbf{r}$ for each conduction electron. Here \mathbf{r} describes the displacement and e the elementary charge.

Adding up all dipoles in a unit volume leads to the polarisation \mathbf{P} of the metal. Assuming the metal is isotropic, the dipoles of all displaced electrons are the same. This leads to

$$\mathbf{P} = n\mathbf{p} \quad (4.1)$$

where n is the number of conduction electrons in the unit volume.

The displacement field \mathbf{D} is given by the sum of the vacuum electric field and the polarisation:

$$\mathbf{D} = \epsilon_0\mathbf{E} + \mathbf{P}. \quad (4.2)$$

On the other hand for an isotropic metal it holds

$$\mathbf{D} = \epsilon_0\epsilon\mathbf{E}. \quad (4.3)$$

Here ϵ describes the dielectric function. In an isotropic medium \mathbf{E} and \mathbf{D} are parallel. In that case the two equations can be combined which leads to an expression for the dielectric function:

$$\epsilon = 1 + \frac{\mathbf{P}}{\epsilon_0\mathbf{E}}. \quad (4.4)$$

Solving the equations of motion for the electrons in an external electric field yields a value for the displacement r , resulting in an expression for the polarisation \mathbf{P} . This can be inserted in equation 4.4 to obtain a value for the dielectric function.

The Drude-Sommerfeld model assumes that, as already mentioned, only conduction electrons contribute to the polarisation and they can move freely with an effective mass $m_{e,con}$. However they can be scattered at unspecified collision centres (lattice ions, other electrons, defects, phonons, etc.) [46].

The equation of motion for a conduction electron in an external (oscillating) electric field reads as [20]

$$m_{e,con} \frac{\partial^2 \mathbf{r}}{\partial t^2} + m_{e,con} \Gamma \frac{\partial \mathbf{r}}{\partial t} = e \mathbf{E}_0 e^{-i\omega t}. \quad (4.5)$$

\mathbf{E}_0 is the amplitude of the electric field and ω its frequency. The movement of the electrons is damped by the factor Γ . This Γ is the reciprocal value of the mean free movement time τ . This free movement time describes the average time between two scattering events and can be calculated via the Fermi velocity v_f and the mean free path l of a conduction electron. This means [47]

$$\Gamma = \frac{1}{\tau} = \frac{v_f}{l}. \quad (4.6)$$

This model assumes an infinite crystal, so there are no restoring forces acting on the displaced electrons. Equation 4.5 can be solved with the ansatz $\mathbf{r} = \mathbf{r}_0 e^{-i\omega t}$. Inserting the solution into equation 4.1 leads to an expression for the polarisation:

$$\mathbf{P} = - \frac{ne^2 \mathbf{E}_0}{m_{e,con}(\omega^2 + i\Gamma\omega)}. \quad (4.7)$$

This result can be used in equation 4.4 to obtain a value for the dielectric function

$$\epsilon_{Drude}(\omega) = 1 - \frac{\omega_p^2}{\omega^2 + i\Gamma\omega} \quad (4.8)$$

where $\omega_p = \sqrt{ne^2/(m_{e,con}\epsilon_0)}$ denotes the plasma frequency of the metal. This expression can be divided into real and imaginary part:

$$Re[\epsilon_{Drude}](\omega) = 1 - \frac{\omega_p^2}{\omega^2 + \Gamma^2}, \quad (4.9a)$$

$$Im[\epsilon_{Drude}](\omega) = \frac{\Gamma\omega_p^2}{\omega(\omega^2 + \Gamma^2)}. \quad (4.9b)$$

These two values have different physical meanings. The relation between displacement field and electric field in equation 4.3 ($\mathbf{D} = \epsilon_0 \epsilon \mathbf{E}$) yields that the real part of the dielectric function describes the in-phase component, whereas the imaginary part describes the out-of-phase component of the metals response to the electric field.

The in-phase component results in dispersion and the ability to store electric energy. The out-of-phase component gives rise to loss of electric energy within the metal.

Figure 4.1 displays a comparison between the literature values taken from Johnson and Christie [48] and the values derived from the Drude-Sommerfeld model. For this the values $\omega_p = 13.8 \cdot 10^{15} \text{ s}^{-1}$ and $\Gamma = 1.59 \cdot 10^{13} \text{ s}^{-1}$ were taken from Novotny and Hecht [20].

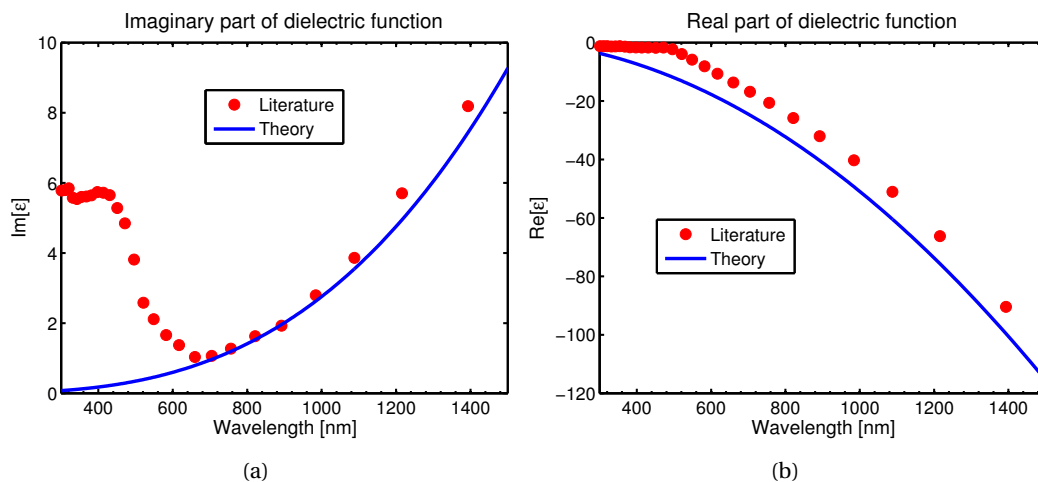


Figure 4.1: Comparison between the dielectric function $\epsilon(\omega)$ derived from the Drude-Sommerfeld model and the literature values from Johnson and Christie [48], (a) shows the imaginary part, (b) the real part. For wavelengths higher than approx. 650 nm the model agrees with the literature values, apart from a small offset in the real part.

For large wavelengths, above approx. 650 nm, the model matches the measured values quite well (except for a constant offset in the real part, which will be discussed later).

For small wavelengths the model can no more predict the actual behaviour of the dielectric function. This is due to the fact that until now it was assumed that only conduction electrons contribute to the dielectric function. However if the radiation energy is big enough electrons bound in filled bands below the Fermi surface can be excited to the conduction band. Naturally these excitations influence the metal's reaction on external electric fields, too.

To take these transitions into account when modelling dielectric constant, they can be classically approximated by an oscillator model for the electrons [20]. Their equation of motion then reads as

$$m_{e,int} \frac{\partial^2 \mathbf{r}}{\partial t^2} + m_{e,int} \gamma \frac{\partial \mathbf{r}}{\partial t} + \alpha \mathbf{r} = e \mathbf{E}_0 e^{-i\omega t}. \quad (4.10)$$

Each interband transition needs to be described with another oscillation with different parameters. $m_{e,int}$ describes the effective mass of the electrons taking part in the respective transition. γ is the damping constant. In the case of bound electrons it is mainly caused by radiative damping. A term that did not appear in the equation of motion for conduction electrons is the term $\alpha \mathbf{r}$. It is caused by restoring forces on the electrons that keep them in place. α can be interpreted as the spring constant of these forces.

The solution of this equation can be used to calculate the contribution of an interband transition to the dielectric function of a metal. Analogous to the Drude case one obtains [20]

$$\epsilon_{interband}(\omega) = 1 + \frac{\tilde{\omega}_p^2}{(\omega_0^2 - \omega^2) - i\gamma\omega}. \quad (4.11)$$

This term is very similar to the Drude term (equation 4.8). However, in this case $\tilde{\omega}_p = \sqrt{\tilde{n}e^2/(m_{e,int}\epsilon_0)}$ does no longer describe the plasma frequency of the metal, but only an analogous parameter. Here \tilde{n} was used for the density of electrons contributing to the interband transition.

Another difference to the Drude term is the existence of an eigenfrequency $\omega_0 = \sqrt{\alpha/m_{e,int}}$. This eigenfrequency is caused by the restoring forces (that do not exist for free electrons) and defines the energy where such an interband transition takes place.

The dielectric function caused by an interband transition can be divided into a real and an imaginary part, too:

$$Re[\epsilon_{interband}] (\omega) = 1 + \frac{\tilde{\omega}_p^2(\omega_0^2 - \omega^2)}{(\omega_0^2 - \omega^2)^2 + \gamma^2\omega^2}, \quad (4.12a)$$

$$Im[\epsilon_{interband}] (\omega) = \frac{\gamma\tilde{\omega}_p^2\omega}{(\omega_0^2 - \omega^2)^2 + \gamma^2\omega^2}. \quad (4.12b)$$

To now model the dielectric function of gold, these interband contributions need to be added to the Drude part of ϵ . In reality numerous of such interband oscillations need to be summed up to obtain a precise model of the dielectric function.

Qualitatively, one can imagine the interband contributions far away from their resonance as follows: Every interband transition has a certain eigenfrequency ω_0 . At frequencies far below this threshold $\omega \ll \omega_0$, the electrons can "follow" the electric field immediately and are thus in phase. Therefore this oscillation is loss-free and contributes only to the real part of the dielectric function with a constant that can be approximated from equation 4.12 to $\epsilon(\omega \ll \omega_0) \approx 1 + (\tilde{\omega}_p/\omega_0)^2$.

At frequencies much higher than the resonance $\omega \gg \omega_0$ the electrons can not follow the electric field anymore. Hence in that region they do not contribute to the value of the dielectric function. This behaviour is sketched in figure 4.2. For comparability ϵ is here plotted against the wavelength $\lambda = 2\pi c/\omega$ with $\lambda_0 = 2\pi c/\omega_0$.

This behaviour leads to the fact that contributions of all interband transitions whose resonance frequency is higher than in the region of interest can be added up to one constant (real) value ϵ_∞ in that region. Not having done that in the Drude-Sommerfeld model explains the offset in the real part for wavelengths above 650 nm. This offset can be overcome by adding such a constant ϵ_∞ .

The Drude-Sommerfeld model can be improved a lot by including the first interband oscillation with the values $\tilde{\omega}_p = 45 \cdot 10^{14} \text{ s}^{-1}$, $\gamma = 1.42 \cdot 10^{14} \text{ s}^{-1}$ and $\omega_0 = 2\pi c/\lambda$ with $\lambda = 450 \text{ nm}$ (from Novotny and Hecht [20]). Adding now a constant offset $\epsilon_\infty = 6$ (from Novotny and

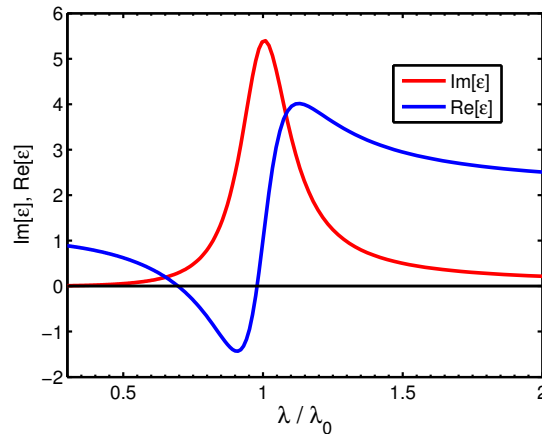


Figure 4.2: The qualitative behaviour of the dielectric function at an interband transition around its resonance wavelength. The imaginary part differs from zero only for frequencies close to λ_0 . The real part shows a constant offset for wavelengths much bigger than λ_0 and equals one for smaller wavelengths.

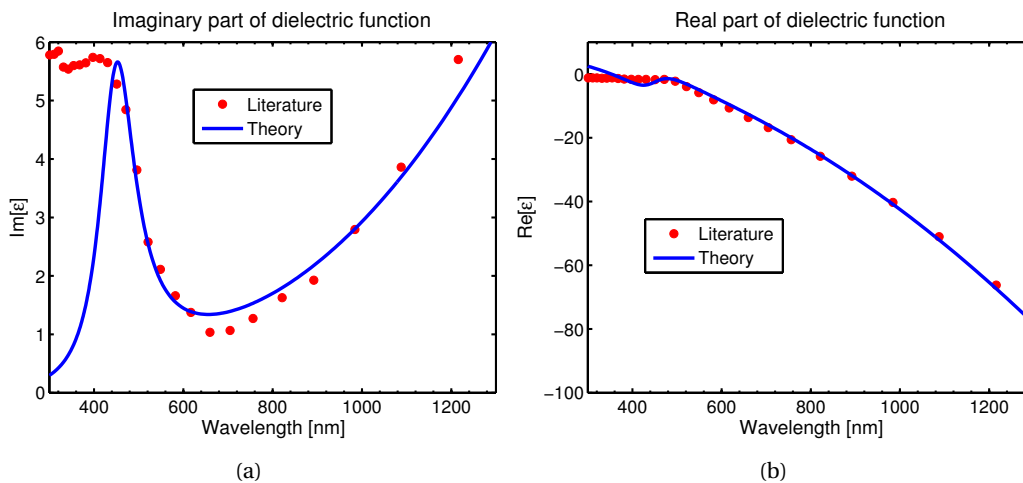


Figure 4.3: Comparison between the model and the literature values from Johnson and Christie [48]. The model agrees well with the values for wavelengths above 500 nm.

Hecht [20], too) leads to an acceptable approximation of the literature values for wavelengths down to 500 nm as can be seen in figure 4.3.

The approximation is a convenient way to understand and approximate the dielectric function of a metal. In practise the band structure of gold is very well known. Therefore this oscillator model is no more necessary, but the dielectric function can be simulated quite precisely as done by Guerisi et al. [49].

This section should mainly give an overview on how the dielectric function of gold approximately looks and on the physical reasons for this. For gold nanoparticles this function gives rise to the occurrence of localised plasmons who determine the spectroscopic behaviour of particles as shown in the following section.

4.2 Localised plasmons

Plasmons describe the collective oscillations of the free electron gas in a metal caused by an external electric field. Different kinds of plasmons occur: Bulk plasmons represent the collective longitudinal oscillation of the electron plasma in bulk metals. Surface plasmon polaritons can be described by propagating waves along the surface of metals.

Localised plasmons are non-propagating excitations of the conduction electrons of metallic nanostructures coupled to the electric field. These modes arise due to the restoring forces at the particles' surface exerting on the driven electrons. Thus a resonance can arise, leading to a field amplification both inside and in the near field zone outside the particle.

These localised plasmons dominate the optical properties of gold nanoparticles. Due to the plasmons' dependence on size and shape of the particles these optical properties are easily tunable making them interesting materials in nanotechnology [26], surface enhanced Raman spectroscopy or even photography [21].

The goal of this section is to understand the occurrence of such resonant plasma oscillations and by that the reaction of gold nanoparticles to an external electric field. For this the electrostatic potential in the region inside and around the particle will be derived. The potential solutions needs to fulfil the boundary conditions. For the surface these conditions were already introduced in section 2.3, others occur at the particle's centre and at large distances to it.

Similar to the derivation of the near field at an AFM tip in section 2.3, the region of interest is assumed to be much smaller than the wavelength of the incoming light. This implies the electrical light-field, and therefore also the phase of the moving electrons, is constant across the entire nanoparticle. By that it is enough to derive an electrostatic solution where a time development can be added subsequently.

This assumption enables the application of the Laplace equation for electrostatics

$$\Delta\Phi = 0. \quad (4.13)$$

From a solution of this equation the electric field can be obtained by $\mathbf{E} = -\nabla\Phi$.

For easier treatment of the problem 4.13 the coordinates are chosen that the electric field has only a component in z -direction. This means the incoming field is written as $\mathbf{E}_0 = E_0\hat{\mathbf{z}}$.

The gold nanoparticle is assumed to be a homogeneous, isotropic sphere with diameter a and dielectric function ϵ_{sph} . It is placed at the origin of the coordinate system and surrounded by an isotropic medium with dielectric constant ϵ_{med} (figure 4.4). Due to the spherical symmetry of the problem, it is convenient to express the Laplace equation in spherical coordinates:

$$\frac{1}{r^2 \sin\theta} \left[\sin\theta \frac{\partial}{\partial r} \left(r^2 \frac{\partial}{\partial r} \right) + \frac{\partial}{\partial \theta} \left(\sin\theta \frac{\partial}{\partial \theta} \right) + \frac{1}{\sin\theta} \frac{\partial^2}{\partial \varphi^2} \right] \Phi(r, \theta, \varphi) = 0. \quad (4.14)$$

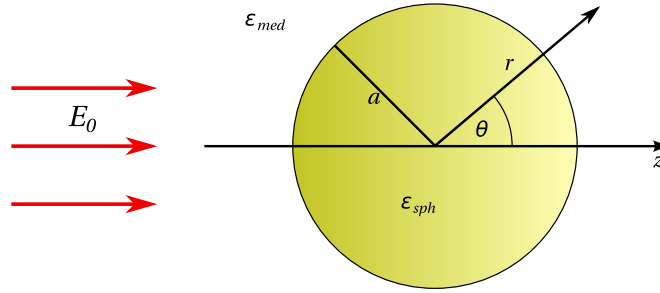


Figure 4.4: A gold particle with radius a placed in a homogeneous medium. It is radiated by a field pointing in z -direction.

Since the electric field points in z -direction, in spherical coordinates the problem is symmetric in φ and the last term $\frac{\partial^2}{\partial \varphi^2}$ is zero. This simplifies the problem and a general solution can be found in Jackson's book on classical electrodynamics [41]:

$$\Phi = \sum_{k=0}^{\infty} [A_k r^k + B_k r^{-(k+1)}] P_k(\cos \theta). \quad (4.15)$$

Here $P_k(\cos \theta)$ describes the Legendre Polynomial of order k .

Using the boundary conditions leads to a concrete solution Φ : As a first condition the potential has to be finite at the origin. Considering this and taking the symmetry of the problem into account, the solution can be divided in two parts, Φ_{in} for the inside of the sphere, Φ_{out} for the outside:

$$\Phi_{out} = \sum_{k=0}^{\infty} [A_k r^k + B_k r^{-(k+1)}] P_k(\cos \theta), \quad (4.16a)$$

$$\Phi_{in} = \sum_{k=0}^{\infty} C_k r^k P_k(\cos \theta). \quad (4.16b)$$

For the potential inside the sphere the constants for $r^{-(k+1)}$ were set to be zero. This is necessary since these factors would cause an infinite potential at the origin.

Another boundary condition is that for places very far away from the origin ($r \rightarrow \infty$) the influence of the sphere on the electric field should be negligible. This means that there the field needs to be parallel to the z -axis with its original amplitude. This leads to the condition

$$\Phi_{out} \xrightarrow{r \rightarrow \infty} -E_0 z = -E_0 r \cos \theta \quad (4.17)$$

which means

$$\sum_{k=0}^{\infty} A_k r^k P_k(\cos \theta) = -E_0 r \cos \theta. \quad (4.18)$$

The Legendre polynomials are orthogonal to each other. This means the term $\cos\theta$ has only one representation in Legendre polynomials. Since already $P_1(\cos\theta) = \cos\theta$, all components to other Legendre polynomials need to be zero. Also the proportionality to r can only be achieved if only A_1 is non-zero. Equation 4.18 then leads to $A_k = -E_0$ for $k = 1$.

Next, the electric potential needs to fulfil the boundary conditions at the surface. They are identical to those already presented when deriving the strength of a mirror dipole in section 2.3. They state that at the surface the tangential components of the electric field and the normal components of the displacement field have to be equal, which means:

$$\left. \frac{\partial\Phi_{in}}{\partial\theta} \right|_{r=a} = \left. \frac{\partial\Phi_{out}}{\partial\theta} \right|_{r=a} \quad \text{and} \quad \epsilon_{sph} \left. \frac{\partial\Phi_{in}}{\partial r} \right|_{r=a} = \epsilon_{med} \left. \frac{\partial\Phi_{out}}{\partial r} \right|_{r=a}. \quad (4.19)$$

Inserting the expressions for the potentials (equation 4.16) into these equations results in two series of Legendre polynomials equalling zero. These need to be zero for all θ , which means, due to the orthogonality of the Legendre polynomials, that all components need to vanish separately.

Jackson [41] shows that this is only fulfilled if $C_k = B_k = 0$ for $k \neq 1$ and that

$$C_1 = - \left(\frac{3\epsilon_{med}}{2\epsilon_{med} + \epsilon_{sph}} \right) E_0, \quad (4.20a)$$

$$B_1 = \left(\frac{\epsilon_{sph} - \epsilon_{med}}{\epsilon_{sph} + 2\epsilon_{med}} \right) \alpha^3 E_0. \quad (4.20b)$$

Inserting these results from the boundary conditions into the expressions for the potential in equation 4.16 results in

$$\Phi_{in} = - \frac{3\epsilon_{med}}{\epsilon_{sph} + 2\epsilon_{med}} E_0 r \cos\theta, \quad (4.21a)$$

$$\Phi_{out} = -E_0 r \cos\theta + \frac{\epsilon_{sph} - \epsilon_{med}}{\epsilon_{sph} + 2\epsilon_{med}} E_0 \alpha^3 \frac{\cos\theta}{r^2}. \quad (4.21b)$$

This means the potential outside of the sphere can be expressed by that of the incident field superposed with that of an electric point dipole placed in the origin with the electric dipole moment

$$\mathbf{p} = 4\pi\epsilon_0\epsilon_{med}\alpha^3 \frac{\epsilon_{sph} - \epsilon_{med}}{\epsilon_{sph} + 2\epsilon_{med}} \mathbf{E}_0. \quad (4.22)$$

The potential outside of the sphere then reads as

$$\Phi_{out} = -E_0 r \cos\theta + \frac{1}{4\pi\epsilon_0\epsilon_{med}} \frac{\mathbf{p} \cdot \mathbf{E}}{r^3}. \quad (4.23)$$

For this dipole a polarizability α can be defined via $\mathbf{p} = \epsilon_{med}\alpha\mathbf{E}_0$. It is expressed as

$$\alpha = 4\pi\epsilon_0 a^3 \frac{\epsilon_{sph} - \epsilon_m}{\epsilon_{sph} + 2\epsilon_m}. \quad (4.24)$$

This is of the same form as the Clausius-Mossotti relation (equation 2.13), which is not surprising since both relations describe the polarizability of a sphere.

The polarizability α is resonant when the denominator in equation 4.24 $|\epsilon_{sph} + 2\epsilon_{med}|$ is minimal. Assuming a real dielectric function for the medium and an arbitrary dielectric function for the sphere, the resonance occurs for a minimum in the denominator. For a small imaginary part $\text{Im}[\epsilon_{sph}]$ or a weak wavelength dependence of $\text{Im}[\epsilon_{sph}]$, this condition can be written as

$$\text{Re}[\epsilon_{sph}] = -2\epsilon_{med}. \quad (4.25)$$

This relation is called the Fröhlich condition [47]. For an oscillating field the associated modes for this resonance are the already introduced localised plasmons. That means they are the resonant oscillations of the electron plasma in the gold particles.

These localised plasmons are the reason the nanoparticle behaves like a dipole with polarizability α . The static field caused by the potential inside and outside of the sphere can be derived from $\mathbf{E} = -\nabla\Phi$:

$$\mathbf{E}_{in} = \frac{3\epsilon_{med}}{\epsilon_{sph} + 2\epsilon_{med}} \mathbf{E}_0, \quad (4.26a)$$

$$\mathbf{E}_{out} = \mathbf{E}_0 + \frac{1}{4\pi\epsilon_0\epsilon_{med}} \frac{3\mathbf{n}(\mathbf{n} \cdot \mathbf{p}) - \mathbf{p}}{r^3}. \quad (4.26b)$$

This shows that the field is enhanced both inside and outside of the sphere if localised plasmons are excited, that is in resonance. It is this field-enhancement at the plasmon resonance on which many of the prominent applications of metal nanoparticles in optical devices and sensors rely [47].

If the incident field is now no more static but oscillating, the system can still be treated as a point dipole in an external field. This holds at least as long as retardation effects can still be neglected [47].

The spectral characteristics of gold nanoparticles result from the reaction of the plasmonic dipoles to an incident light field. These dipoles both scatter and absorb the incident field, which is described by a plane wave. The scattering cross section σ_{scatt} is derived by dividing the total radiated power of the dipole by the energy density of the exciting wave [20].

The total radiated power of the dipole is obtained via the Poynting vector $\mathbf{S} = \mathbf{E} \times \mathbf{H}$ which is calculated with the electromagnetic fields of a point dipole [41]:

$$\mathbf{E} = \frac{1}{4\pi\epsilon_0\epsilon_{med}} \left[k^2(\mathbf{n} \times \mathbf{p}) \times \mathbf{n} \frac{e^{ikr}}{r} + [3\mathbf{n}(\mathbf{n} \cdot \mathbf{p}) - \mathbf{p}] \left(\frac{1}{r^3} - \frac{ik}{r^2} \right) e^{ikr} \right] \quad (4.27)$$

and

$$\mathbf{H} = \frac{ck^2}{4\pi} (\mathbf{n} \times \mathbf{p}) \frac{e^{ikr}}{r} \left(1 - \frac{1}{ikr} \right). \quad (4.28)$$

Integrating the Poynting vector over a closed spherical surface and averaging over time leads to the total radiated power P [20]:

$$P = \frac{1}{4\pi\epsilon_0\epsilon_{med}} \frac{ck^4}{3n} |\mathbf{p}|^2 = \frac{ck^4}{12\pi\epsilon_0 n} |\alpha|^2 |E_0|^2. \quad (4.29)$$

Here c denotes the vacuum speed of light and n the refractive index of the medium. k describes the wave vector in the medium.

The time averaged energy density of a plane wave is given by the energy density of an electric field multiplied with the light's propagation speed in the medium c/n :

$$S_{inc} = \frac{\epsilon_0 c}{2n} E_0^2. \quad (4.30)$$

Dividing now the radiated power by the incident energy density leads to an expression for the scattering cross section of a nanoparticle:

$$\sigma_{scatt} = \frac{k^4}{6\pi\epsilon_0^2} |\alpha|^2 = \frac{8\pi}{3} k^4 a^6 \left| \frac{\epsilon_{sph} - \epsilon_m}{\epsilon_{sph} + 2\epsilon_m} \right|^2. \quad (4.31)$$

This is the cross section that describes the scattering efficiency of a particle mediated by the plasmon resonance.

A point dipole does not only scatter light but also absorbs light if its polarizability also has an imaginary part. For plasmons this is the case, since the dielectric function of metals always also has a non-negligible imaginary component.

In analogy to the deviation of the scattering cross section the absorption cross section of a dipole is obtained by dividing the dissipated power by the incident energy density. From Poynting's theorem the energy dissipated in the dipole can be derived [20] and expressed as

$$P_{abs} = \frac{kc}{2n} \text{Im}[\mathbf{p} \cdot \mathbf{E}_0^*] \quad (4.32)$$

where \mathbf{E}_0^* denotes the complex conjugated amplitude of the electric field. Using $\mathbf{p} = \epsilon_{med} \alpha \mathbf{E}_0$ and the assumption that ϵ_{med} is real, one obtains

$$P_{abs} = \frac{kc}{2n} \epsilon_{med} E_0^2 \text{Im}[\alpha]. \quad (4.33)$$

This expression can now be divided by the energy density of the incident wave (equation 4.30) to find a value for the absorption cross section σ_{abs} of a nanoparticle:

$$\sigma_{abs} = \frac{k}{\epsilon_0} \text{Im}[\alpha] = 4\pi k a^3 \text{Im} \left[\frac{\epsilon_{sph} - \epsilon_m}{\epsilon_{sph} + 2\epsilon_m} \right]. \quad (4.34)$$

The two cross sections in equations 4.31 and 4.34 define the extinction spectrum of a gold nanoparticle in the region around the plasmonic resonance. The extinction cross section is given by the sum of absorption and scattering, that means

$$\sigma_{ext} = \sigma_{scatt} + \sigma_{abs}. \quad (4.35)$$

The extinction describes the general weakening of electromagnetic waves hitting the particle.

Since σ_{scatt} scales with a^6 it is dominant for bigger particles whereas σ_{abs} dominates the extinction for smaller particles since it scales with a^3 .

For gold the plasmon resonance is in the visible region of the electromagnetic spectrum. The absorption, extinction and scattering cross section of gold are shown graphically in figure 4.5(a). For this figure particles with a diameter of 100 nm were assumed to be placed in air (this means $\epsilon_{med} = 1$). The dielectric function for gold was again taken from Johnson and Christie [48] and inserted in the model for σ_{scatt} (equation 4.31) and the model for σ_{abs} (equation 4.34).

Both absorption and scattering show a maximum in the green area of visible light. The absorption maximum is located at $\lambda = 506$ nm whereas the scattering cross section shows a peak at $\lambda = 521$ nm. The shift in the peak can be understood from the fact that not only a minimum in the denominator determines the maximal value but also the properties of the numerator. It can shift resonances a bit in directions of its own maxima.

For these 100 nm-particles the scattering cross section is already bigger than the absorption cross section. However both phenomena contribute notably to the extinction.

The scattering cross section increases for smaller wavelengths. This is due to its k^4 dependence which dominates the decreasing of the resonance in α . The absorption does not decrease for wavelengths below 570 nm. This is caused by the interband transitions.

The resonance is very sensitive for changes in ϵ_{med} . This can be seen in figure 4.5(b), where the absorption cross section of the 100 nm-particles is plotted for different surrounding media or rather for different ϵ_{med} between 1 and 2.5. Also here the dielectric function of gold was obtained from Johnson and Christie [48].

The shift occurs since for different ϵ_{med} the denominator of α is minimal at different wavelengths. For $\epsilon_{med} = 1$ it occurs for $\epsilon_{sph} \approx -2$, for $\epsilon_{med} = 2.5$ $\epsilon_{sph} \approx 5$ is necessary. Due to

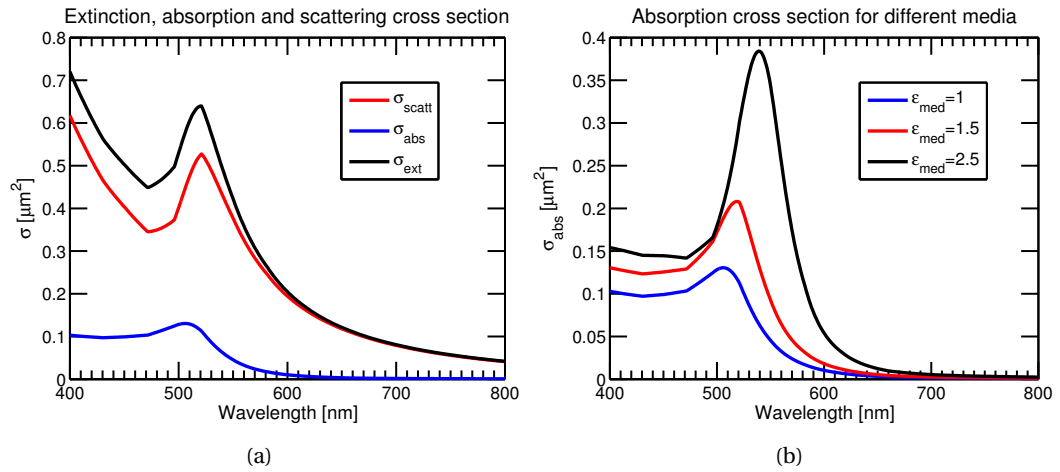


Figure 4.5: Model of the scattering cross section of gold nanoparticles with a diameter of 100 nm, the absorption cross section and their sum, the extinction cross section, of gold nanoparticles placed in a medium with $\epsilon_{med} = 1$ (a) for particles of this size, scattering is stronger than the process of absorption. Maximum scattering occurs for $\lambda = 521$ nm, the absorption maximum is located at $\lambda = 506$ nm. (b) shows the absorption cross section for different surrounding media. A higher ϵ_{med} causes the peak to shift to longer wavelengths. This shift results also in an increase of absorption at resonance due to a smaller imaginary part, in the dielectric constant of gold in this area.

the form of the real part of the dielectric function of gold (see 4.3(b)) the resonance shifts to higher wavelengths for media with higher ϵ_{med} . This makes gold nanoparticles a good sensor for changes in refractive index.

Qualitatively this effect can be understood from the medium's ability to compensate charges at the particle surface. This causes the surface charge to decrease and by that the restoring force on the plasma becomes smaller, leading to a smaller resonance frequency or a higher resonance wavelength, respectively.

The peak height in the absorption cross sections depends on the imaginary part of the dielectric function, because the real part of α vanishes when the Fröhlich condition is met. Therefore the peak for $\epsilon_{med} = 1.5$ is bigger than that for $\epsilon_{med} = 1$, since $\text{Im}[e_{sph}]$ is smaller at a resonance wavelength $\lambda = 519$ nm than at $\lambda = 506$ nm. This attenuation becomes even smaller for the peak with $\epsilon_{med} = 2.5$ at a resonance wavelength of $\lambda = 539$ nm.

For this previous discussion the assumption was made, that retardation effects can be neglected and that the electric field is constant over the whole particle. However this assumption is actually only valid for particles smaller than 20 nm [50]. For a more precise modelling, especially of the absorption cross section, Mie theory needs to be applied. This includes also moments of higher order like quadrupole and octupole moments in addition to the dipole moment. These cause a red shift in the absorption spectra of 10 nm-particles [50].

This section presented the reasons for the formation of localised plasmons as resonant oscillations of the electron gas. For gold nanoparticles these plasmons occur in the visible range of the electromagnetic spectrum and can thus influence the fluorescence of dyes emitting light in a comparable spectral region.

4.3 J-aggregates

J-aggregates are self-organised supramolecular clusters occurring for certain organic dyes at high concentrations. They were independently discovered by Jelley [31] and Scheibe [32] in the 1930s (J denotes Jelly). They have a sharp fluorescence peak and a comparably small Stokes shift. Thus they are useful as optical sensitisers [33], laser active media [30] or fluorescent tags [34]. Their optical properties result from the coupling of monomer excitations over the whole aggregate.

This section shall give an overview over the physical theory of those aggregates. They can be approximated as linear chains of monomers whose interaction is mediated by the transition dipole moments of their lowest excited state. Due to this interaction they form a new energy band. This energy band can be understood by a model of classical linear dipoles placed in a one-dimensional chain as will be done later in the section. With this understanding the energetic properties of J-aggregates become clear.

J-aggregates occur in solution or at solid-liquid surfaces [29]. They evolve due to intermolecular van-der-Waals-like attractive forces between the molecules (often referred to as monomers) [30] and as the monomers are no longer spatially separated but assembled regularly, interactions between them can arise. This results in supramolecular excited states.

The monomers are plain two dimensional molecules. In the easiest configuration which can well be used to describe the phenomenon they form chains similar to a brick pile. The single molecules are separated by a distance a . A sketch of this configuration is depicted in figure 4.6.

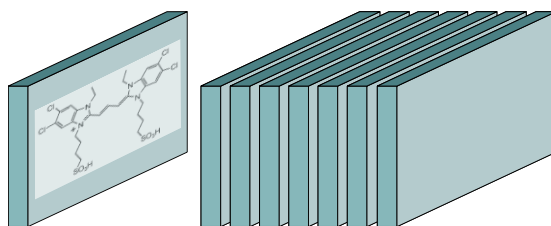


Figure 4.6: Two dimensional plates resembling monomers in a chain. As an example molecule TDBC is shown with its two-dimensional structure on the left.

The lowest excited state of this aggregate is described by an electron-hole pair where the distance between the two is on the order of a monomer size. Such an electron hole pair is called Frenkel exciton [51]. It is delocalised over the whole aggregate .

The wave function of the aggregate with N monomers in the ground state can be written as

$$\Psi_G = u_1 u_2 \dots u_{N-1} u_N \quad (4.36)$$

where u_j describes the ground state of the j th monomer. If the j th monomer is excited and intermolecular interactions can be neglected, the state is written as

$$\phi_j = u_1 \dots u_{j-1} u_j^* u_{j+1} \dots u_N \quad (4.37)$$

where u_j^* describes the lowest excited state of the j th monomer. This non-interaction state has the energy $\epsilon_j = \epsilon$.

Allowing interaction between nearest neighbours the Schrödinger equation is written as [51]

$$H\phi_j = \epsilon\phi_j + V(\phi_{j-1} + \phi_{j+1}). \quad (4.38)$$

Here V is the intermolecular interaction energy and represents the energy transfer from the molecule j to its neighbours $j \pm 1$. For J-aggregates this interaction is given by the interaction of the transition dipole moments of the monomers [30].

The ϕ_j are no more eigenfunctions for this Hamilton operator. Those can be found via diagonalisation of H . The new set of eigenfunctions can be expressed by linear combination of the ϕ_j via [51]

$$\Psi_K = \sum_j e^{ijKa} \phi_j. \quad (4.39)$$

K is the wave vector of the state and $\hbar K$ plays the role of the exciton's quasi momentum. Inserting this wave function into the Schrödinger equation 4.38 yields

$$H\Psi_K = e^{ijKa} [\epsilon + V(e^{-ijKa} + e^{ijKa})] \phi_j = (\epsilon + 2V \cos(Ka)) \Psi_K = E(K) \Psi_K. \quad (4.40)$$

Thus the energy of an excited state is given by $E = \epsilon + 2V \cos(Ka)$. To understand this energy, let us look at a one dimensional chain of classical point dipoles which have the constant distance a between two nearest neighbours. For a classical dipole its electric near field is given by equation 2.14:

$$\mathbf{E} = \frac{1}{4\pi\epsilon_0} [3\mathbf{n}(\mathbf{n} \cdot \mathbf{p}) - \mathbf{p}] \frac{1}{r^3}. \quad (4.41)$$

Two cases can occur: An orientation of the dipoles perpendicular to the chain axis (the transversal case) and an orientation parallel to the chain axis (the longitudinal case). Both cases can be treated simultaneously. The electric field of a dipole at the position of its closest neighbour is written as

$$E_{i,m} = \frac{\gamma_i p_{i,m}}{4\pi\epsilon_0 a^3}. \quad (4.42)$$

Here γ_i is a polarisation dependent constant, where the index i refers to the polarisation. It is $\gamma_T = -1$ in the transversal case and $\gamma_L = 2$ in the longitudinal case. Thus the interaction energy between two dipoles depending on their orientation can be written as

$$V_i = \gamma_i c \quad (4.43)$$

where c is a polarisation independent constant. Inserting this into equation 4.40 leads to a dispersion relation for a chain of any kind of dipoles

$$E = E_0 + 2V \cos(Ka). \quad (4.44)$$

Here E_0 describes the energy of an independent dipole. This dispersion relation is plotted in figure 4.7.

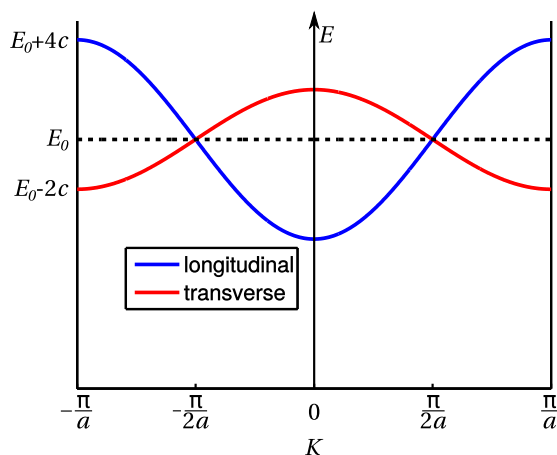


Figure 4.7: Dispersion of a chain of dipoles. The $k = 0$ mode increases the energy for transversal orientation and decreases the energy for longitudinal orientation.

This means the energy of the chain of dipoles compared to independent dipoles shifts (depending on the k -vector and the polarisation). $K = 0$ means all dipoles are parallel, while $K = \pi/a$ describes the case where neighbouring dipoles have opposite orientation.

The energy for transversal polarisation is increased for $K = 0$. This is due to the repulsive coulomb forces for parallel dipoles. For $K = \pi/a$ the energy is decreased in the transversal case. For longitudinal dipole orientation the situation is vice versa. The energy is decreased for only parallel dipoles and increased when direct neighbours are oriented antiparallel. A graphical motivation for the different energy shifts depending on the polarisation is shown in figure 4.8.

J-aggregates can indeed be described by such a dipole chain [51]. The transition dipoles are oriented parallel to the chain axis. Hence the lowest excitation forms a band of states with a dispersion relation described by the blue (longitudinal) line in figure 4.7. For $K = 0$ their energy is smaller than that of independent monomers and within the band this state is stable, that means it cannot decay along the band. If irradiated with light, due to momentum conservation and the comparably small k -vectors of visible light, only states around $K = 0$ can be excited.

There are also aggregates of monomers with transition dipoles transversal to the chain axis. Those are called hypsochromic or H-aggregates. Their dispersion is given by the red line in

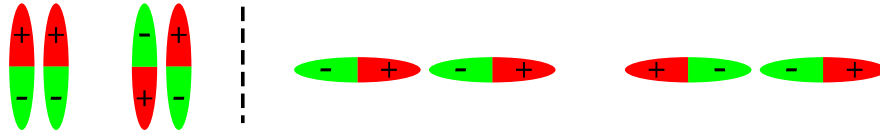


Figure 4.8: In the transversal case (left) parallel dipole moments cause a higher energy, whereas it is decreased for antiparallel dipole moments. In the longitudinal case (right) it is the other way around: Parallel dipoles decrease the energy whereas antiparallel dipole increase it.

figure 4.7. Since also they can only be excited around $K = 0$, their fluorescence is not that strong, since excited states can decay along the band.

In reality the spatial structures of J-aggregates are more complicated than a simple one-dimensional linear chain [29]. However their principal characteristics can still be understood by the simple model presented in this section.

In summary this means that, compared to their monomers, J-aggregates have a lower excitation energy caused by the interaction of longitudinal transition dipole moments. Due to the band structure this excitation (a delocalised exciton) is stable and strongly fluorescing.

4.4 Strong coupling

The interactions between quantum mechanical systems are commonly classified in weak coupling and strong coupling regimes. Weak coupling means, that the single systems are coupled stronger to other systems. This means for example that for at least one of the systems damping dominates its properties. Examples for weak coupling are changes in the decay rate of excited atoms (Purcell effect [52]) or Förster resonance energy transfer (FRET) [53] which describes the energy transfer from a donor to an acceptor where the decay rate of the acceptor is higher than the energy transfer rate.

Strong coupling occurs when the coupling between two systems is dominant. This means for example if the decay rate of the energy acceptor in FRET is no more higher than the energy transfer rate. In that case energy can be transferred back to the donor and the excitation becomes delocalised. In such a situation the two systems can no more be treated as single systems but must be seen as one.

The experiments presented in chapter 5 were conducted to investigate the characteristics of gold nanoparticles coated with a fluorescent dye that develops J-aggregates. It has been shown that the plasmons and excitons in the respective particles can be strongly coupled [35]. Therefore this section discusses the most important properties of strong coupling, especially the energy splitting it causes if the uncoupled energies have similar values.

The effect of strong coupling can most easily be understood by looking at two coupled classical oscillators as shown in figure 4.9. Two masses m_A and m_B shall be coupled to solid ground by two springs with the coupling constants k_A and k_B . In addition they shall be connected by a spring with coupling constant κ .

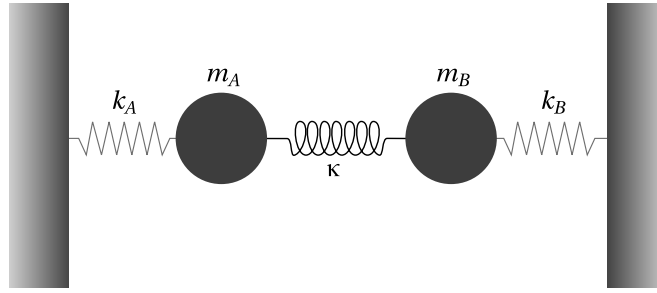


Figure 4.9: The coupled oscillator model: Two mechanical oscillators with masses m_A and m_B and spring constants k_A and k_B are connected via a spring with spring constant κ .

If the masses were uncoupled, their eigenfrequencies would be $\omega_{0,A} = \sqrt{k_A/m_A}$ and $\omega_{0,B} = \sqrt{k_B/m_B}$. For the coupled regime the equations of motion are given by

$$m_A \ddot{x} + k_A x_A + \kappa(x_A - x_B) = 0, \quad (4.45a)$$

$$m_B \ddot{x} + k_B x_B - \kappa(x_A - x_B) = 0. \quad (4.45b)$$

Here x_A and x_B denote the positions of the masses. This system can be solved with the ansatz $x_i = x_{0,i} e^{i\omega_{\pm} t}$ where ω_{\pm} describes the new eigenfrequencies of the system. The solutions for ω_{\pm} are given by [54]

$$\omega_{\pm}^2 = \frac{1}{2} \left[\omega_A^2 + \omega_B^2 \pm \sqrt{(\omega_A^2 - \omega_B^2)^2 + 4\Gamma^2 \omega_A \omega_B} \right] \quad (4.46)$$

where $\omega_A = \sqrt{(k_A + \kappa)/m_A}$, $\omega_B = \sqrt{(k_B + \kappa)/m_B}$ and

$$\Gamma = \frac{\sqrt{\kappa/m_A} \sqrt{\kappa/m_B}}{\sqrt{\omega_A \omega_B}}. \quad (4.47)$$

The two new eigenfrequencies can be seen as follows: The lower value ω_- represents an oscillation where both oscillators are in phase, whereas ω_+ describes the eigenfrequency when both oscillators are out of phase.

The consequences of the coupling for the eigenfrequencies are shown in figure 4.10. For this figure a constant $\omega_A = \omega_0$ was defined and the two eigenfrequencies are plotted against a difference frequency $\Delta\omega = \omega_A - \omega_B$. The left plot shows the situation without coupling. As $\Delta\omega$ is increased the two lines intersect at $\omega_A = \omega_B$. Assuming a coupling constant $\kappa \neq 0$, the two lines do not intersect anymore. Instead a characteristic *anticrossing* arises with a frequency splitting of $\Gamma = \omega_+ - \omega_-$ [54]. For large frequency differences the coupled eigenfrequencies approach the uncoupled ones, for small $\Delta\omega$ the splitting becomes stronger.

Note that until now, damping of the oscillators was neglected. If also taken into account, this damping would cause complex eigenfrequencies. Their imaginary part would represent

the linewidth and thus cause a smearing out of the curves in figure 4.10 [54]. For quantum mechanical systems analogous arguments apply.

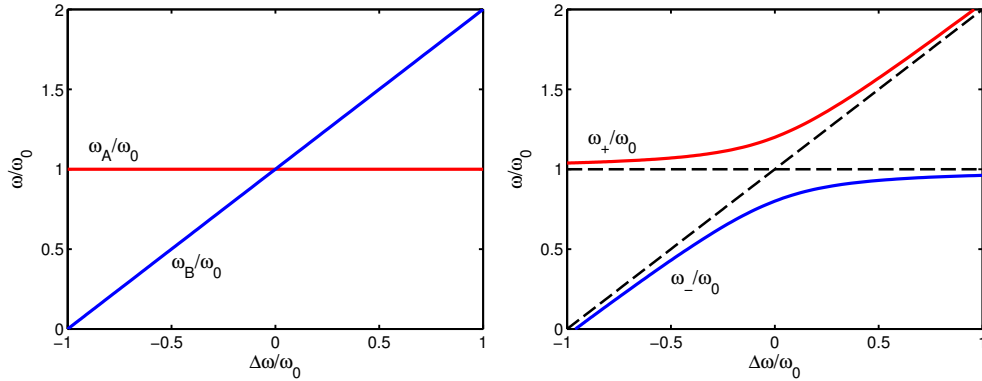


Figure 4.10: Properties of the resonance frequency without (a) and with (b) coupling. Without coupling the lines intersect when the resonance frequency is identical. This intersection does not occur for coupled oscillators. Instead, a characteristic anticrossing arises.

It has been shown that the excitons in J-aggregates and the plasmons in gold nanoparticles can couple strongly [35]. For this the particles need to be coated with the dye. If strong coupling occurs the plasmons and excitons are no more independent but form new states that are called *plasmon-exciton* or *plexiton*. Their eigenfrequencies are in principle given by those of the coupled oscillator derived earlier and thus shifted compared to those of uncoupled plasmons and excitons [55]. Fofang et al. show that plexitons can indeed be understood in the classical picture, too [35]. This justifies the argumentation with classical dipoles.

The strong coupling can then be seen by two peaks in the absorption spectrum which are shifted with respect to the original peaks. The peak with originally higher energy is blue-shifted whereas the lower energy peak gets shifted to the red part of the absorption spectrum. This increased peak splitting is the characteristic fingerprint of strong coupling [54].

Summary: This chapter presented the theoretical foundation of the experiments presented and discussed in the following chapter. The properties of localised plasmons in gold nanoparticles were discussed as well as the properties of J-aggregates in certain organic supramolecules. To have a better understanding of the plasmons, the dielectric function of gold was discussed.

As once more will be shown in the next chapter excitons and plasmons are strongly coupled in gold nanoparticles that are coated with the fluorescent dye TDBC. Therefore properties and consequences of strong coupling were presented in the last section of this chapter. These theoretical elaborations are the basis for the discussions of the experiments presented in the next chapter.

5 Experiments

This chapter presents the results of the single particle fluorescence spectroscopy measurements for a gold nanoparticle coated with 5,5',6,6'-tetrachloro-1-1'-diethyl-3,3'-di(4-sulfo-butyl)-benzimidazolocarbo-cyanine (TDBC). These measurements were conducted with the scattering SNOM introduced in chapter 3. The results show that the fluorescence of the J-aggregates formed by TDBC molecules is annihilated in gold nanoparticle-TDBC compounds.

In order to understand the systems under investigation, the preparation of the samples will first be explained in section 5.1. Afterwards the components will be studied independently. This is, the absorption of gold nanoparticles as well as the transmission and fluorescence of aqueous TDBC solutions will be discussed in section 5.2. There the occurrence of a plasmon resonance peak in the gold particles and the forming of J-aggregates in the TDBC solutions can be observed.

After those preliminary experiments spectra of the TDBC coated gold nanoparticles will be presented in section 5.3. The section will start with the absorption spectrum showing that strong coupling occurs in those compounds. Afterwards the single particle spectra will be discussed. The chapter will end with a comparison between single and many particle spectra showing that peaks in a single particle spectrum are sharper since they are not inhomogeneously broadened.

5.1 Preparation of samples

Eventually the spectroscopy by the SNOM took place on a substrate. Section 4.2 discussed the dependence of the resonance frequency on the surrounding medium. Therefore the spectra were taken for gold particles deposited on a substrate as opposed to measurements in solution. Both silicon and fused silica substrates were used.

The surface charge of the gold particles is slightly negative. To adsorb the particles on the substrate, the latter should have a positive surface charge. This can be achieved by coating the surface with layers of ionic polymers (polyelectrolytes) with a cationic polyelectrolyte as topmost layer.

These polyelectrolytes are polymers composed of monomers with an electrolyte group that dissolves when in contact with deionized water. One part of the electrolyte group stays bonded to the monomer which results in a charged polymer molecule.

For this work the polymers poly-ethyleneimine (PEI), poly-sodium 4-styrenesulfonate (PSS) and poly-allylamine hydrochloride (PAH) were used. Both PEI and PAH are cationic whereas PSS is anionic. Figure 5.1 shows the chemical formulas and the functional groups of the molecules.

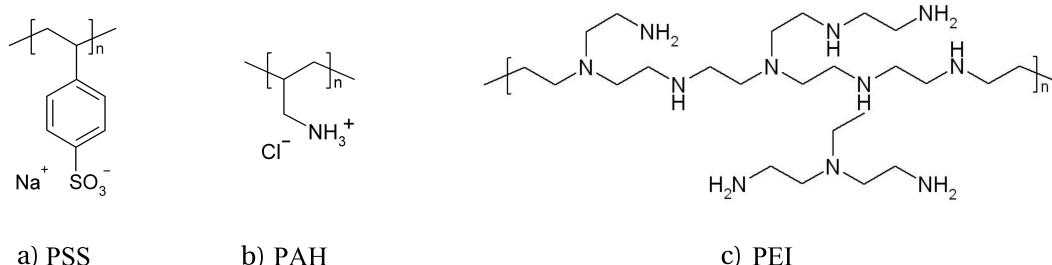


Figure 5.1: Chemical structures of the used polymers: PSS (a), PAH (b) and PEI (c) (from Kiel [56]). In PEI, all nitrogen atoms can accept a further hydrogen ion when in aqueous solution and thus cause the cationic behaviour [57].

PEI is a branched cationic polyelectrolyte with a monomer molecular weight of 163.266 g/mol. It was delivered as a 50 wt% aqueous solution. PAH is a linear cationic polyelectrolyte with a monomer molecular weight of 93.56 g/mol and was, like PSS, purchased as solid. PAH is a weakly charged polyelectrolyte. PSS is linear and anionic. Its monomer weight measures 206.20 g/mol. All polyelectrolytes were purchased from Sigma-Aldrich.

The method of depositing polyelectrolytes on a substrate uses the maximisation of entropy as driving force to develop thin films of ionic polymers [56]. For this, the polyelectrolytes are dissolved in aqueous NaCl solution. The Na⁺ or Cl⁻ ions are then located in proximity of the polymer chains and act as counterions.

If now in touch with a layer of differently charged polyelectrolyte the charged segments compete with the compensating ions of the layer. A release of the ions into the water and bonding between differently charged polymer segments causes the polymers to be fixed in one position whereas the released ions can move freely. The fixation of one polymer molecule causes the release of a lot of ions. Thus the process of bonding between the monomers of differently charged polyelectrolytes increases the degrees of freedom in the system. This results in an increase of entropy in the system which causes the polymer-polymer bonding to be favoured. The process is shown in figure 5.2.

Immersing the layer in deionized water washes away the excess Na and Cl ions and the final state is a stable bond of the two layers of differently charged polyelectrolytes. Only in the layer closest to air some Na⁺ or Cl⁻ ions remain in the compound [56] and a new layer can be adsorbed.

A spin coater is used to evenly spread solutions over a substrate. The substrate is fixed in the centre of a rotatable table inside a closed chamber filled with nitrogen. It is kept stable by creating a vacuum underneath. The substrate is rotated with 3000 rpm while desired liquids are deposited onto it. For this deposition the chamber's lid has holes for syringes. The solutions had a polymer concentration of 10⁻³ mol/l and a NaCl concentration of 0.5 mol/l.

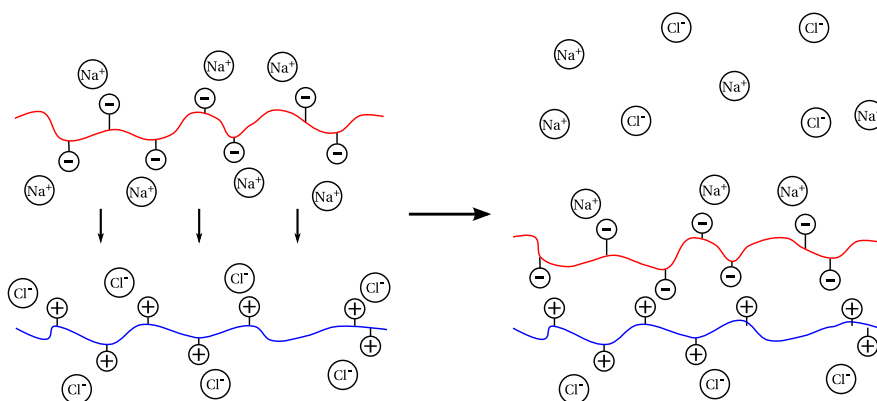


Figure 5.2: A layer of anionic polyelectrolyte comes in vicinity of a cationic polyelectrolyte. Due to the increasing entropy the small counter ions dissolve in the solution while the two polymers become bonded.

The process was the same for all polymers. A layer was created by depositing a few drops (between 5 and 10) of polymer solution on the spinning substrate. Due to the centrifugal force the solution was spread evenly on the whole substrate and a layer could evolve. After 5-10 seconds the excess of the solution was washed away by depositing 5 - 10 drops of water on the substrate. Since it was constantly rotating, after a few seconds all liquid on the substrate had vanished and a new layer could be created.

The substrates have a homogeneously negatively charged hydrophilic surface [56] to which PEI adsorbs very strongly. It was therefore used to form the ground layer on the substrate. In addition it can compensate small inhomogeneities in the surface charge distribution of the substrate, which otherwise could cause defects in the multilayer structure [56].

Afterwards, alternating layers of PSS and PAH could be adsorbed. For the main experiment reported in section 5.3 only one such double layer (that means one layer PSS and on layer PAH) was used.

After a substrate was prepared with polyelectrolyte layers with PAH as the highest layer, the gold nanoparticles were deposited on top. The particles were purchased in from Sigma Aldrich. They had a diameter of 100 nm and were stabilised in a suspension with citrate buffer.

Around 0.5 ml of the suspension were poured on the sample. The gold particles were given 2 hours to adsorb before the rest of the suspension was washed away with purified water. Eventually a sample with evenly spread gold nanoparticles was obtained.

A sketch of such a sample is shown in figure 5.3(a). To show that this sample fabrication process yields gold nanoparticles deposited in the desired way, figure 5.3(b) presents a picture of such a sample taken in a raster electron microscope.

To investigate strong coupling between plasmons and excitons, the gold nanoparticles were coated with TDBC. This is a fluorescent dye that, at a certain minimum concentration, forms J-aggregates as presented in section 4.3. The chemical structure can be seen in figure 5.4. It was purchased as powder from FEW Chemicals.

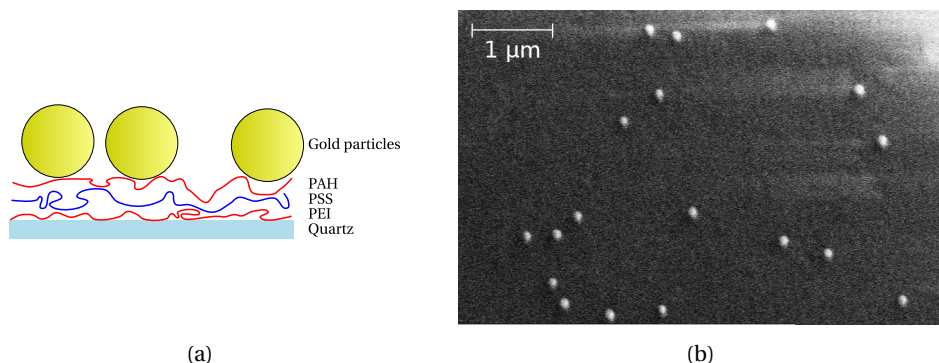


Figure 5.3: (a) shows a sketch of a gold nanoparticle sample on a coated substrate. The particles are deposited on quartz that was coated layer by layer with PEI, PSS and PAH. (b) shows an image of such a sample taken in a raster electron microscope. The particles are nicely spread and do not cluster.

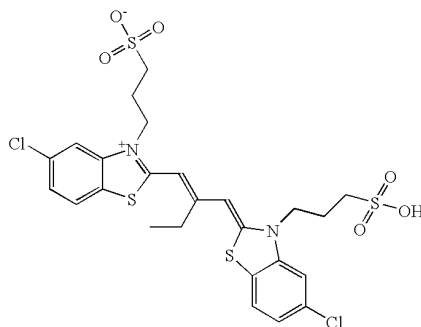


Figure 5.4: Chemical structure of TDBC. The adsorption on gold is mediated by the nitrogen atoms (from Bower et al. [58]).

The coating process follows the protocol described by Lekeufack et al. [59]. The TDBC was prepared in an aqueous solution with a concentration of $c = 5 \cdot 10^{-5}$ mol/l and small amount of NaOH to adjust the pH value above 7. The mixture was stirred for 5 minutes and afterwards placed in an ultrasonic bath for 15 minutes. This solution could directly be used for coating of gold nanoparticles. For this, the solution was mixed with the gold particle suspension at a ratio of 1 : 1. This mixture was kept away from light and stored for 24 hours. In that time the citrate ions which stabilized the particle surface were gradually replaced by TDBC. The adsorption of the TDBC was mediated by the nitrogen atoms [59].

After the 24 hours, the now coated particles were separated from the excess by centrifugation at a speed of 8000 rpm for 10 minutes. Afterwards the excess was removed.

These TDBC coated gold particles appeared to stick best on a positively surface charged substrate, too. Hence the process of sample preparation was identical to that of uncoated particles presented earlier.

This section showed how gold nanoparticles were coated with TDBC and how both coated and uncoated particles were prepared on substrates (fused silica or silicon).

5.2 Spectra of uncoupled gold nanoparticles and TDBC

In order to understand the characteristics of gold nanoparticle-TDBC compounds, they were first investigated independently. An absorption spectrum of gold particles was recorded and will be presented in section 5.2.1. The spectrum will show that plasmon resonance occurs in the visible region. Section 5.2.2 presents and discusses transmission and fluorescence spectra of TDBC in aqueous solutions with different concentrations. There the occurrence of J-aggregates can be observed for sufficiently high concentrations.

5.2.1 Absorption of gold nanoparticles

Now, the absorption spectrum of gold nanoparticles will be discussed. This is done to experimentally show the actual occurrence of a plasmon resonance and as preparation for understanding the spectra of the TDBC coated gold nanoparticles.

The absorption spectra were measured by a spectrometer employing an Indium gallium arsenide (InGaAs) integrating sphere also called Ulbricht sphere. This is a sphere with highly non-absorbing inside walls and a InGaAs photodiode on its top. Due to the very low absorption of the walls every photon that reaches the walls is again and again scattered back inside the sphere until it is eventually recorded by the diode. Ideally every photon that hits the sphere's wall is detected. In practise of course not every photon is detected and a measurement has to be normalised with a reference baseline.

With such a sphere transmitted, reflected and scattered photons of a sample can be detected. From that the sample's absorption can be calculated. A sketch of the system is shown in figure 5.5.

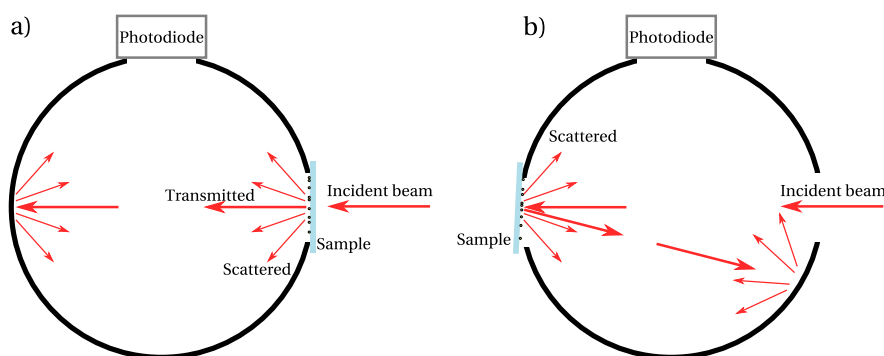


Figure 5.5: Sketch of an Ulbricht sphere for absorption measurements. Light hitting the non-absorbing walls will eventually be recorded by the detector. First wavelength dependent transmittance and forward scattering are measured (a), afterwards reflectance and back scattering are recorded (b).

Transmission and forward scattering are obtained in one measurement, reflectance and back scattering in a second. For transmission and forward scattering the sample is placed in the beam path of the incident light in an aperture directly in front of the sphere (figure

5.5(a). All light passing this aperture is detected by the sphere. The recorded spectrum is then divided by a baseline taken without a sample, which resembles a 100% transmission sample.

In a second measurement the sample is placed on the backside of the sphere and illuminated through the aperture already used for transition. The sample is slightly tilted, to prevent directly reflected light from exiting the sphere undetected (figure 5.5(b)). Again the result is divided by a baseline taken with a closed aperture in the back. This is identical to having a 100% reflectance sample.

The absorption is now obtained by subtracting the values of transmission and forward scattering ($T_{d,s}$) and those of reflection and back scattering ($R_{d,s}$) from 100%, i.e. $Abs = 100 - T_{d,s} - R_{d,s}$.

For uncoated gold nanoparticles an absorption spectrum was taken of the sample shown in figure 5.3(b) where a picture of an exemplary sample is presented. The measurement was executed with a Cary 5000 spectrophotometer by Varian. The results are shown in figure 5.6.

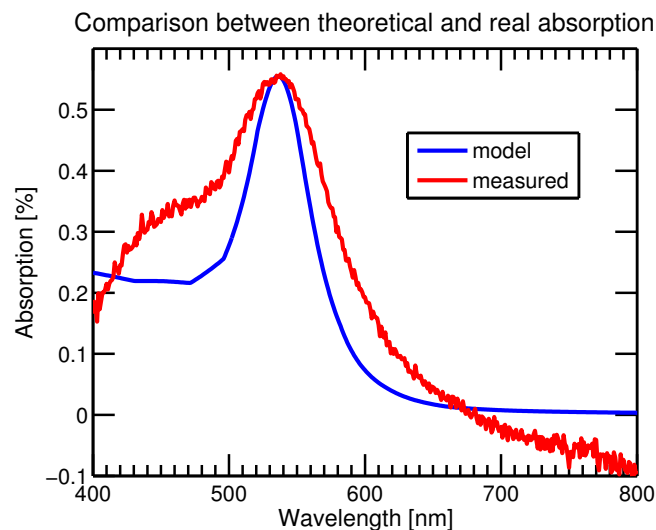


Figure 5.6: Absorption spectrum of gold nanoparticles on a glass substrate. The plasmon peak can be seen nicely with a maximum at 537 nm.

The spectrum looks partly as expected from theory. The absorption shows a peak around 537 nm. This is the absorption caused by surface plasmons excited in the particles. For higher wavelengths this absorption vanishes, for lower wavelengths than the resonance the absorption remains above zero. Obviously the experimental data does not completely reflect the real absorption spectrum of the sample. It drops below the non-physical value of zero. This happened in several measurements on different days, which points to a bad calibration of the measuring instrument. This might also have caused the drop for smaller wavelengths below 560 nm. If the substrate, which could not be included on the baseline, had an influence on the absorption of small wavelengths, it would have increased the absorption and not caused a drop. Therefore this possibility can be ruled out.

Interestingly, the absorption spectrum of TDBC coated gold nanoparticles which is presented later (figure 5.8) does not show these abnormalities. But all measurements executed both before and after the TDBC-gold absorption with different sample showed the same results like that shown in figure 5.6.

Since the samples were prepared identically the only difference between these two measurements was that in one case the gold surface was covered with stabilising citrate buffer whereas in the other the gold was coated with TDBC. Thus the differences can also only be caused by the coatings. However, even if the citrate buffer had such a big influence on the gold, this does not explain the non-physical negative absorption values. Another explanation might be that the absorption of the sample without TDBC is very weak (the sample with TDBC absorbs around 16 times more light at the peak, this might be caused by better adsorption on the sample). Hence the spectrometer might work inaccurate for too low absorptions.

If the latter reason is right, the spectral regions with higher absorptions can be treated as approximately correct. Thus the absorption maximum is assumed to be indeed around 537 nm and a comparison with the theoretical model is discussed.

To fit the model presented in the previous chapter to the measurement results, a surrounding medium with a dielectric constant of $\epsilon_{med} = 2.4$ had to be assumed for the actual sample. The particles were not only surrounded by one medium but by quartz, a thin layer of polyelectrolytes and air. In general it is possible to assume an effective dielectric constant by averaging over the included media, depending on their contribution to the surrounding volume [50]. However with air that approximately has a dielectric constant of $\epsilon_{air} = 1$, quartz that approximately has a dielectric function of $\epsilon_{quartz} = 2.1$ [60] and the polyelectrolytes with $\epsilon_{poly} = 2.5$ [61], a dielectric constant of $\epsilon_{med} = 2.4$ is only achievable if the small polyelectrolyte layer is overestimated.

This shows that the dipole quasi static model presented in section 4.2 does not completely explain the spectrum of gold nanoparticles with a diameter of 100 nm. As mentioned also quadrupole and octupole modes caused by retardation effects lead to a red-shift of the absorption maximum and need to be considered in the model to obtain a good approximation of reality.

Since the contribution of those higher moments depends on the size of a particle a variation in particle size also causes a widening of the resonance peak due to the inhomogeneity. The manufacturer gives 12% as the maximal variation in size for the particles. This explains the peak widening in the measurement compared to the model.

Another effect might contribute to the peak width: The resonance is very sensitive to the electric constant of the surroundings. Therefore the slightest variation in the surroundings of different particles causes a shift of the resonance wavelength. Hence chemical inhomogeneities of the coated substrate lead to a widening of the absorption peak as well.

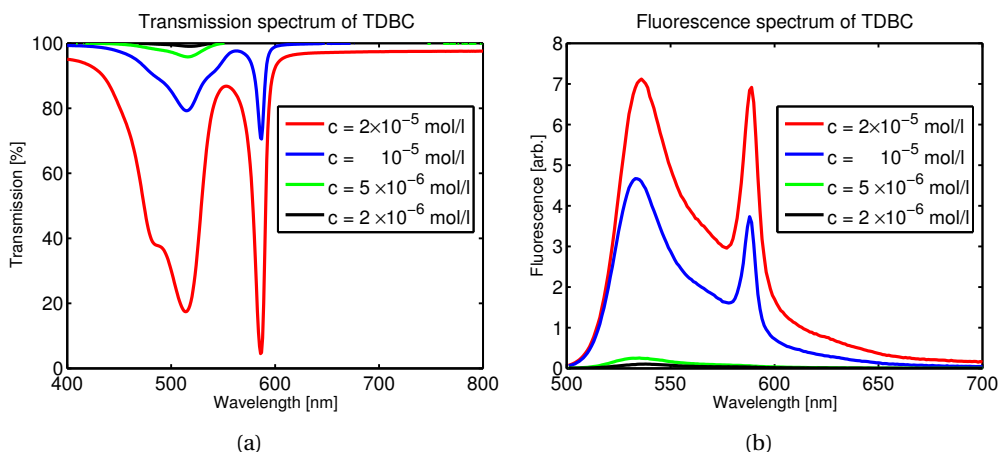


Figure 5.7: Transmission (a) and fluorescence (b) spectrum of TDBC for concentrations of $c = 2 \cdot 10^{-5}$ mol/l, $c = 10^{-5}$ mol/l, $c = 5 \cdot 10^{-6}$ mol/l and $c = 2 \cdot 10^{-6}$ mol/l, respectively. The monomer absorption or fluorescence can be seen in all curves, the two higher concentrations show a dip in the transmission spectrum and peak in the fluorescence. These are caused by J-aggregates that form for sufficiently high concentrations.

5.2.2 Formation of J-aggregates of TDBC

This section shows both absorption and fluorescence spectra of TDBC solutions of different concentrations. With increasing concentration new peaks caused by the J-aggregates occur. Figure 5.7 depicts transmission and fluorescence spectra of TDBC solutions. The had a concentration of $c = 2 \cdot 10^{-5}$ mol/l, $c = 10^{-5}$ mol/l, $c = 5 \cdot 10^{-6}$ mol/l and $c = 2 \cdot 10^{-6}$ mol/l, respectively.

The transmission was measured with the Cary 5000 spectrophotometer that was also used in absorption measurements. For the fluorescence spectra a *Fluorolog* from Horiba was used. There the solutions were excited with light of 488 nm emitted from a Xenon arc lamp. This wavelength was chosen since it is also the wavelength of the laser used for the single particle spectrum that is presented later in this chapter.

All transmission spectra show a dip at 515 nm but with different depth. This becomes stronger for higher concentration. A dip in the transmission spectrum is caused by a peak in the absorption. In this case the dip is caused by the monomer absorption of the fluorescent dyes. The dips show side lobes for all concentrations which are caused by other vibronic transitions in the monomers [32]. In addition, for the two higher concentrations a new transmission dip appears at $\lambda = 587$ nm. It is relatively sharp compared to the monomer dips. It does not appear for lower concentration and shows the formation of J-aggregates for a TDBC concentration above $c = 10^{-5}$ mol/l. As expected the J-aggregate absorption is red-shifted compared to that of the monomers. The reason for this was discussed in section 4.3: The parallel transition dipoles oriented along the chain axis cause an decrease of energy.

The fluorescence spectra show a peak around $\lambda = 535$ nm. This is the corresponding fluorescence to the monomer absorption peak. It can be seen for all concentrations only with different intensity. For the two higher concentrations the fluorescence peak of the J-aggregates is visible at $\lambda = 589$ nm.

Now the relevant properties of the independent components of the gold nanoparticle-TDBC compounds are clear: Localised plasmons occur in gold nanoparticles in the region of visible light and for sufficiently high concentrations J-aggregates appear in aqueous TDBC solutions. Their excitations, the excitons, show a sharp absorption and fluorescence around 588 nm.

5.3 Spectra of TDBC coated nanoparticles

This section presents the measurements conducted for gold nanoparticles coated with TDBC as presented in section 5.1. To see that the gold indeed was coated with TDBC and that strong coupling occurs, section 5.3.1 will present an absorption spectrum of the compound. Section 5.3.2 eventually shows the single particle fluorescence spectrum of one coated gold particle recorded with the SNOM. This spectrum will show that the J-aggregate fluorescence is almost completely annihilated and possible reasons will be discussed.

5.3.1 Absorption

To show that the gold nanoparticles were really coated with TDBC and that strong coupling occurred, an absorption spectrum was taken. For this the particles were adsorbed on a coated fused silica substrate as explained in section 5.1. The absorption was again measured using the Ulbricht sphere and the result is presented in figure 5.8.

The absorption spectrum shows two peaks at $\lambda = 527$ nm and $\lambda = 595$ nm. In between them there is a dip at $\lambda = 583$ nm. This spectrum shows that the plasmons of the gold particles and the excitons of the J-aggregates indeed are strongly coupled.

The peaks are shifted compared to those of the uncoupled measurements. If the plasmons and excitons were not coupled the spectrum would look like the sum of the independent spectra [35] (if the concentration of the components is the same as in the uncoupled measurements). In that case, the peaks would at most move closer to each other. However here, the splitting between the two peaks becomes larger. The low-energy peak is red-shifted (from 587 nm to 595 nm) whereas the high-energy peak is blue shifted (from 537 nm to 527 nm). These features show the anticrossing discussed in section 4.4, a characteristic fingerprint of strong coupling [54]. This leads to the conclusion that here the plasmons and excitons indeed couple strongly and form plexcitons.

The presented results coincide with those from other publications like that by Fofang et al. [35] or that by Lekeufack et al. [59]. Also these authors see these outcomes as proof for the occurrence of strong coupling. The results also show that the gold particles indeed were coated with TDBC since otherwise strong coupling would not occur.

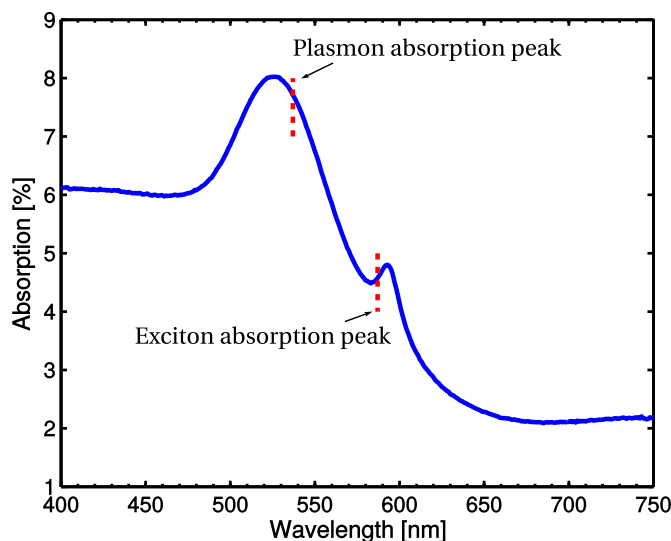


Figure 5.8: Absorption spectrum of TDBC coated gold nanoparticles. Two peaks are visible whose maxima are shifted compared to those of uncoupled components. For comparison the positions of the uncoupled peak maxima are marked in the spectrum. The shift shows that plasmons and excitons are strongly coupled.

5.3.2 Emission

To investigate the influence of the gold nanoparticles on the fluorescence of J-aggregated TDBC, a single particle fluorescence spectrum of a coated gold particle was recorded. For this a SNOM picture was taken of a sample where TDBC gold particles were deposited. From that picture a single particle was chosen and both tip and laser focus brought to its center. A spectrum of the outgoing light was then taken.

For the SNOM measurement the particles were deposited on a silicon substrate since a strongly reflective surface eases the readjustment and optimisation of the near field signal. The substrate was prepared as explained in section 5.1. Of that sample a SNOM picture was taken of a random region with an area of ca. $25\mu\text{m}^2$. It is depicted in figure 5.9. The laser used for the picture and the spectra later was an Argon laser which produced an excitation wavelength of 488 nm.

The picture shows the gold particles on the substrate. Around those particles black edges appear. These edges are caused by the mechanism explained in section 2.6 and that is visualized in figure 2.6: The edges at the gold particles are too steep for the tip to immediately follow the topography. Therefore the distance between tip apex and sample increases around those edges, which causes a drop in the near field signal. This also causes the increased width of the particles in the picture. Their actual size is rather given by the non-black area within the edges.

Another idea is that the edges might arise from an interaction between the tip and the TDBC coating. However this hypothesis could be abandoned since uncoated gold particles on a Si-substrate showed the same black edges.

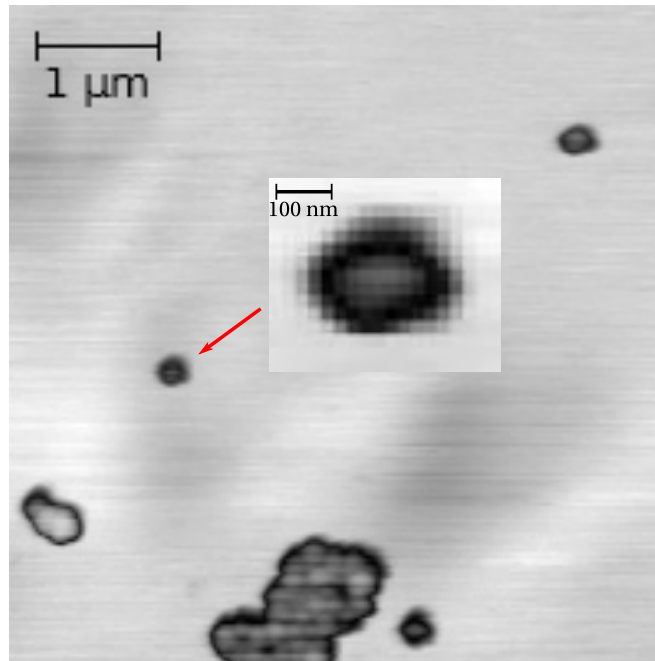


Figure 5.9: SNOM picture of TDBC coated gold nanoparticles deposited on a silicon substrate. The marked particle is that, of which a single particle spectrum was taken. The inset depicts a zoomed picture of that particle. It shows that the particle indeed is not part of a cluster.

Obviously on the picture also clusters can be seen. Thin and weak black lines however enable a distinction between the single particles. Thus it can be seen that the chosen particle (the marked one in figure 5.9) really is lying alone. To ensure this, a further zoom on the particle is depicted in the picture's inset. A distance of over 1 μm to the next neighbour ensures that no other particles lie in the laser spot when the particle is in focus.

The tip and the laser were now focused directly on the chosen particle and a fluorescence spectrum was taken. As already mentioned in the theoretical part in section 2.5, the photon rate can be too small for the lock-in amplifier to discriminate a modulated signal. In this case at least the number of photons per tip modulation, i.e. the number of photons that were detected during one oscillation cycle of the tip, was too small. Therefore, the lock-in could not be connected to the tip oscillation. To filter out noise like dark noise, the excitation laser was chopped. Thus the signal was still modulated, however with a much lower frequency (approx. 200 Hz). For this frequency enough photons reached the detector to detect a modulated signal. This signal was discriminated and amplified by the lock-in with an integration time of 10 seconds. The tip, however, was still necessary causing field enhancement and by that fluorescence enhancement in the region underneath.

The monochromator has a nominal spectral width of 2 nm. Thus a step length of 2 nm was chosen for the spectra. The (analog) signal from the lock-in was digitalized by an analog-to-digital converter and passed on to the controlling PC. This converter recorded the signal at a sampling rate of 12 bit at 1 kHz. For the spectrum a total integration time of 9 seconds was chosen which corresponds to the technically maximum possible value of the converter.

This means for a single particle, a spectrum was recorded for wavelengths between 500 nm and 650 nm with a step width of 2 nm and an integration time of 9 seconds. Since the signal was still very weak, this procedure was repeated eight times and an average value from those eight measurements was taken for every wavelength. The result is shown in figure 5.10(a).

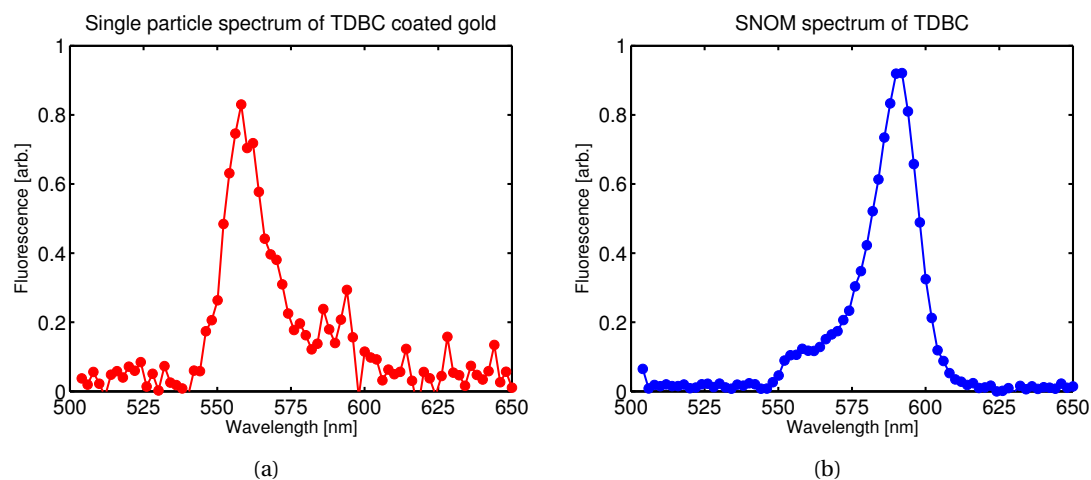


Figure 5.10: Spectrum of a single TDBC coated gold nanoparticle (a) and a spectrum of TDBC directly deposited on a substrate. Here many particles contributed to the spectrum since were adsorbed in a uniform film.

Obviously even after the very long integration time the spectrum is not completely smooth. This is due to the very weak signal. However a clear peak is visible around $\lambda = 558$ nm. This is in the range of the monomer fluorescence of TDBC, although the comparison measurement for different TDBC concentrations in water the monomer peak around $\lambda = 535$ nm. A possible reason for this will be discussed later.

Possibly around $\lambda = 589$ nm a second peak is visible. However it is very weak compared to the ground noise. It is located exactly at the fluorescence of J-aggregates and might be accounted to uncoupled excitons. It might however also be a second vibronic transition of the monomers.

To be able to see the influence of the gold, another sample was prepared with only TDBC taken from the same solution that was used to coat the gold. That means a Si-substrate was coated with polyelectrolytes (PAH as highest layer) and a drop of the solution was given on top. The sample's fluorescence was recorded in the same way as the spectrum above. However since this time a uniform TDBC film was spread over the whole substrate, this is not a single particle spectrum and no special place was chosen for the spectrum.

Due to the high amount of luminous particles in the focus, the fluorescence was very strong. Therefore the integration time of the lock-in as well as its amplification strength was decreased. The result of this measurement is shown in figure 5.10(b).

Since the fluorescence was much stronger, the spectrum is much smoother than that of the gold particle. It shows a peak at $\lambda = 590$ nm which is the same position as that of the J-aggregate fluorescence in solution. Another peak is visible around $\lambda = 554$ nm which coincides with the emission peak of the gold nanoparticles coated with TDBC.

The J-aggregate fluorescence is much stronger than that of the monomers. This was different in the spectra of TDBC dissolved in water. This is due to the fact that the TDBC has dried up on the substrate. Thus the concentration is much higher than in the solutions and most of the monomers could form J-aggregates and only a few molecules have are not clustered to aggregates.

To have a better comparability, the two spectra are shown once more in one plot in figure 5.11.

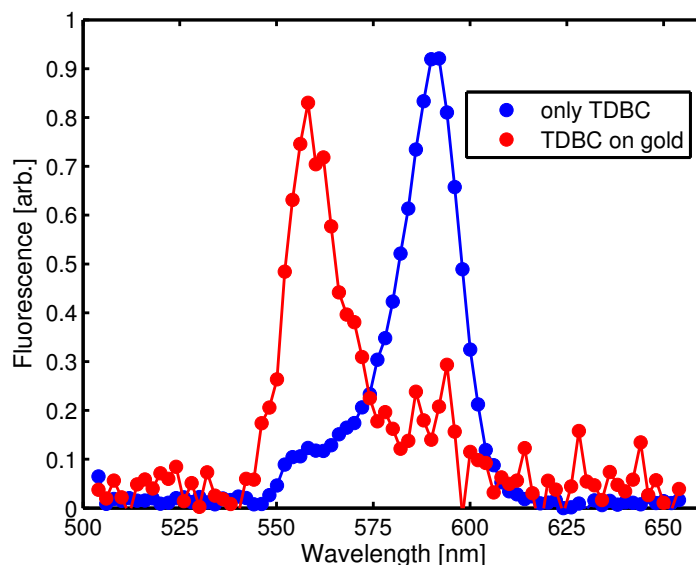


Figure 5.11: Comparison of the two fluorescence spectra of only TDBC and a TDBC coated gold nanoparticle.

Remember that the fluorescence of TDBC without gold was much stronger than that of the gold particle. It had to be scaled down for comparability and the signal was already amplified less when the spectrum was recorded. In reality also the peak around $\lambda = 554$ nm for TDBC without gold particles exceeded that of the gold-TDBC compound by at least a factor of ten since many more molecules were in the focus.

The monomer fluorescence can be seen in both spectra. In comparison with the fluorescence in solution the TDBC for these spectra was tightly packed instead of being able to float freely being less in contact with other TDBC particles. Thus the particles investigated in dry phase had a different chemical environment (also due to the substrate). This seems to have red-shifted the monomer peak. This effect is comparable to the absorption peak shift of plasmons in gold nanoparticles for different surrounding media discussed in section 4.2.

The comparison of the two spectra in figure 5.11 indicates that indeed around $\lambda = 589$ nm there might be a small peak, too. It coincides at least with the J-aggregate peak in the spectrum of TDBC without gold.

Now the question is, in which way the gold nanoparticles influenced the fluorescence of the TDBC. Obviously the J-aggregates do not fluoresce anymore or at least fluoresce very weakly. An easy explanation for this would be the hypothesis that the gold disturbed the formation

of J-aggregates. However this is not the case since the absorption spectrum in figure 5.8 showed that strong coupling between J-aggregates and the particle occurred. Therefore the TDBC obviously did form J-aggregates.

This means that plasmon-excitons evolved, but did not decay by fluorescence. Thus they must have decayed via other channels. One possibility would be that they decayed to excitons in the J-aggregates again. However there was only very little or even no fluorescence of excitons visible. This fluorescence might either have been quenched, which is an effect that can happen for fluorescent particles in vicinity of gold nanoparticles [62].

However this quenching requires a coupling between the excitations called Förster transfer [53]. This would indicate a weak coupling [54] and therefore cannot be the strong coupling that occurred here. Thus it is unlikely that the fluorescence was quenched. This means that the plexcitons apparently did not decay back to excitons.

Other possible decay channels for the plasmon-excitons are a decay into a plasmon or direct energy transfer to the valence band electrons of gold, that means a direct decay to interband transitions in the gold. The plexcitons might also be scattered at discontinuities of the surface of the gold particles.

The last three decay channels are hard to distinguish, but may be a transient absorption measurement might yield information about via which channel the decay mainly takes place. If the particle is excited with a short laser pulse in the absorption region of the TDBC (like in this case $\lambda = 488$ nm) the absorption spectrum changes over time (on a femto- and picosecond scale). Changes in different spectral regions give rise to changes in different physical parameters. By that it might be possible to see, where the energy of a decaying plexciton is transferred.

For couplings between surface plasmon polaritons (SPPs) and excitons, investigations of the decay characteristics of plexcitons have been carried out in the past years. For example, Koponen et al. showed that plexcitons between SPPs on a thin silver layer and excitons in Nile Red only decay via the exciton or the plasmon (and not for example via interband transitions or scattering at surface defects) [63]. For the case presented here, this would mean that the plexcitons decay only via plasmons. However localised plasmons on nanoparticles possess different properties than SPPs and thus conclusions that count for SPPs are not necessarily transferable to localised plasmons. To my knowledge the decay properties of plexcitons of localised plasmons and excitons have not been investigated yet, leaving room for further experiments like the mentioned transient absorption measurement.

Another question is the origin of the small peak in the region of J-aggregate fluorescence in the single particle spectrum at $\lambda = 598$ nm. It can either be caused by TDBC J-aggregates that are not coupled to the gold plasmons at all or it can be caused by excitons that were excited by plexciton decay.

Conclusively it can be said that obviously the gold nanoparticles do have an influence on the fluorescence of TDBC. The original peak of the J-aggregates vanishes almost completely and only monomer fluorescence can be observed. The reason for the extinction of the J-aggregate peak can be explained by the strong coupling between excitons and plasmons. The resulting plexcitons obviously do not fluoresce themselves but decay non-radiatively.

5.4 Comparison between single and many particle spectroscopy

To see how single particle spectroscopy is different to many particle a multi particle spectrum of the TDBC coated gold nanoparticles was recorded. The result is plotted in figure 5.12 together with the single particle fluorescence spectrum.

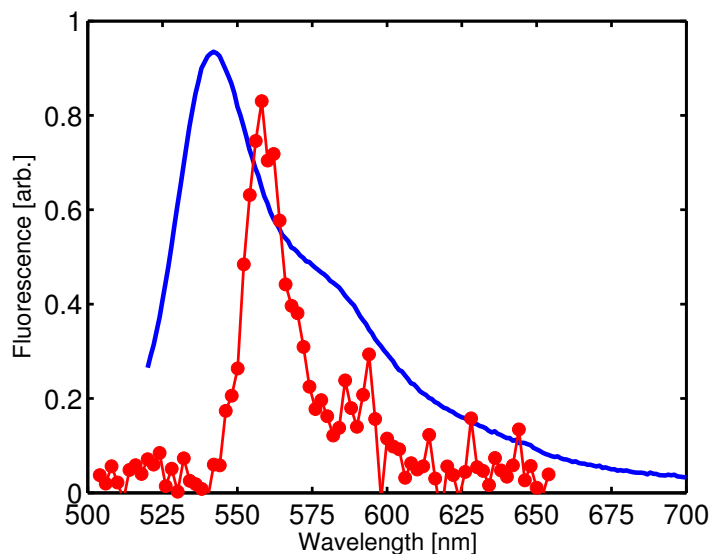


Figure 5.12: Comparison between a single (red) and a multi particle spectrum (blue). The single particle peak is sharper and the second peak around 590 nm is not only a shoulder of the dominant peak. It is however harder to distinguish from noise.

Obviously the peak of the single particle spectrum is much sharper than that of the many particle spectrum. Its full width half maximum can be estimated to be 17 nm. The wider peak in the many particle spectrum is caused by inhomogeneous broadening. In the single particle spectrum only a few fluorescent dyes contributed to the spectrum that were all in more less the same chemical environment. They also coupled to only one single gold particle and thus no inhomogeneities in the plasmon absorption could arise.

The multiple particle spectrum recorded the fluorescence of numerous fluorescent dyes coupled to numerous gold nanoparticles. Thus for both the excitons and the plasmons inhomogeneities arise that cause a broadening of the spectrum. The full width half maximum of this peak can be estimated to be 46 nm, this means 2.7 times wider than that of the single particle spectrum.

In the multi particle spectrum a shoulder of the big peak can be seen around 583 nm. It is probably caused by J-aggregate fluorescence and supports the hypothesis that there is also a peak in the single particle spectrum at approximately the same spectral position. There the peak is not only visible as a shoulder of the big peak but stands alone and is by that easier to interpret (assuming a higher integration time or less noise in the measurement). This is a result of the sharper peaks in the single particle spectrum. These sharper peaks are a feature that shows the advantages of single particle spectroscopy in comparison to multi particle investigations.

A last feature of the two spectra is that the monomer peaks are shifted by 15 nm. The reason for this is most likely of statistical nature. The single particle peak still lies within the peak width of the multi particle peak. Thus it seems like the fluorescence of the few dye monomers that contributed to the single particle spectrum deviates for statistical reasons. For the J-aggregates the shift between single particle and many particle spectrum is not that strong.

Summary: This chapter showed that the SNOM cannot only record high-resolution pictures of sub 100 nm structures. The device can also be used to do single particle spectroscopy. Gold nanoparticles and J-aggregates in TDBC were characterised with absorption or transmission and fluorescence spectra, respectively. Strong coupling between plasmons and excitons was observed. This strong coupling caused a drop in fluorescence of the J-aggregates since the new states, plasmon-excitons do not fluoresce. The advantage of single particle spectroscopy due to the lack of inhomogeneities was presented.

6 Conclusion and outlook

This work documented the successful construction of the first scattering SNOM in the group for ultrafast dynamics in condensed matter at the university of Potsdam under the direction of Matias Bargheer. The single components, an AFM, a classical optical microscope and a confocal microscope, were presented including their working principles. Their practicability was demonstrated.

The AFM could resolve structures with sizes below 100 nm sharply. The classical microscope, used for optical control over the investigated area, also showed a resolution below 2 μm . The confocal part even showed a resolution of 740 nm.

A scattering SNOM was then obtained by combining the AFM tip, used for near field enhancement, and the confocal microscope, used as spatially confined high intensity light source.

The theory for this scattering SNOM was provided, as well. The Abbe limit was presented as lower bound for classical optical microscopy. Its existence is caused by the loss of k -vectors in the detected light. This was the motivation for also using the near field of light to obtain spatial information about small structures.

The occurrence of such near fields was discussed leading to the utilisation of an AFM tip as both source and scatterer of a near field. The electric field beneath such an AFM tip was discussed, showing that it is strongly enhanced compared to the incident field. This enhanced signal is scattered by the AFM tip and guided to a detector. By that the near field signal of one point with the size of the tip's apex is recorded. Scanning over a defined area leads to a near field picture of that region. The use of a lock-in amplifier and a monochromator as noise filter was discussed and arguments for a resolution limit of an s-SNOM were presented.

The SNOM built with this theory as foundation showed its superiority to classical microscopes in high resolution pictures. It could nicely resolve nanoparticle chains with particle sizes of 80 nm. Also, it detected inhomogeneities in an optically active surface that could not be detected with an AFM.

In addition, the new s-SNOM was demonstrated to enable single particle spectroscopy. Strongly coupled plasmons and excitons were investigated, especially their fluorescence characteristics. For this purpose gold nanoparticles could successfully be coated with the organic dye TDBC leading to the occurrence of plexcitons.

The uncoupled components (gold nanoparticles and TDBC) were investigated beforehand, both theoretically and experimentally. The absorption spectrum of the gold nanoparticles proved the existence of localised plasmons in such particles. The transmission and fluorescence spectra of TDBC showed the formation of J-aggregates.

Thus for nanoparticle-TDBC compounds strong coupling could and did take place. This was shown in their absorption spectrum where two peaks arose, shifted in comparison to the two uncoupled peaks showing the characteristic anticrossing.

The fluorescence of the J-aggregates vanished almost completely for the compounds indicating that the occurring plasmon-excitons do not decay radiatively. Neither do they relax to excitons since also in this case fluorescence would be visible. Other decay channels like decay into plasmons or interband transitions are possible and require further investigation for example with transient absorption measurements.

In future the SNOM can also enable scattering spectra on a nanometre scale. For this the tip and the substrates should have spectrally constant dielectric functions since then the scattering field only depends on the spectral properties of the sample. With this also single particle scattering spectra could be obtained for TDBC coated gold nanoparticles. This would lead to a higher precision than in many particle spectra deeper understanding of the strong coupling and plexcitons since inhomogeneities like badly coated particles could be eliminated.

In future this device will be able to be used for time resolved measurements on a femtosecond time scale, thus combining high resolution in time and space. This could for example be used for further investigation of the possible decay channels of plexcitons.

Also Rabi-oscillations of single particles could be investigated with a SNOM with a temporal resolution of a few femtoseconds. These describe the oscillation in energy distribution between the plasmonic part and the excitonic part of a plexciton. To my knowledge such an experiment has until now only been conducted for couplings between excitons and surface plasmon polaritons [64] and not localised plasmons, yet.

Conclusively one can say that the construction of this s-SNOM has enabled a lot of new possibilities for the group of ultrafast dynamics at the university of Potsdam and that these possibilities will even become more after implementing temporal resolution. Doing so will still be a lot of work and a challenge that will be tackled in near future.

Bibliography

- [1] L. Rayleigh, "On the theory of optical images, with special reference to the microscope," *Philosophical Magazine Series 5*, vol. 42, no. 255, pp. 167–195, 1896.
- [2] E. Abbe, "Beiträge zur Theorie des Mikroskops und der mikroskopischen Wahrnehmung," *Archiv für mikroskopische Anatomie*, vol. 9, no. 1, pp. 413–418, 1873.
- [3] E. Synge, "XXXVIII. A suggested method for extending microscopic resolution into the ultra-microscopic region," *Philosophical Magazine Series 7*, vol. 6, no. 35, pp. 356–362, 1928.
- [4] E. A. Ash and G. Nicholls, "Super-resolution aperture scanning microscope," *Nature*, vol. 237, pp. 510 – 512, 1972.
- [5] G. Binnig, H. Rohrer, C. Gerber, and E. Weibel, "Surface studies by scanning tunneling microscopy," *Phys. Rev. Lett.*, vol. 49, pp. 57–61, Jul 1982.
- [6] G. Binnig, C. Quate, and C. Gerber, "Atomic force microscope," *Phys. Rev. Lett.*, vol. 56, pp. 930–933, Mar 1986.
- [7] D. W. Pohl, W. Denk, and M. Lanz, "Optical stethoscopy: Image recording with resolution $\lambda/20$," *Applied Physics Letters*, vol. 44, no. 7, pp. 651–653, 1984.
- [8] A. Lewis, M. Isaacson, A. Harootunian, and A. Muray, "Development of a 500 Å spatial resolution light microscope: I. light is efficiently transmitted through $\lambda/16$ diameter apertures," *Ultramicroscopy*, vol. 13, no. 3, pp. 227 – 231, 1984.
- [9] J. M. Atkin, S. Berweger, A. C. Jones, and M. B. Raschke, "Nano-optical imaging and spectroscopy of order, phases, and domains in complex solids," *Advances in Physics*, vol. 61, no. 6, pp. 745–842, 2012.
- [10] F. Heilmann and R. Hillenbrand, "Near-field microscopy by elastic light scattering from a tip," *Philosophical Transactions of the Royal Society of London. Series A: Mathematical, Physical and Engineering Sciences*, vol. 362, no. 1817, pp. 787–805, 2004.
- [11] J. Wessel, "Surface-enhanced optical microscopy," *J. Opt. Soc. Am. B*, vol. 2, pp. 1538–1541, Sep 1985.
- [12] U. Fischer and D. Pohl, "Observation of single-particle plasmons by near-field optical microscopy," *Phys. Rev. Lett.*, vol. 62, pp. 458–461, Jan 1989.
- [13] F. Zenhausern, M. P. O'Boyle, and H. K. Wickramasinghe, "Apertureless near-field optical microscope," *Applied Physics Letters*, vol. 65, no. 13, pp. 1623–1625, 1994.

- [14] M. Knoll and E. Ruska, "Das Elektronenmikroskop," *Zeitschrift für Physik*, vol. 78, no. 5-6, pp. 318–339, 1932.
- [15] S. W. Hell and J. Wichmann, "Breaking the diffraction resolution limit by stimulated emission: stimulated-emission-depletion fluorescence microscopy," *Opt. Lett.*, vol. 19, pp. 780–782, Jun 1994.
- [16] T. A. Klar and S. W. Hell, "Subdiffraction resolution in far-field fluorescence microscopy," *Opt. Lett.*, vol. 24, pp. 954–956, Jul 1999.
- [17] A. V. Zayats and I. I. Smolyaninov, "Near-field photonics: surface plasmon polaritons and localized surface plasmons," *Journal of Optics A: Pure and Applied Optics*, vol. 5, no. 4, p. S16, 2003.
- [18] S. Kawata, *Near-Field Optics and Surface Plasmon Polaritons*. Physics and astronomy online library, Springer, 2001.
- [19] A. Furube, Y. Tamaki, and R. Katoh, "Time-resolution estimation of a femtosecond time-resolved SNOM having an apertured cantilever tip," *Journal of the Korean Physical Society*, vol. 47, pp. 76–79, 2005.
- [20] L. Novotny and B. Hecht, *Principles of Nano-Optics*. Cambridge University Press, 2006.
- [21] M. Ware, *The Chrysotype Manual: The Science and Practice of Photographic Printing in Gold*. Ffotofilm Pub., 2006.
- [22] M. Faraday, "The bakerian lecture: Experimental relations of gold (and other metals) to light," *Philosophical Transactions of the Royal Society of London*, vol. 147, pp. 145–181, 1857.
- [23] G. Mie, "Beiträge zur Optik trüber Medien, speziell kolloidaler Metallösungen," *Annalen der Physik*, vol. 330, no. 3, pp. 377–445, 1908.
- [24] J. Bozzola and L. Russell, *Electron Microscopy*. Jones and Bartlett series in biology, Jones and Bartlett, 1999.
- [25] S. Eustis and M. A. El-Sayed, "Why gold nanoparticles are more precious than pretty gold: Noble metal surface plasmon resonance and its enhancement of the radiative and nonradiative properties of nanocrystals of different shapes," *Chem. Soc. Rev.*, vol. 35, pp. 209–217, 2006.
- [26] M. Brongersma, J. Hartman, and H. Atwater, "Electromagnetic energy transfer and switching in nanoparticle chain arrays below the diffraction limit," *Phys. Rev. B*, vol. 62, pp. 16356–16359, Dec 2000.
- [27] S. W. Bishnoi, C. J. Rozell, C. S. Levin, M. K. Gheith, B. R. Johnson, D. H. Johnson, and N. J. Halas, "All-optical nanoscale pH meter," *Nano Letters*, vol. 6, no. 8, pp. 1687–1692, 2006. PMID: 16895357.
- [28] A. O. Govorov and I. Carmeli, "Hybrid structures composed of photosynthetic system and metal nanoparticles: Plasmon enhancement effect," *Nano Letters*, vol. 7, no. 3, pp. 620–625, 2007. PMID: 17309315.

- [29] F. Würthner, T. E. Kaiser, and C. R. Saha-Möller, "J-aggregates: From serendipitous discovery to supramolecular engineering of functional dye materials," *Angewandte Chemie International Edition*, vol. 50, no. 15, pp. 3376–3410, 2011.
- [30] V. V. Egorov and M. V. Alfimov, "Theory of the J-band: from the Frenkel exciton to charge transfer," *Physics-Uspexhi*, vol. 50, no. 10, pp. 985–1029, 2007.
- [31] E. E. Jelley, "Spectral absorption and fluorescence of dyes in the molecular state," *Nature*, vol. 138, no. 3502, pp. 1009–1010, 1936.
- [32] G. Scheibe, "Über die Veränderlichkeit der Absorptionsspektren in Lösungen und die Nebenvalenzen als ihre Ursache," *Angewandte Chemie*, vol. 50, no. 11, pp. 212–219, 1937.
- [33] W. West and B. H. Carroll, "Energy transfer in the photo sensitization of silver halide photographic emulsions: Optical sensitization, supersensitization, and antisensitization," *The Journal of Chemical Physics*, vol. 19, no. 4, pp. 417–427, 1951.
- [34] A. Mathur, Y. Hong, B. K. Kemp, A. A. Barrientos, and J. D. Erusalimsky, "Evaluation of fluorescent dyes for the detection of mitochondrial membrane potential changes in cultured cardiomyocytes," *Cardiovascular Research*, vol. 46, no. 1, pp. 126–138, 2000.
- [35] N. T. Fofang, T.-H. Park, O. Neumann, N. A. Mirin, P. Nordlander, and N. J. Halas, "Plexcitonic nanoparticles: Plasmon-exciton coupling in nanoshell-J-aggregate complexes," *Nano letters*, vol. 8, no. 10, pp. 3481–3487, 2008.
- [36] W. Demtröder, *Experimentalphysik 2. Experimentalphysik / Wolfgang Demtröder*, Springer, 2008.
- [37] S. Bliven, "Airy disk spacing near rayleigh criterion." http://upload.wikimedia.org/wikipedia/commons/a/ae/Airy_disk_spacing_near_Rayleigh_criterion.png 2014-03-05.
- [38] H. A. Bethe, "Theory of diffraction by small holes," *Phys. Rev.*, vol. 66, pp. 163–182, Oct 1944.
- [39] C. J. Bouwkamp, "On the diffraction of electromagnetic waves by small circular disks and holes," *Philips Res. Rep.*, vol. 5, no. 401, 1950.
- [40] H. Heinzelmann and D. Pohl, "Scanning near-field optical microscopy," *Applied Physics A*, vol. 59, no. 2, pp. 89–101, 1994.
- [41] J. D. Jackson, *Classical electrodynamics*. New York, NY: Wiley, 3rd ed. ed., 1999.
- [42] D. Meschede, ed., *Gerthsen Physik*. Berlin [u.a.]: Springer, 22., vollst. Neubearb. Aufl. ed., 2004.
- [43] A. Köhler, "Ein neues Beleuchtungsverfahren für mikrophotographische Zwecke," *Zeitschrift für wissenschaftliche Mikroskopie und für Mikroskopische Technik*, vol. 10, pp. 433–440, 1893.
- [44] J. Lim, M. Jung, C. Joo, and S. Kang, "Development of micro-objective lens array for

- large field-of-view multi-optical probe confocal microscopy,” *Journal of Micromechanics and Microengineering*, vol. 23, no. 6, p. 065028, 2013.
- [45] J. Pawley, *Handbook of Biological Confocal Microscopy*. Springer, 2010.
- [46] C. Sönnichsen, *Plasmons in metal nanostructures*. PhD thesis, Ludwig-Maximilians-Universität München, Juli 2001.
- [47] S. Maier, *Plasmonics: Fundamentals and Applications: Fundamentals and Applications*. Springer, 2007.
- [48] P. B. Johnson and R. W. Christy, “Optical constants of the noble metals,” *Phys. Rev. B*, vol. 6, pp. 4370–4379, Dec 1972.
- [49] P. Winsemius, M. Guerrisi, and R. Rosei, “Splitting of the interband absorption edge in Au: Temperature dependence,” *Phys. Rev. B*, vol. 12, pp. 4570–4572, Nov 1975.
- [50] U. Kreibig and M. Vollmer, *Optical properties of metal clusters*. No. Bd. 25 in Springer series in materials science, Springer, 1995.
- [51] G. Lanzani, *The Photophysics behind Photovoltaics and Photonics*. Wiley, 2012.
- [52] E. Purcell, “Spontaneous emission probabilities at radio frequencies,” in *Confined Electrons and Photons* (E. Burstein and C. Weisbuch, eds.), vol. 340 of *NATO ASI Series*, pp. 839–839, Springer US, 1995.
- [53] T. Förster, “Zwischenmolekulare Energiewanderung und Fluoreszenz,” *Annalen der Physik*, vol. 437, no. 1-2, pp. 55–75, 1948.
- [54] L. Novotny, “Strong coupling, energy splitting, and level crossings: A classical perspective,” *American Journal of Physics*, vol. 78, no. 11, pp. 1199–1202, 2010.
- [55] N. T. Fofang, N. K. Grady, Z. Fan, A. O. Govorov, and N. J. Halas, “Plexciton dynamics: Exciton-plasmon coupling in a J-aggregate-Au nanoshell complex provides a mechanism for nonlinearity,” *Nano Letters*, vol. 11, no. 4, pp. 1556–1560, 2011. PMID: 21417362.
- [56] M. Kiel, *Static and Ultrafast Optical Properties of Nanolayered Composites*. PhD thesis, Universität Potsdam, May 2012.
- [57] I. Tabujew and K. Peneva, *CHAPTER 1 Functionalization of Cationic Polymers for Drug Delivery Applications*. The Royal Society of Chemistry, 2015.
- [58] C. Bower, W. Harrison, A. Zayats, R. Pollard, G. Wurtz, and P. Evans, “Plasmonic elements,” Nov. 19 2009. US Patent App. 12/440,770.
- [59] D. D. Lekeufack, A. Brioude, A. W. Coleman, P. Miele, J. Bellessa, L. De Zeng, and P. Stadelmann, “Core-shell gold j-aggregate nanoparticles for highly efficient strong coupling applications,” *Applied Physics Letters*, vol. 96, no. 25, p. 253107, 2010.
- [60] I. H. Malitson, “Interspecimen comparison of the refractive index of fused silica,” *J. Opt. Soc. Am.*, vol. 55, pp. 1205–1208, Oct 1965.

- [61] M. Kiel, M. Klötzer, S. Mitzscherling, and M. Bargheer, "Measuring the range of plasmonic interaction," *Langmuir*, vol. 28, no. 10, pp. 4800–4804, 2012.
- [62] E. Dulkeith, A. Morteani, T. Niedereichholz, T. Klar, J. Feldmann, S. Levi, F. van Veggel, D. Reinhoudt, M. Möller, and D. Gittins, "Fluorescence quenching of dye molecules near gold nanoparticles: Radiative and nonradiative effects," *Phys. Rev. Lett.*, vol. 89, p. 203002, Oct 2002.
- [63] M. A. Koponen, U. Hohenester, T. K. Hakala, and J. J. Toppari, "Absence of mutual polariton scattering for strongly coupled surface plasmon polaritons and dye molecules with a large stokes shift," *Phys. Rev. B*, vol. 88, p. 085425, Aug 2013.
- [64] P. Vasa, W. Wang, R. Pomraenke, M. Lammers, M. Maiuri, C. Manzoni, G. Cerullo, and C. Lienau, "Real-time observation of ultrafast Rabi oscillations between excitons and plasmons in metal nanostructures with J-aggregates," *Nature Photonics*, vol. 7, pp. 128–132, 2013.

Selbständigkeitserklärung

Hiermit erkläre ich, dass ich die vorliegende Diplomarbeit mit dem Titel *Single particle spectroscopy using a scattering scanning near field optical microscope* selbständig verfasst habe. Es wurden keine anderen als die in der Arbeit angegebenen Quellen und Hilfsmittel verwendet. Diese Arbeit wurde in gleicher oder ähnlicher Form noch keiner anderen Prüfungsbehörde vorgelegt und auch noch nicht veröffentlicht.

Ort, Datum

Unterschrift

Danksagung

An dieser Stelle möchte ich mich bei allen Menschen bedanken, die zur Entstehung dieser Arbeit beigetragen haben. Als erstes geht mein Dank an Wouter Koopman für die viele Zeit und die große Geduld, ohne die diese Arbeit in der Form nicht möglich gewesen wäre. Desweiteren möchte ich mich natürlich bei Matias Bargheer bedanken, einerseits für die Möglichkeit, in seiner Arbeitsgruppe diese Arbeit zu schreiben, andererseits für seine Zeit und seinen Rat.

Ein großer Dank geht an die komplette Gruppe für ultraschnelle Dynamik kondensierter Materie, insbesondere an Steffen Mitzscherling, André Bojar, Daniel Schick, Mathias Sander und Radwan M. Sarhan für helfende Hände, Messungen und Materialien. Auch alle anderen Mitglieder der Gruppe haben einen großen Teil zu dieser Arbeit durch anregende Diskussionen, gute Ratschläge sowie ein fantastisches Arbeitsklima beigetragen.

Auch bei der Gruppe für die Physik weicher Materie unter der Leitung von Prof. Dieter Neher sowie bei der Gruppe für Photonik und der Leitung von Prof. Ralf Menzel an der Universität Potsdam möchte ich mich bedanken für die Bereitstellung von Messgeräten und Lasern.

An Paul, Johannes, Mathis, Jonas und Christa geht großer Dank für das Überprüfen der Arbeit in verschiedenen Stadien.

Selbstverständlich möchte ich mich sehr bei meinen Eltern bedanken, die mir durch ihre Unterstützung dieses Studium erst ermöglicht haben.

Und natürlich danke, Sophie.